Low-Temperature Measurement of the Giant Dipole Resonance Width in Sn

By

Paul R. Heckman

A DISSERTATION

Submitted to
Michigan State University
in partial fulfillment of the requirements
for the degree of

DOCTOR OF PHILOSOPHY

Department of Physics and Astronomy

2003

ABSTRACT

Low-Temperature Measurement of the Giant Dipole Resonance Width in Sn

By

Paul R. Heckman

Theoretical calculations within the adiabatic thermal shape fluctuation model predict differences in the behavior of the Giant Dipole Resonance (GDR) width between nuclei with and without shell effects. At low temperatures, in nuclei with strong shell effects, the width is predicted to be suppressed relative to nuclei where shell effects are weak.

Studies have been performed on the GDR properties of nuclei with strong shell effects (^{208}Pb), and weak shell effects (Sn and Cu). The data for nuclei where shell effects are weak show a deviation from predictions at low temperatures. To investigate this discrepancy, an experiment was performed to measure the GDR width in ^{120}Sn at lower temperatures than have previously been measured.

The width of the GDR built on excited states in ^{120}Sn was studied by means of inelastically scattered ^{17}O particles. This technique allowed for the first measurement of the GDR width at a temperature as low as 1 MeV in Sn. A GDR width of 4 ± 1 MeV consistent with the GDR width of the ground state was extracted. This result does not confirm the adiabatic coupling calculations of the evolution of the width as a function of temperature, and indicates an overestimation of the influence of thermal fluctuations.

To my wife, Karen

ACKNOWLEDGMENTS

The completion of this thesis marks the end of my life as a graduate student. It has been a long, and sometimes frustrating experience. That being said, it has also been a very rewarding experience personally. I am indebted to many for their contributions.

First and foremost I would like to thank my advisor, Dr. Michael Thoennessen. This thesis would not have been possible if not for your guidance and support over the past few years. It has truly been an enjoyable experience working with you.

I am also grateful to all that helped in the running of the experiment. This includes everyone from our group, the S800 group, ORNL, University of Washington, and the NSCL staff. The running of this experiment was a group effort.

The lengthy data analysis relied heavily on the computing power here at the NSCL. The computer department and support staff has done a wonderful job making sure that the necessary resources were always available. For this, I thank you.

Finally, I would like to thank everyone that has made my time as a graduate student more enjoyable. You know who you are! I am not even going to try and list everyone. There are many of you, and undoubtedly I would miss someone.

Contents

List of Figures

List of Tables

Chapter 1

Introduction

Giant resonances are an important topic in nuclear physics. These resonances are called "giant" due to their collective nature. More specifically, all of the nucleons take part in the resonance. Several giant resonances have been identified, resulting in two classifications.

The first classification of giant resonances is electric vibrational modes. Several of these modes have been found. In order of their discovery, they are the giant dipole, quadrupole, monopole, and octupole resonances. These terms arise from the names for electric fields of a given spatial complexity [1]. For example, the motion of protons in the nucleus vibrating in the dipole mode give rise to an oscillating electric field that resembles the field generated by two poles, or point charges.

The second classification of giant resonances is magnetic vibrational modes. The magnetic giant resonances involve the spin orientation of the nucleons. In this type of giant resonance, there is a coordinated precession of the nucleons. As a result, the nucleus can acquire a net spin or net magnetic moment that oscillates at the precession frequency. The names of the giant resonances in this category are the giant Gamow-Teller and giant magnetic-dipole resonances.

In this thesis, the giant dipole resonance (GDR) built on excited states will be

investigated. The study of this resonance can provide nuclear structure information. For example, the strong nuclear forces that hold the nucleus together can be probed. The study of this resonance also provides an experimental check on the validity of various theoretical models. The adiabatic thermal shape fluctuation model will be tested in this thesis.

1.1 Background

1.1.1 GDR Built on Ground States

The first measurements of the GDR built on nuclear ground states were in the mid-1940's [1]. The experiments were performed with the use of photonuclear cross-section measurements [2]. The photo-absorption cross section (σ_{abs}) is given by

$$\sigma_{abs}(E_\gamma) = \frac{4\pi e^2\hbar}{Mc}\frac{NZ}{A}\frac{1}{\Gamma}\frac{E_\gamma^2\Gamma^2}{\left(E_\gamma^2 - E_{GDR}^2\right)^2 + E_\gamma^2\Gamma^2}, \tag{1.1}$$

where E_γ is the γ-ray energy, E_{GDR} is the resonance energy, Γ is the resonance width, M is the mass of a nucleon, N is the number of neutrons, Z is the number of protons, and A is the number of nucleons. This functional form of σ_{abs} provides a good description of the shape of the GDR in medium and heavy nuclei by treating the resonance energy, width, and sum rule strength as energy-independent, empirically adjustable parameters [3]. The sum rule strength is defined with the following expression:

$$\sigma_T = \int_0^\infty \sigma_{abs}(E_\gamma)dE_\gamma = \frac{2\pi^2 e^2\hbar}{Mc}\frac{NZ}{A} = 60\frac{NZ}{A}(MeVmb). \tag{1.2}$$

This expression corresponds to a classical E1 sum rule, and is referred to as the Thomas-Reich-Kuhn (TRK) sum rule [4].

The GDR splits into two components for axially symmetric deformed nuclei, corresponding to oscillations along the short axis (high-energy component) and long axis

(low-energy component). The ratio of the strength for the two components provides a sense of the deformation (i.e. prolate or oblate deformed), and the energy splitting is related to the magnitude of the deformation [3]. For the case of deformed nuclei, σ_{abs} can be generalized to include two Lorentzian components.

1.1.2 Macroscopic Picture

The easiest way to describe the motion of the GDR is macroscopically. The center of mass is fixed, and the protons move collectively as a group, as do the neutrons.

One macroscopic description is named after Steinwedel and Jenson [5]. In this model, the motion is thought of as density vibrations of neutron and proton fluids against each other with the surfaces fixed [6], as depicted in Fig. 1.1. This description leads to a form for the resonance energy in terms of the number of nucleons A given by

$$E_{GDR} \propto A^{-1/3}. \tag{1.3}$$

A second description is named after Goldhaber and Teller [7]. Here, the protons and neutrons behave as two separate rigid but interpenetrating density distributions. These rigid distributions undergo a harmonic displacement with respect to each other [6], as depicted in Fig. 1.2. This mode also leads to an expression for the resonance energy, and has the following form:

$$E_{GDR} \propto A^{-1/6}. \tag{1.4}$$

The GDR can also be described as a superposition of the above two modes [6]. The superposition of these two modes leads to the following equation for the resonance energy:

$$E_{GDR} = (1.13 \times 10^{-4} A^{2/3} + 7.34 \times 10^{-4} A^{1/3})^{-1/2}. \tag{1.5}$$

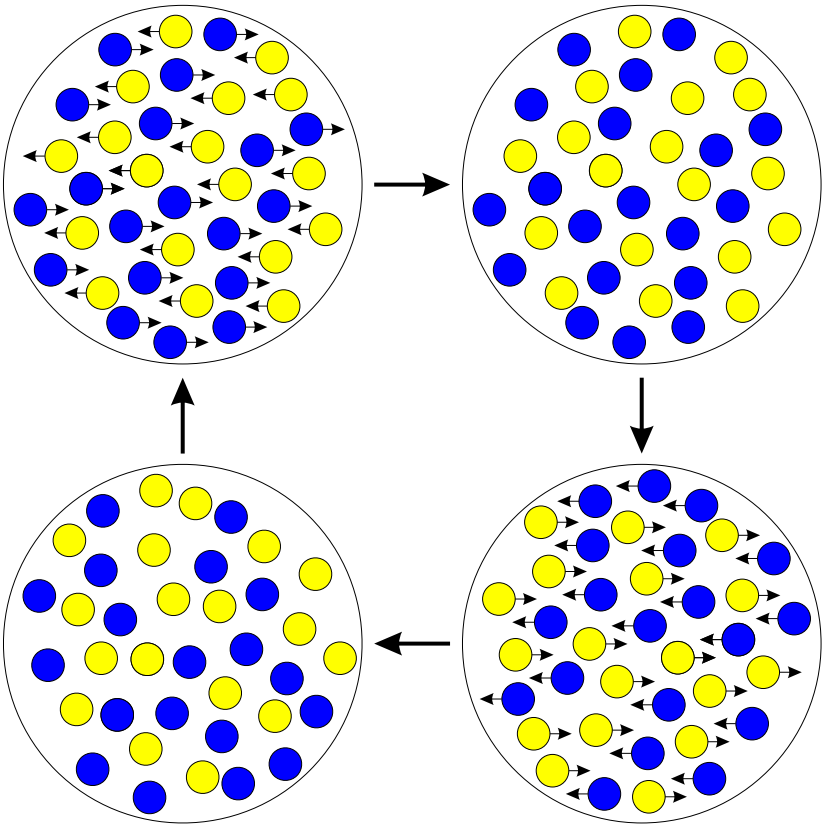

Figure 1.1: Cartoon of Steinwedel and Jenson model to show GDR vibrational motion. The protons are shown in blue, and the neutrons in yellow. *Images in this thesis are presented in color.*

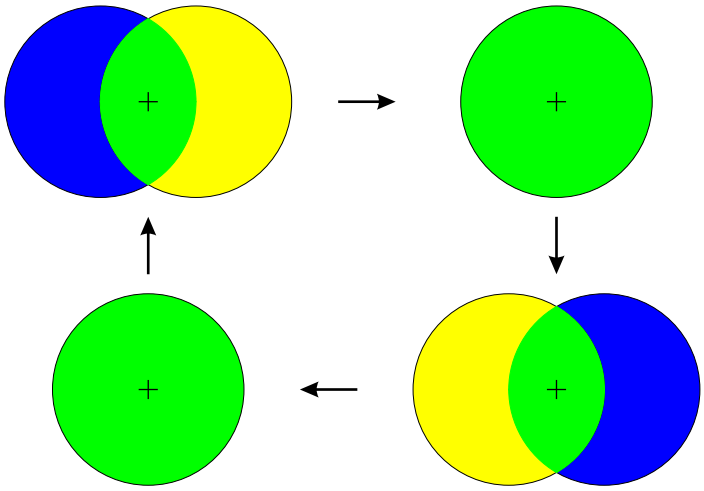

Figure 1.2: Cartoon of Goldhaber and Teller GDR model. The rigid proton distribution is shown in blue, while that of the neutrons is shown in yellow. The interpenetrating area is shown as green. The center of mass is fixed and shown as the cross.

The ratio of the contributions from the GT and SJ modes is

$$\frac{GT}{SJ} = 6.49 \times A^{-1/3}, \tag{1.6}$$

and the contribution from the SJ mode becomes more significant with increasing mass [4].

1.1.3 Microscopic Picture

The microscopic picture of the GDR is more complicated than the macroscopic picture. In the microscopic picture, the collective oscillations of the nuclear system are described in terms of particle-hole excitations, obtained by promoting nucleons from occupied shells to unoccupied shells [8]. In order to describe the resonance in this way, the particle-hole interaction has to be taken into account. This can be done by using the random-phase approximation (RPA) [8]. Examples of this treatment can be found in Refs. [8–10].

Microscopic models have been applied to various nuclei. Despite this, the microscopic picture has limitations. As energy increases, it becomes extremely difficult to perform microscopic calculations. This is due to the fact that all energetically allowed channels must be considered. These channels can include three, four, or more fragments. Presently, a calculation with more than three fragments in the continuum is out of reach at resonance energies [9].

1.1.4 GDR Built on Excited States

The GDR built on excited states differs from the GDR built on nuclear ground states in that it is built on excited states, as the name suggests. The study of the resonance built on excited states provides information about the nucleus at temperatures above 0 MeV. This makes this type of study especially useful in determining properties of

nuclei at high temperatures. For example, it is possible to study the shape evolution of the nucleus with increasing temperature.

The existence of the GDR built on excited states was postulated as early as 1955 by David Brink [4]. He proposed that the energy dependence of the photo-absorption cross section is independent of the detailed structure of the initial state of the nucleus [3]. This weak-coupling hypothesis, known as the Brink hypothesis, implies that Eqn. 1.1 should also apply to the GDR built on excited states.

It was soon realized that the Brink hypothesis together with the existence of a substantial spreading width for the ground-state GDR meant that the high-energy γ decay of highly excited compound nuclei formed in nuclear reactions should be observable and be visible as an enhancement or "bump" at γ-ray energies equal to E_{GDR} [3]. This "bump" was first observed experimentally with proton, ^{3}He, and ^{4}He-induced reactions [11, 12]. In these first experiments, the enhancement was only observed. The first quantitative analysis of a high-energy γ-ray spectrum was on the nucleus ^{252}Cf in 1974 [13].

Since the first measurements of the GDR built on excited states, it has been studied extensively by use of fusion-evaporation reactions [3, 14–22]. More recently, inelastic scattering has been used to study this resonance [23–27]. The most extensive studies have been done on Sn isotopes.

1.1.5 GDR Width

The evolution of the GDR width with increasing temperature has been the focus of many experimental studies [3, 14–27]. These studies have resulted in a significant amount of data covering a relatively large range of temperatures ($0 < T < 3$ MeV). The availability of data over such a broad range of temperatures has lead to theories that predict the width of the GDR as a function of temperature.

In general, the width of the GDR increases with temperature. This increase can

be explained microscopically. The GDR width (Γ_{GDR}) has two components

$$\Gamma_{GDR} = \Gamma\uparrow + \Gamma\downarrow, \tag{1.7}$$

where $\Gamma\uparrow$ is the escape width and $\Gamma\downarrow$ is the spreading width of the nucleus.

The escape width originates from the decay of the collective doorway state to residual nuclei with a one-hole configuration resulting from the emission of a proton or a neutron. In an excited nucleus, the escape width is small, on the order of a few hundred keV [28]. Thus, the increase of the width with temperature is primarily due to the spreading width, which is the result of the coupling of the coherent 1p-1h excitation to 2p-2h and other complicated particle-hole configurations (np-nh) [4].

The magnitude of the spreading width is determined by its coupling with other nuclear degrees of freedom, such as the nuclear shape. Because of this, shape fluctuations are important in the behavior of the GDR. The shape of the nucleus is sensitive to the angular momentum and temperature of the nucleus.

The magnitude of the shape fluctuations is determined in part by the free energy. Several free energy surfaces are shown in Fig. 1.3 for Sn and Pb. The surfaces are much broader in Sn than in Pb at a given temperature, due to the presence of shell effects in Pb. As the temperature increases, the thermal fluctuations increase and the nucleus probes different shapes. The GDR couples to these shape fluctuations and the resonance properties convey information on the time scales of these shape variations [29].

In most nuclei, the width of the GDR is 4–5 MeV at low temperatures (T $\approx$ 0 MeV). The lifetime of the resonance is then on the order of 10^{-22} s. As the nucleus gets hotter, the width of the resonance increases, and the lifetime decreases. The lifetime of the GDR is much shorter than lifetimes of rotational and single-particle states, which have lifetimes on the order of 10^{-14}–10^{-15} s. These estimates indicate the GDR

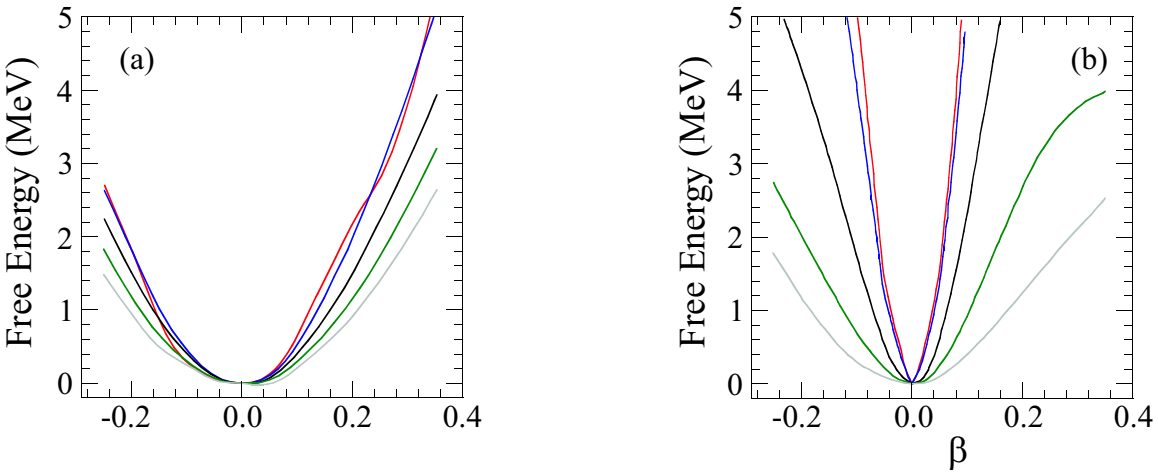

Figure 1.3: Free energy surfaces as a function of the quadrupole deformation parameter β. The deformation parameter γ was set to zero. Panel (a) is for ^{120}Sn and (b) is for ^{208}Pb. See Table 1.1 for the temperatures associated with each distribution.

lifetime is approximately seven to eight orders of magnitude shorter than those of single-particle states and rotational states, respectively.

Several models have been proposed that use shape fluctuations in describing the GDR properties [30]. The model that has been generally adopted is the adiabatic thermal shape fluctuation model. The adiabatic assumption is that the nuclear shape does not change during the time it takes the GDR to damp. The strength is then a weighted sum of the strength distributions that correspond to vibrations built on the possible shapes that the nucleus can have. The increase of the GDR width with increasing temperature is then attributed to the resonance sampling all possible shapes, which become more numerous as the free energy surfaces become more broad and shallow.

In some models that use shape fluctuations, the adiabatic assumption is dropped

Color	^{120}Sn	^{208}Pb
red	0.0	0.0
blue	1.0	0.5
black	2.0	1.0
green	3.0	1.5
gray	4.0	2.0

Table 1.1: Summary of temperatures in MeV associated with each curve in Fig. 1.3.

at high temperatures. These models take the relative time scales for the shape fluctuations into account [30]. In these models, the time spent in each shape configuration decreases with increasing temperature, and enough time may not be spent in a given shape for the GDR to adjust its frequency to the corresponding nuclear shape. As a result, the GDR only feels the average shape of the nucleus. The implication of this is motional narrowing [31].

The GDR width has also been modeled without the use of shape fluctuations. Microscopic calculations based on the linearized Vlasov equation that include the interplay between one-body Landau damping and two-body collisional damping of nucleons have been performed [27, 32].

1.2 Motivation

The evolution of the giant dipole resonance (GDR) has been the focus of many experimental studies. The dependence of the GDR width on temperature and angular momentum has been of particular interest. Fusion-evaporation and inelastic-scattering reactions have been used to extract the GDR width at various temperatures [22,25,27] and angular momenta [20, 21], primarily in Sn and Pb.

Shell effects are thought to play an important role in predicting the width of the GDR [33–35]. The generally accepted model is the adiabatic thermal shape fluctuation model. In this model, the width of the GDR is determined by averaging over a thermal ensemble of nuclear shapes. The increase of the GDR width is then attributed with an increase in shape fluctuations with temperature. In nuclei where shell effects are weak, such as Sn, the shape fluctuations are expected to behave as determined by a rotating liquid drop. This is not the case for nuclei with strong shell effects. In nuclei where shell effects are strong, such as Pb, shell effects must be considered. To take shell effects into account, Nilsson-Strutinksy calculations are used to determine the

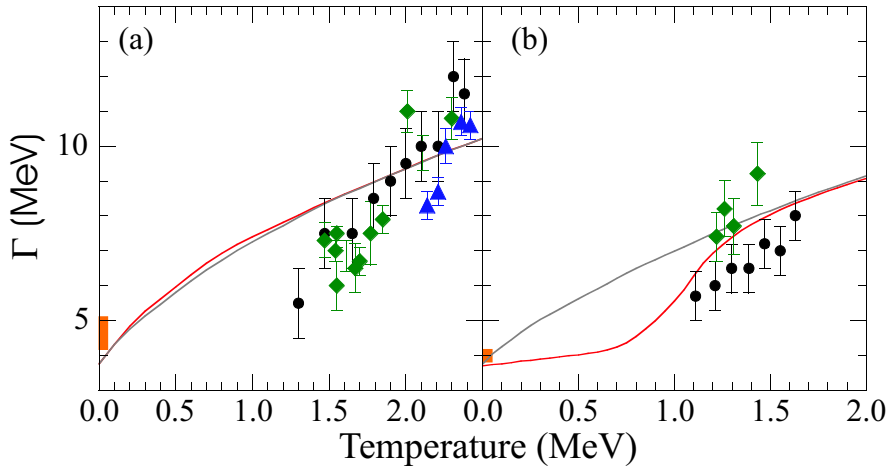

Figure 1.4: Data and theory for Sn and Pb nuclei. Panel (a) – Sn. Panel (b) – Pb. The solid curves are adiabatic thermal shape fluctuation calculations. The shapes were determined using Nilsson-Strutinsky calculations for the red curve, while liquid drop calculations were used for the gray curve. The calculations are taken from Ref. [35]. The black circles and green diamonds are data points taken from Ref. [35]. The black circles were measured using inelastic scattering, whereas the green diamonds are from fusion-evaporation measurements. The blue triangles are taken from Ref. [22]. The orange rectangles show the range of widths measured for the ground state.

shapes.

Both panels in Fig. 1.4 show adiabatic thermal shape fluctuation calculations. Calculations were performed where the shapes were determined within the Nilsson-Strutinsky formalism (red curve) and liquid drop formalism (gray curve). In the Nilsson-Strutinsky formalism, shell effects are considered, whereas in the liquid drop formalism they are not. Examination of Fig. 1.4a shows that the calculations are nearly identical. This suggests that the properties of a rotating liquid drop can be used to determine the shape fluctuations in Sn, as already mentioned. As discussed previously, liquid drop predictions cannot be used for Pb. This is evident in Fig. 1.4b. The initial suppression of the GDR width found in Pb should be absent in Sn.

The existing data for Sn and Pb generally agree with calculations [33–35]. However, the lowest temperature data point in Sn is on the order of 1–2 MeV lower than predicted (see Fig. 1.4a). This discrepancy suggests a possibly significant deviation between theory and experiment. To investigate this discrepancy, the width of the

GDR must be measured at even lower temperatures. Thus, the goal of this thesis was to measure the GDR width at a temperature below 1.3 MeV.

1.3 Experimental Considerations

The majority of experiments performed to measure the GDR width in Sn used fusion-evaporation reactions. These types of reactions cannot be used to study the GDR at low temperatures. Traditional fusion-evaporation experiments are limited to higher temperatures because of the Coulomb barrier in the entrance channel.

Inelastic scattering can be used to study the GDR at low temperatures. Inelastic α-scattering has been used to measure the GDR width as a function of temperature [25, 27] in the past. While this type of reaction is not limited to high temperatures, there is a difficulty associated with it. Inelastic-scattering reactions have the disadvantage that it is difficult to determine the initial excitation energy [36,37]. This is due to knockout reactions and contributions from other reactions that do not lead to full energy equilibrium of the energy loss of the scattered particle. The latter effect becomes more important with increasing projectile energy loss. The contribution due to knockout reactions can be reduced by using heavy-ion scattering as opposed to α-scattering [24].

The reaction employed in this experiment was ^{120}Sn(^{17}O,^{17}O$'$). The projectile ^{17}O was chosen for several reasons. As mentioned above, the contribution from knockout reactions and other processes that do not lead to full energy equilibrium of the energy loss of the scattered projectile should be reduced with heavy-ion scattering. The neutron binding energy of ^{17}O is also very low (4.14 MeV). This is important as we wish to study target excitations and not projectile excitations. If the projectile becomes excited in the scattering process, it will emit γ rays with energies up to the neutron binding energy. Since the neutron binding energy is low, these γ rays will have

energies below the region of interest. The γ-ray energies probed in this experiment range from 8–25 MeV. If the projectile is excited to energies above the neutron binding energy, it will lose the loosely bound neutron to form ^{16}O. These events are easily discriminated against as we demand an ^{17}O fragment to be in coincidence with the detected γ rays.

Chapter 2

Experimental Details

The experiment was performed at the National Superconducting Cyclotron Laboratory (NSCL). A primary beam of ^{17}O was accelerated by the K1200 cyclotron to 80 MeV/nucleon. The beam was sent down the analysis line to the S800 magnetic spectrograph. Here the beam bombarded a 7.45 mg/cm^2 target of ^{120}Sn.

Three major detector systems were used in this experiment. These systems included an array of Barium Fluoride (BaF_2) scintillators, an array of Cesium Iodide (CsI) scintillators, and the S800 spectrometer. The BaF_2 scintillators were used to measure high-energy γ rays. The CsI scintillators detected charged particles. The S800 measured inelastically scattered ^{17}O particles and other reaction products. The S800 focal plane detectors ultimately determined scattered particle energy loss. The focal plane detectors also allowed for accurate particle identification. A schematic of the setup is shown in Fig. 2.1.

The BaF_2 scintillators were arranged into two close-packed arrays. Each array consisted of 68 scintillators. The arrays were placed at angles of $\pm 90^\circ$ with respect to the target chamber of the S800. The geometry of the arrays is shown in Fig. 2.2. The scintillators were stacked in a wall type configuration. The gap in the stacking scheme was necessary because of the design of the S800 target chamber doors.

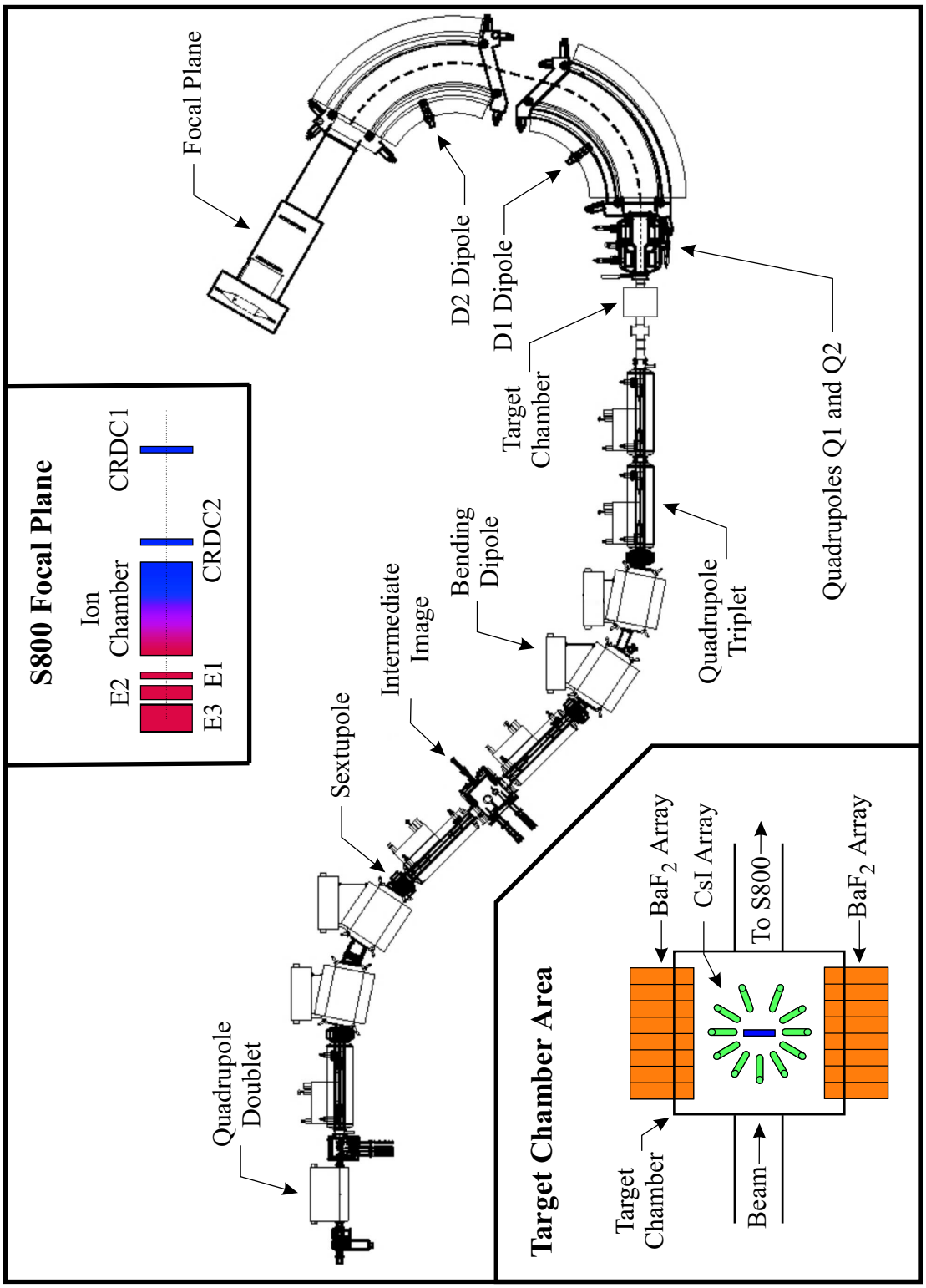

Figure 2.1: Schematic of experimental setup. This drawing is not to scale.

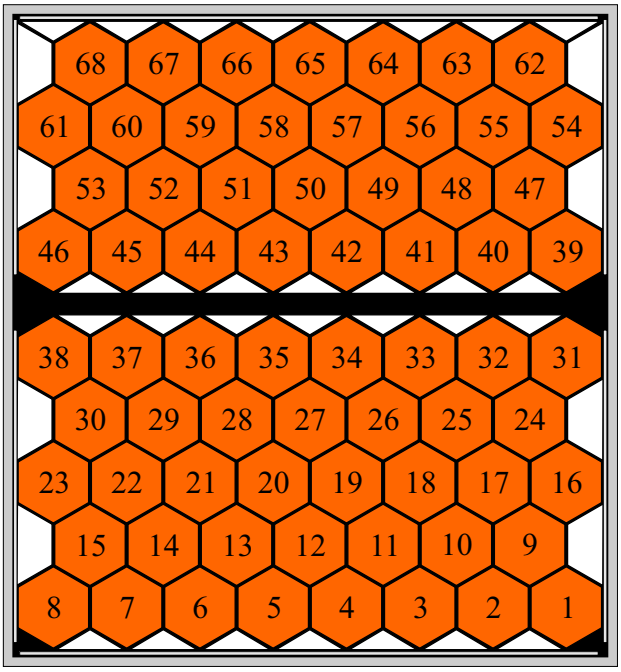

Figure 2.2: Schematic view of one of the BaF_2 arrays. The detectors are shown as the orange hexagons. The white trapezoids were plastic that aided in the stacking of the arrays. The aluminum frame used to hold the array together is also evident.

The S800 target chamber doors were modified in order to get the BaF_2 arrays as close to the target as possible. Each door had a cavity that extended into the target chamber. A piece of aluminum was welded to the back wall of the cavity to provide strength. This piece of aluminum extended into the cavity, and is evident in Fig. 2.3. As a result, it was necessary to stack the BaF_2 scintillators with a gap between two of the rows. Positioning the arrays closer to the target gives a larger solid angle coverage, which results in a higher detection efficiency.

The CsI scintillators were mounted inside the S800 target chamber. There were 11 of these scintillators in all. Nine of these scintillators were attached to the roof of the target chamber, while the two most forward detectors were attached to the forward wall. A picture of the CsI array is shown in Fig. 2.4. The most forward detector in the picture was removed for the run. The array covered scattering angles as indicated in Table 2.1.

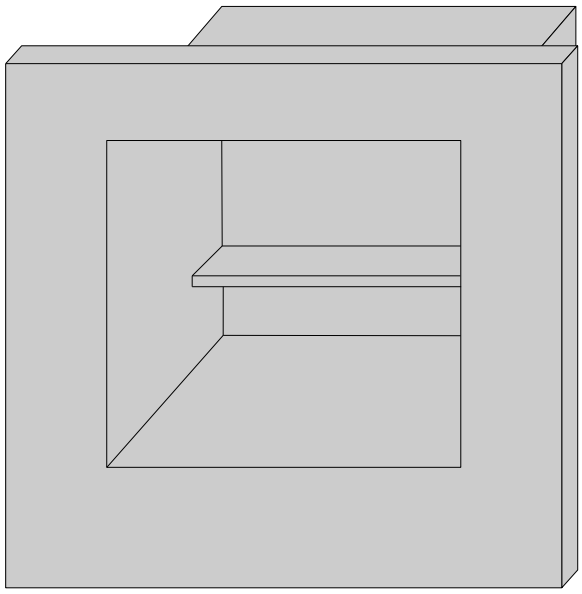

Figure 2.3: Perspective drawing of the S800 target chamber door. Notice the aluminum extrusion from the door cavity.

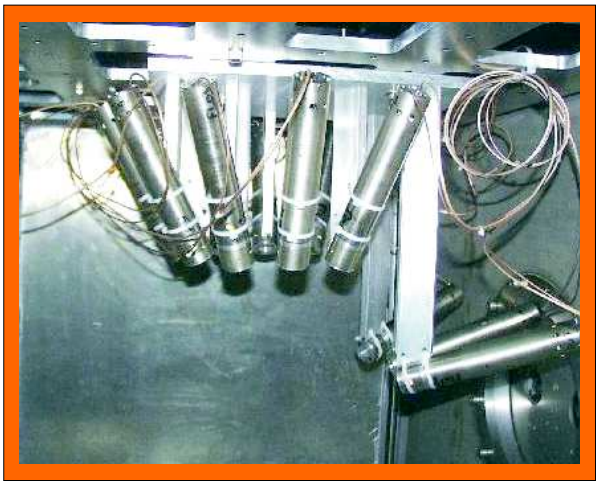

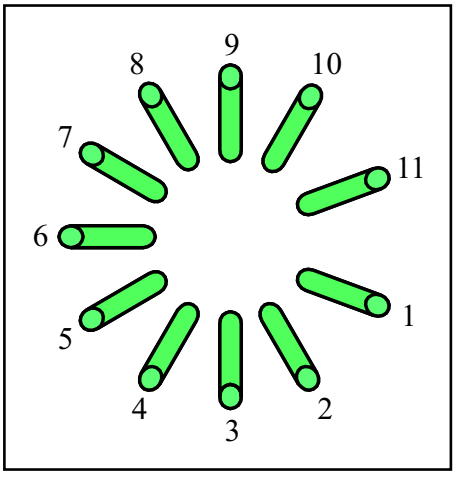

Figure 2.4: The direction of the beam is from left to right in both panels. Left: Photo of the CsI array. The most forward detector was removed during the experiment. Right: Top view of the CsI array. The CsI detectors are depicted as green cylinders.

Number	θ (degrees)	ϕ (degrees)
1	30	20
2	60	60
3	90	60
4	120	60
5	150	60
6	180	60
7	-150	60
8	-120	60
9	-90	60
10	-60	60
11	-30	20

Table 2.1: Lab angles of the CsI detectors. θ is the scattering angle, and ϕ is the azimuthal angle. The z-axis is given by the direction of the beam. The numbering scheme is as in Fig. 2.4.

2.1 Detectors and Experimental Devices

2.1.1 BaF_2 Scintillators

BaF_2 is an inorganic scintillator. The scintillation light consists of two components, namely the fast component and the slow component. The fast component has a decay time of 0.6 ns emitted in the short wavelength (220 nm) region of the spectrum, while the slow component has a 630 ns decay time at wavelengths longer (310 nm) than that of the fast component [38]. The very short decay time of the fast component makes BaF_2 an excellent sub-nanosecond timing detector. In addition to the excellent timing capabilities of BaF_2, it also has a high density (4.89 g/cm^2) [39]. The high density makes this material good for γ ray detection.

The two arrays of BaF_2 scintillation detectors were assembled and installed at the NSCL. The BaF_2 detectors belong to Oak Ridge National Laboratory (ORNL), Texas A&M University (TAMU), and Michigan State University (MSU). All scintillators are regular hexagons. The ORNL and TAMU scintillators have a length $l = 19.5$ cm and hexagonal cross section of inscribed radius $r = 3.25$ cm. The MSU dimensions differ in that they have $l = 24.5$ cm and $r = 3.00$ cm. The various BaF_2 detectors were

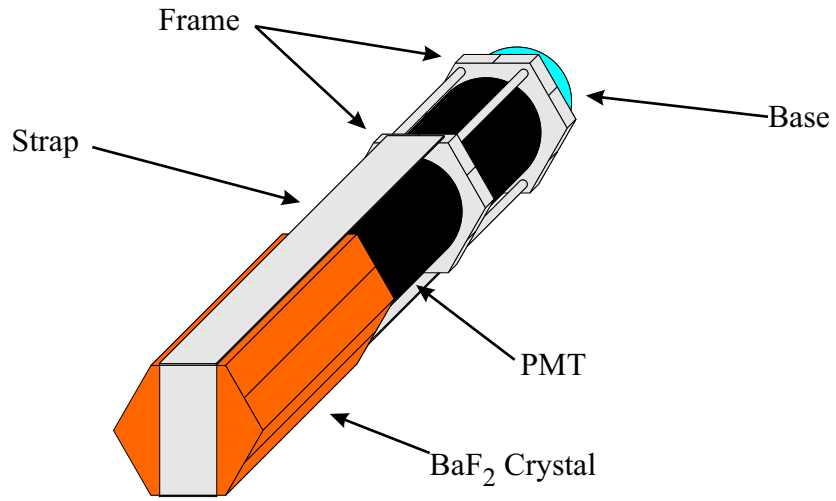

Figure 2.5: Perspective drawing of a BaF_2 scintillator. All components are shown except for the materials used to wrap the crystal.

stacked into the arrays as follows: 1–15 TAMU, 16–61 ORNL, and 62–68 MSU. The numbering scheme follows that of Fig. 2.2. All together 136 BaF_2 detectors were used.

Each BaF_2 detector consisted of a BaF_2 crystal, photomultiplier tube (PMT), strap, frame, and base. The crystal was attached to the PMT by use of optical grease. This grease is transparent to the ultraviolet light emitted in BaF_2. The crystal was then wrapped in teflon tape. The teflon tape gives the edges of the crystal a highly reflective surface, which results in maximum light collection. Once coated with the teflon tape, the crystal was wrapped with black electrical tape. The black tape produced a covering that was light tight. To aid in the strength of the coupling of the PMT to the crystal, a frame and strap were used. This also helped in the stacking of the arrays. A base was then attached to the PMT for applying voltage. Fig. 2.5 shows exactly how the various components of the BaF_2 detectors were connected.

2.1.2 CsI Array

CsI is an inorganic scintillator. CsI is typically activated with either thallium (Tl) or sodium (Na). The scintillators used in this experiment were activated with Tl. The resulting scintillation light consists of two components, namely the fast and slow

component. The fast component has a decay time of 0.68 μs, and the slow component has a decay time of 3.34 μs. The two components of light emitted allows for pulse shape discrimination to differentiate among different types of radiation. The density is 4.51 mg/cm^2 [39]. The scintillators were cylindrical in shape, with a length of 3 cm and diameter of 1.5 cm.

The CsI scintillators were assembled as follows: first, all but one end of the crystal was wrapped in teflon tape. As in the case of BaF_2, this gave the edges of the crystal a highly reflective surface. This is important for maximum light collection. Next, the wrapped crystal was put into an aluminum can. The aluminum can served to protect the crystal and to seal it from outside light. Finally, a photomultiplier tube was attached to the end of the crystal not wrapped in tape.

2.1.3 S800 Magnetic Spectrograph

The S800 spectrometer is composed of an analysis line and a magnetic spectrograph. The analysis line consists of four bending dipoles, one quadrupole doublet, five quadrupole triplets, and four sextupoles (See Fig. 2.1). The magnetic spectrograph contains two dipole magnets (D1 and D2), two quadrupoles (Q1 and Q2), and a series of detectors in its focal plane [40]. The focal plane detectors consist of two cathode readout drift chambers, an ion chamber, and three plastic scintillators [41].

The magnetic spectrograph bends scattered fragments to its focal plane. The two quadrupoles focus fragments in the dispersive (x) and non-dispersive (y) directions. The two dipole magnets have a bending radius of 2.8 m with a maximum central field of 1.6 T, giving an overall bending power of 4 Tm. This results in an angular acceptance of 7° and 10° in the dispersive and non-dispersive directions, respectively [41]. Running the spectrograph in dispersion-matched, energy-loss mode compensates for intrinsic beam momentum spreading in the dispersive direction, which ideally gives a zero-width image at the focal plane [40]. The S800 is capable of correcting Δp/p

by 1% for every 10 cm at the dispersive image. The overall energy acceptance of the device is 10%. For a very detailed description of the S800 and its operation see Ref. [42].

Cathode Readout Drift Chambers

The Cathode Readout Drift Chambers (CRDC1 and CRDC2) are position sensitive detectors in the S800 focal plane. The active area of each detector is 30 cm $\times$ 59 cm with an active depth of 1.5 cm. The volume of the detectors is filled with a mixture of 80% CF_4 and 20% C_4H_{10} gas at a pressure of 140 Torr [41].

The gas in the detector volume is ionized by charged particles passing through it. The electrons created in this process drift through a region with a constant electric field until they reach a grounded Frisch grid. Once the grid is passed, charge amplification (electron avalanche) takes place and the electrons are accelerated towards the anode wire. The anode wire is typically kept at 1400 Volts. Cathode pads are located in front of and behind the anode wire. There are 224 cathode pads in all. The Frisch grid insures that the integration over all pad signals will be independent of the charged fragment's interaction distance from the anode. This is due to the fact that no charge amplification takes place in the region of constant electric field [40].

The dispersive (x) position is determined with a Gaussian fit over non-zero pad signals. The centroid of the fit gives the position. The non-dispersive (y) position is determined by measuring the drift time of the electrons from the point of interaction to the anode. The position resolution of these detectors is designed to be better than 0.48 mm in both directions.

Ionization Chamber

The ionization chamber (IC) is a detector that gives energy loss information. This detector is a standard Frisch gridded ion chamber that is segmented into 16 one-inch

anodes perpendicular to the path of the ions [41]. The IC volume is filled with P10 gas at a pressure of 300 Torr. This gas is 90% argon and 10% methane. Sampling the energy loss along the path through the IC reduces the noise, and provides an accurate energy-loss signal.

Scintillation Detectors

The last set of detectors in the S800 focal plane are a series of scintillators. The scintillators provide fragment energy loss and total energy information. They can also be used for timing purposes. There are three scintillators in all. The first one (E1) is 5 cm thick, while the second (E2) and third (E3) are 10 and 20 cm thick, respectively. All three scintillators are made of plastic. Light guides are attached to both ends of the plastic, and PMTs are attached to the light guides. The light guides direct the light created in the scintillation process from the plastic to the PMTs. This results in higher light collection. The E1 scintillator was also used to determine the time-of-flight of fragments relative to the cyclotron radio frequency (RF).

2.2 Electronics

This experiment utilized three different electronic systems. These systems correspond to the BaF_2 array, CsI array, and S800 spectrometer. Two different threshold settings were used in the BaF_2 electronics. During the run, the BaF_2 acquisition was started if any of the individual detector elements had energy deposition greater than a high threshold, T_h. In the event that T_h was exceeded by any of the detector signals, a high gamma trigger was created. Also, energy and time information was collected for all detector elements with energy deposition greater than the low threshold, T_l. The CsI acquisition was started based on the energy deposited in the individual detector elements. If any of the individual detectors had energy deposited greater than the

threshold, a CsI master trigger was generated. Additionally, energy and time-of-flight information was collected for all CsI detectors. The S800 acquisition was started if both PMTs attached to the E1 scintillator had a signal. If a signal was present in both PMTs, a S800 master trigger was generated and information was collected from all S800 focal plane detector elements.

2.2.1 BaF_2 Electronics

Each of the 136 BaF_2 scintillation detectors had two output signals. One of these signals was delayed and split into two parts, namely the fast and slow signals. The fast and slow signals were sent to a charge-to-digital converter (QDC) unit. The QDC units integrated the charge and digitized it to give energy information. The other output from each detector was used for logic and timing. This signal was attenuated and fanned into two parts. The signals were attenuated to approximately match the thresholds from detector to detector. The fanned logic signals were sent to leading edge discriminators, one with threshold T_l and the other with threshold T_h. The signals sent to the discriminator with threshold T_l were used to generate the low gamma (lo-γ) logic, while the others were used to generate the high gamma (hi-γ) logic. The lo-γ and hi-γ logic was used to generate gates for the various electronic modules, triggers for the data acquisition, and for timing purposes.

The lo-γ logic path began with the 136 individual detector signals. These signals were sent to 10 different 16 channel discriminators, all with threshold T_l. This formed 10 banks, each with up to 16 detectors. The individual outputs from each channel were sent to a time-to-digital converter (TDC) unit. These signals were delayed and served as individual stops to the TDC for each detector element. The TDC unit was run in common start mode. The common start was provided by the event output from the trigger box (to be discussed in Sec. 2.2.4). In addition to the individual outputs, each of the 10 discriminators also had a single output that worked as a logical OR.

The logical OR signal from each of the 10 discriminators were input to another logic unit. This logic unit served as a logical OR to the 10 OR-ed discriminator signals. This resulted in a single output that was true if any of the 136 detectors fire. It was this signal, in coincidence with the master event signal, that was ultimately used to generate the QDC gates. This signal was also used as the lo-γ trigger.

The hi-γ logic path began in the same way as the lo-γ logic. The 136 detector signals were sent to 10 discriminators, each with threshold T_h. As in the case of the lo-γ logic, each of the 10 discriminators had a logical OR output. The 10 OR-ed outputs were sent to a logic unit. This unit served as another logical OR. The resulting output was used to generate the hi-γ trigger.

A diagram of the electronics is shown in Fig. 2.6. The lo-γ and hi-γ triggers were input to the trigger box used in this experiment. The clears for the TDC and QDC units came from the computer.

2.2.2 CsI Electronics

The CsI electronics were responsible for reading out energy and time information from the individual CsI detectors. The readout was triggered based on the energy deposited in the individual CsI detectors. If any of the detectors had energy deposition greater than the threshold setting, energy and time information was gathered for all 11 elements. The time was determined with a TDC, where the individual detectors provided a stop and the master event signal provided a common start. Both the fast and slow energies were read out with the use of a QDC. A diagram of the electronics is shown in Fig. 2.7. Clears for the QDC and TDC modules came from the computer.

2.2.3 S800 Electronics

The S800 electronics were responsible for reading out signals from all focal plane detector elements. The readout was triggered based on the E1 scintillator. If both

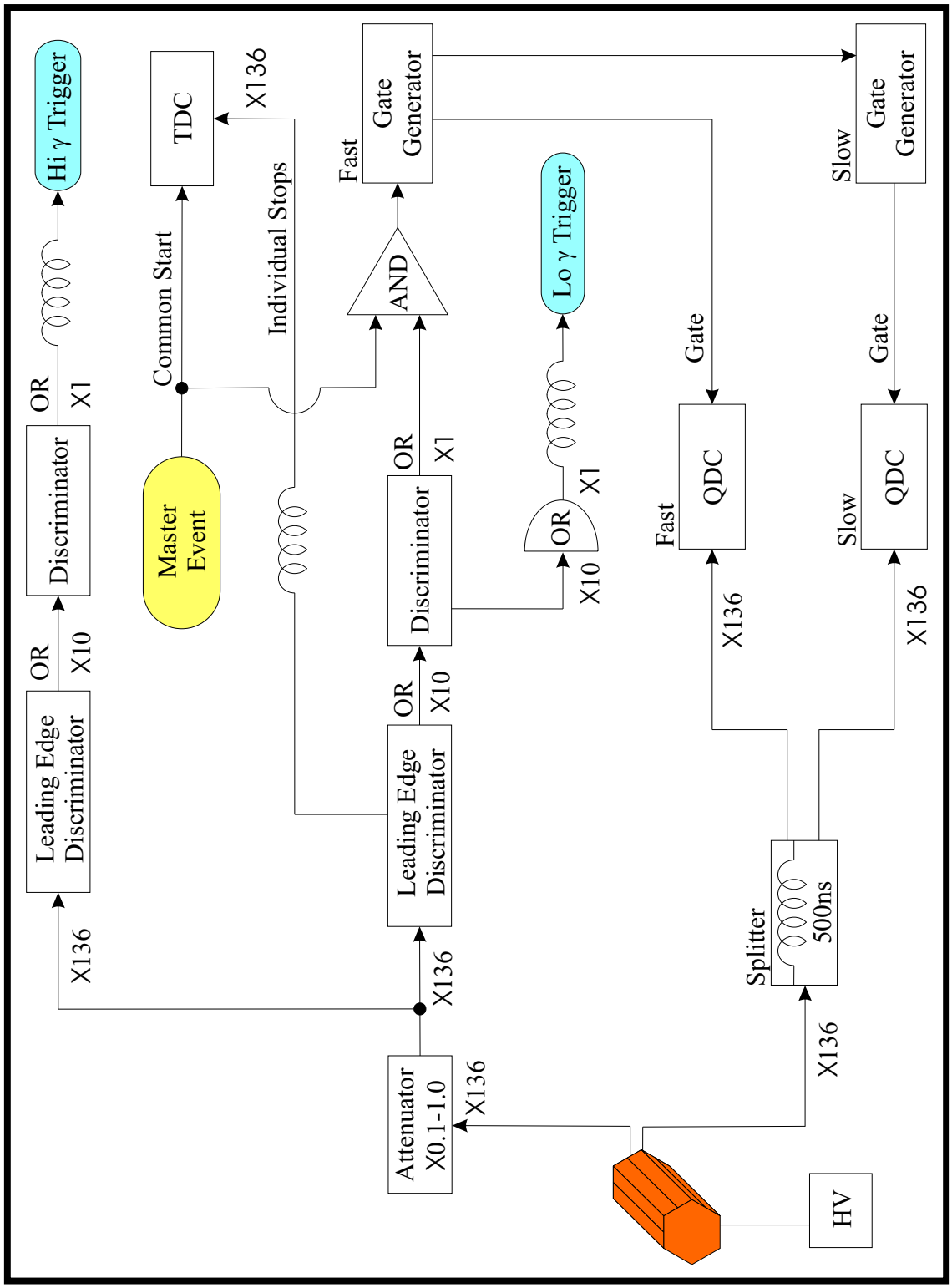

Figure 2.6: Diagram of the BaF_2 electronics.

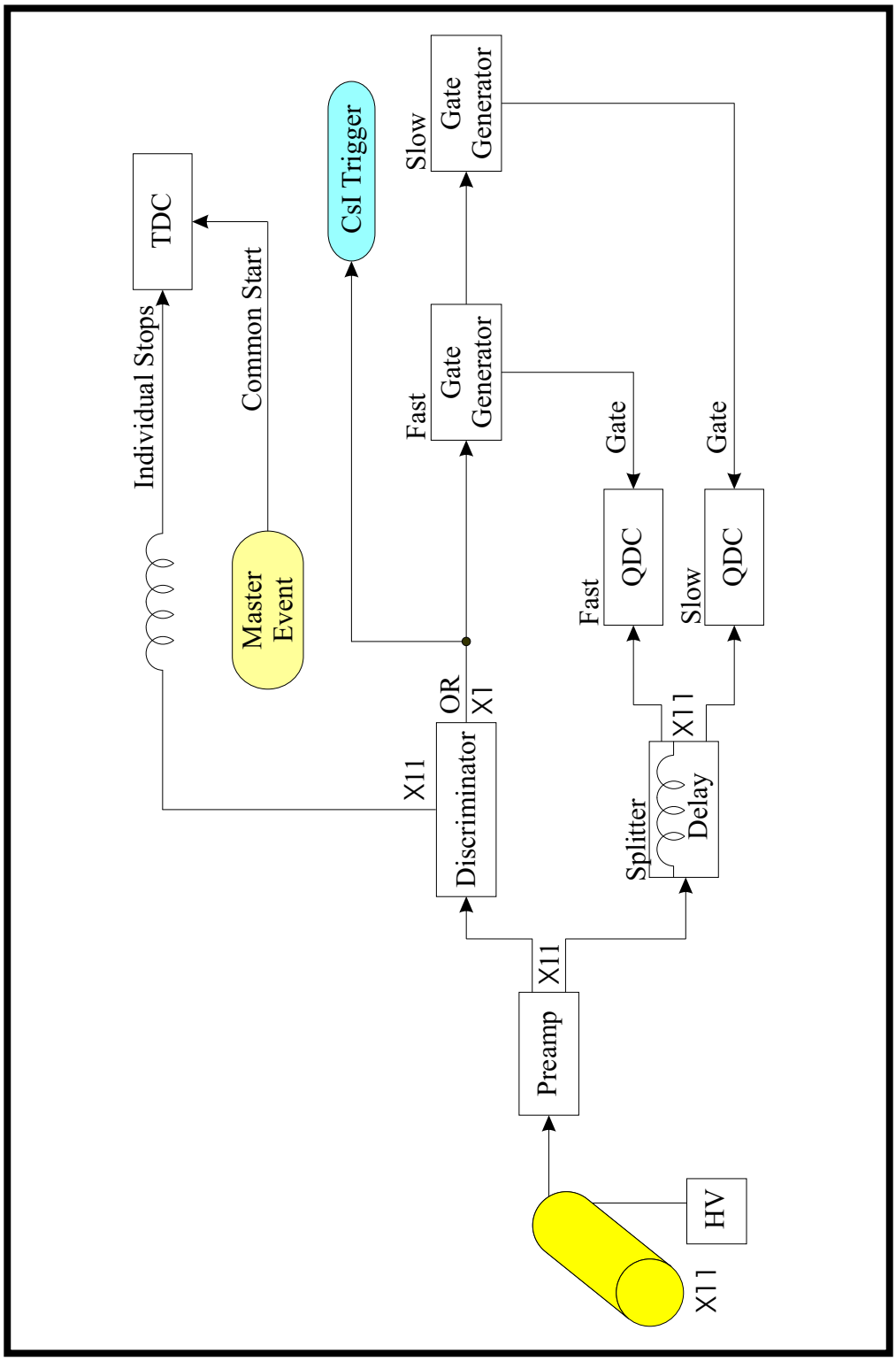

Figure 2.7: Diagram of the CsI electronics.

PMTs on this scintillator had a signal, the trigger was generated. Specifically, the gates for the S800 electronics were created by the logical AND of constant fraction discriminator (CFD) signals from both E1 scintillator PMTs. This signal also served as the start signal for each CRDC time-to-analog converter (TAC). The stops for each of these TACs came from the individual CRDC anodes. Additionally, the logical AND between both E1 PMTs was the stop for a TAC which measured time-of-flight relative to the cyclotron RF. The cyclotron RF provided the start for this TAC. The analog signals from each TAC were sent to an analog-to-digital converter (ADC) to be read by the acquisition. Diagrams of the electronics can be found in Ref. [42].

2.2.4 Trigger Box Electronics

The trigger box (TB8000) served as the control system between the various detector systems and data acquisition. A diagram of TB8000 is shown in Fig. 2.8. TB8000 allowed for easy selection of which events started the acquisition, as the different triggers were selected with the flip of a switch. It also allowed for downscaling of the different inputs. Additionally, if the computer was busy, TB8000 was inhibited. This was to block events that occur while the computer was still processing the current event. Both raw and downscaled signals were sent to scaler modules.

The trigger inputs to TB8000 were Lo-γ, Hi-γ, S800 master, CsI master, a coincidence trigger formed between a logical AND between Hi-γ and S800 master, and a second coincidence trigger formed between a logical AND between CsI master and S800 master. Several triggers were selected during the experiment. Both coincidence triggers were used to trigger the acquisition. The S800 master also triggered the acquisition during the run. The S800 master was downscaled by a factor of 128 to give S800 singles events. The Lo-γ trigger was used for source calibration purposes with the BaF_2 array. Similarly, the CsI master trigger was used for calibration purposes with the CsI array.

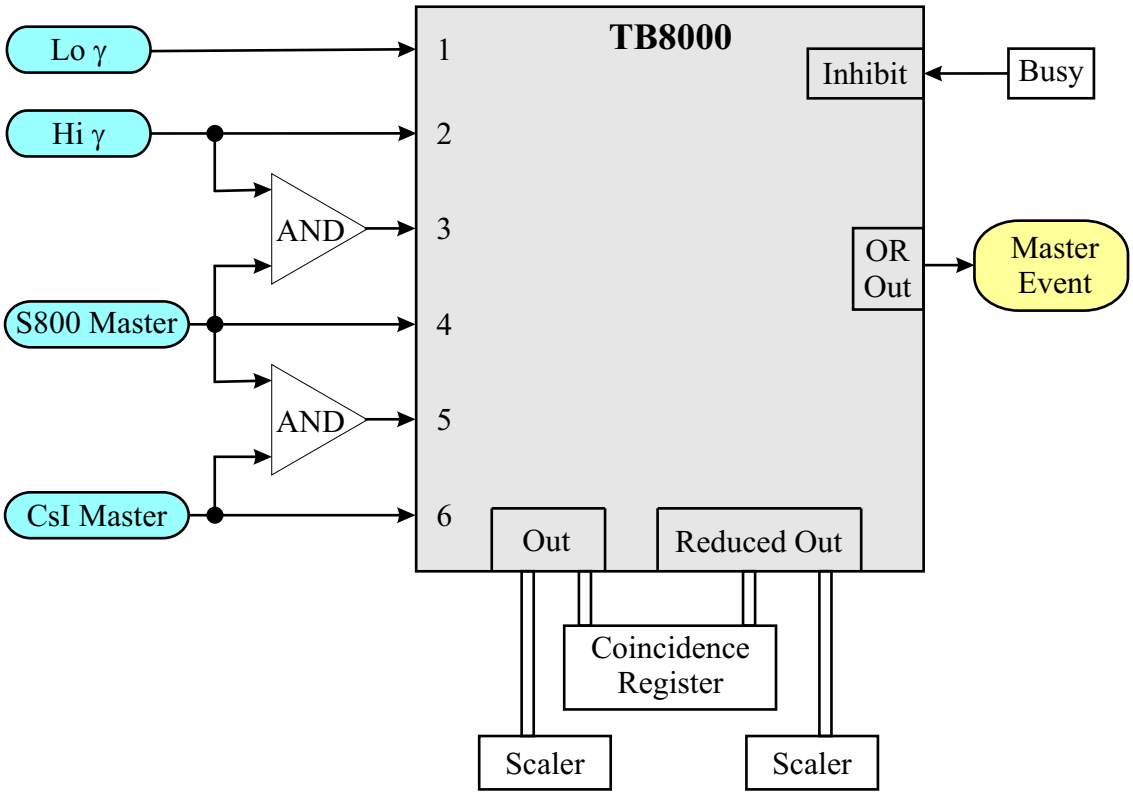

Figure 2.8: Diagram of trigger box, TB8000, which controlled the data acquisition for this experiment. All inputs and outputs are described in the text.

Chapter 3

Data Analysis

The experimental data analysis consisted of several parts. First calibrations were performed. All detectors in the BaF_2 array and CsI array were calibrated for time and energy. The only elements that needed calibration in the S800 focal plane were the CRDC detectors. These detectors were calibrated for position. After the calibration process, it was necessary to identify the fragments detected in the S800 focal plane. This was to ensure that only inelastically-scattered ^{17}O events were considered. Next, the γ-ray events detected with the BaF_2 array were isolated. The γ rays were then correlated with projectile energy loss in order to extract γ-ray spectra corresponding to various projectile energy losses. Finally, proton events in the CsI array were isolated from other events. These events were also correlated with projectile energy loss.

3.1 Calibrations

3.1.1 BaF_2 Array

Each of the 136 BaF_2 detectors was calibrated for energy. The energy calibration was carried out by using a source of ^{88}Y and PuBe. These two sources gave calibration points at 0.898 MeV, 1.836 MeV, 3.927 MeV, and 4.438 MeV. The two lowest energy

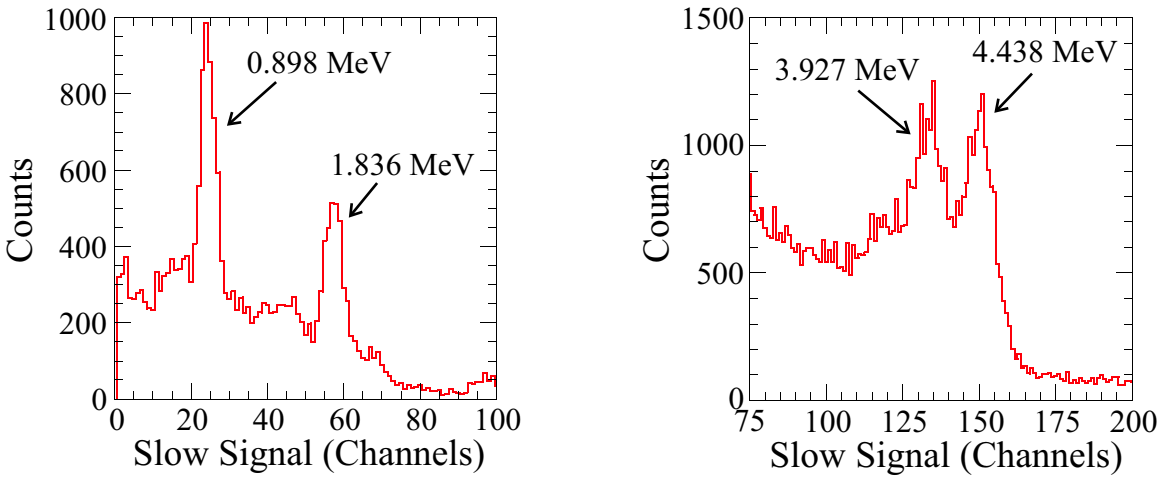

Figure 3.1: Left: ^{88}Y source calibration spectrum. Right: PuBe source calibration spectrum. The lower energy peak in this plot is the first escape peak.

points were from the ^{88}Y source, while the other two were from the PuBe source. Fig. 3.1 shows a typical spectrum resulting from the two sources. The first escape peak is evident in the PuBe spectrum, and gave the calibration point at 3.927 MeV. A higher energy calibration point was obtained from cosmic rays. The energy deposited in the individual detector elements from cosmic rays depends on the geometry of the detectors. Hence, the energy deposited in the ORNL and TAMU detectors was the same. The detectors belonging to MSU had a lower amount of energy deposition as compared to the other two types. The energy deposited in the ORNL and TAMU detectors corresponds to an energy of 40.290 MeV, while in the MSU detector it is 37.930 MeV. These energies are based on simulations run at ORNL. In this analysis, only the slow component was calibrated. A typical energy calibration curve is shown in Fig. 3.2. A calibrated cosmic-ray spectrum is shown for both an MSU and ORNL/TAMU detector in Fig. 3.3.

The time calibration of the BaF_2 detectors consisted of two parts. First, all of the timing channels were gain matched. This was accomplished by using a pulser to trigger the electronics. With the electronics triggered in this manner, a spectrum was measured with several peaks (Fig. 3.4). The time between peaks corresponds to 40 ns,

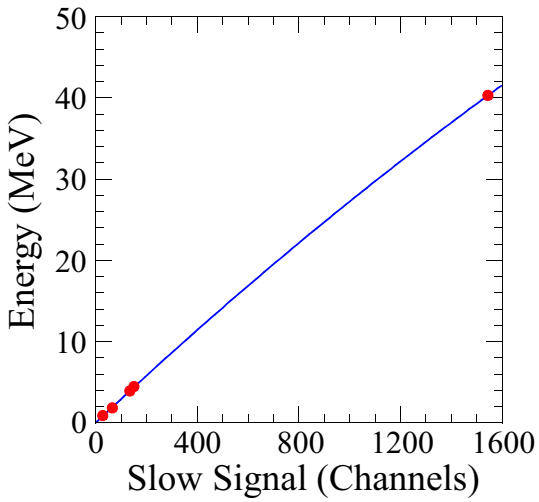

Figure 3.2: Typical energy calibration curve for a BaF_2 detector. The solid curve is the result of a quadratic fit through the points shown. The points were obtained as explained in the text.

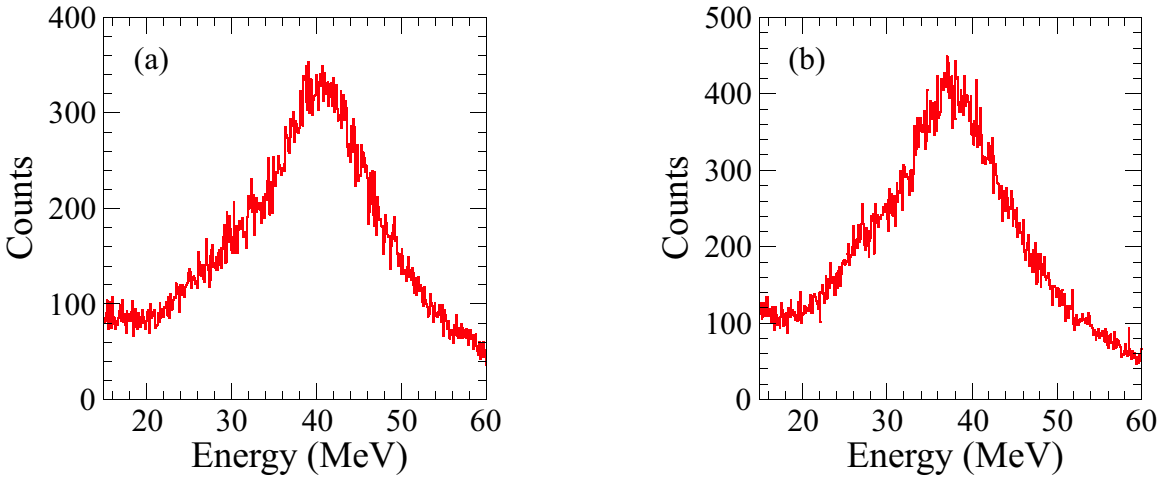

Figure 3.3: Calibrated cosmic-ray spectra. Panel (a) is for an ORNL/TAMU detector, while panel (b) is for an MSU detector.

which was easily determined from the frequency of the pulser. With this information, the time gains of the individual channels in the electronics were matched. With the gains matched, a reference point was still needed to complete the time calibration.

The reference point to complete the calibration was obtained from actual run data. The time spectrum of each individual detector contains a prompt peak as well as random peaks (Fig. 3.4). The prompt peak corresponds to events that are correlated with the current beam burst. The random peaks arise because of the width of the gates

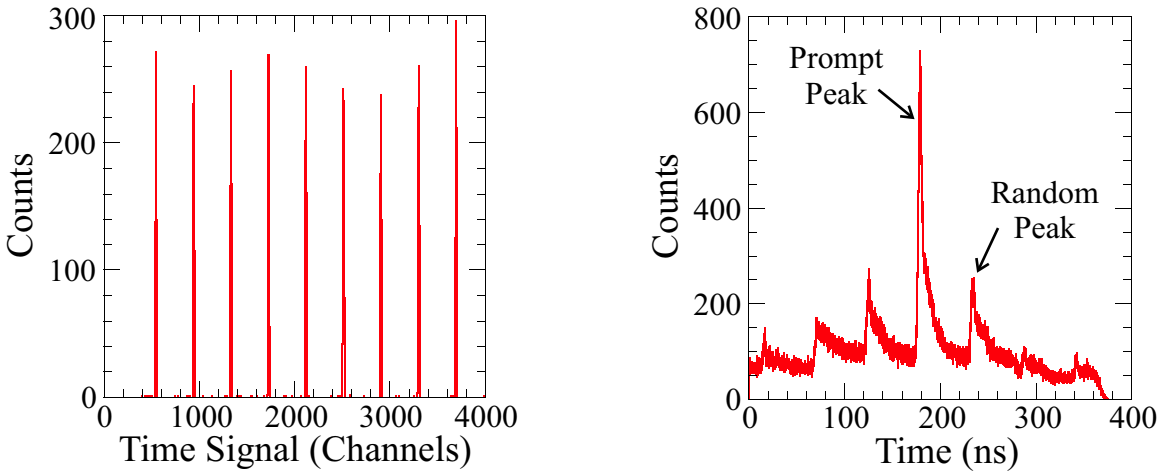

Figure 3.4: Time spectra used to calibrate the BaF_2 array. Left: Pulser data used to gain match the individual electronic channels. Right: Time spectra from data used as reference point. The prompt peak is indicated, as is a random peak.

used in the electronics. The width is sufficiently large for events from either previous or later beam bursts to trigger the acquisition. These events are not correlated with the current beam burst, and the occurrence of such events is random. The reference point used in the calibration corresponds to the centroid of the prompt peak.

The time information from the BaF_2 detectors was used in conjunction with the time between the RF and the E1 scintillator in the S800 focal plane. The accuracy of the BaF_2 time, when measured relative to the E1 scintillator, was insufficient to resolve the γ rays from the neutrons. By subtracting the time between the RF and E1 scintillator from the BaF_2 times, the times were relative to the cyclotron RF. The resulting resolution with this reference point was good enough to resolve the γ rays and neutrons.

3.1.2 CsI Array

The CsI detectors were calibrated for time in the exact same manner as the BaF_2 array (see Sec. 3.1.1). The individual gains were matched from detector to detector with pulser data, while the prompt peak resulting from detected charged particles

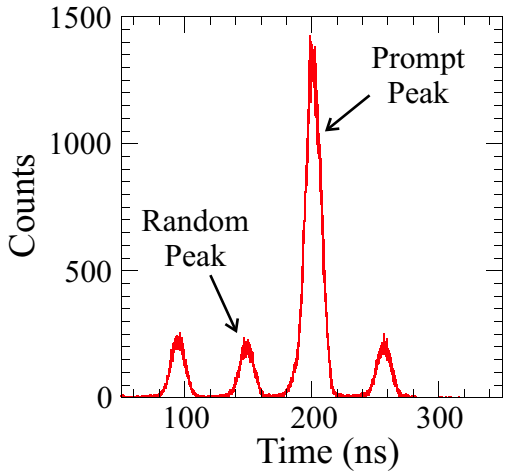

Figure 3.5: Calibrated time spectrum from the CsI detectors. The prompt and random peaks are indicated in the spectrum.

was used as the reference point. The calibrated time spectrum is shown in Fig. 3.5.

The individual CsI detectors were calibrated for energy. Energy calibrations were performed for α particles and protons. It was necessary to have a separate calibration for each type of particle as the response of the detector is not the same for different particles. For the calibration process, the CsI detectors were removed from their position during the run and stacked into a holder. The holder was then placed into the path of the beam. To get calibration points, beams of protons and alphas were used. To get enough points for calibration, the beams were degraded with the use of aluminum. Additionally, the $B\rho$ was varied. Two different degraders were used. The two degraders had thicknesses of 420 mg/cm^2 and 209 mg/cm^2. The values for $B\rho$ varied between 0.65 Tm and 1.28 Tm. In the case of the α calibration, a source of ^{232}U was also used. A typical calibration for both proton and α particles is shown in Fig. 3.6. In the case of the protons, a linear fit gave a good fit to the calibration points. A quadratic fit was needed for the α calibration.

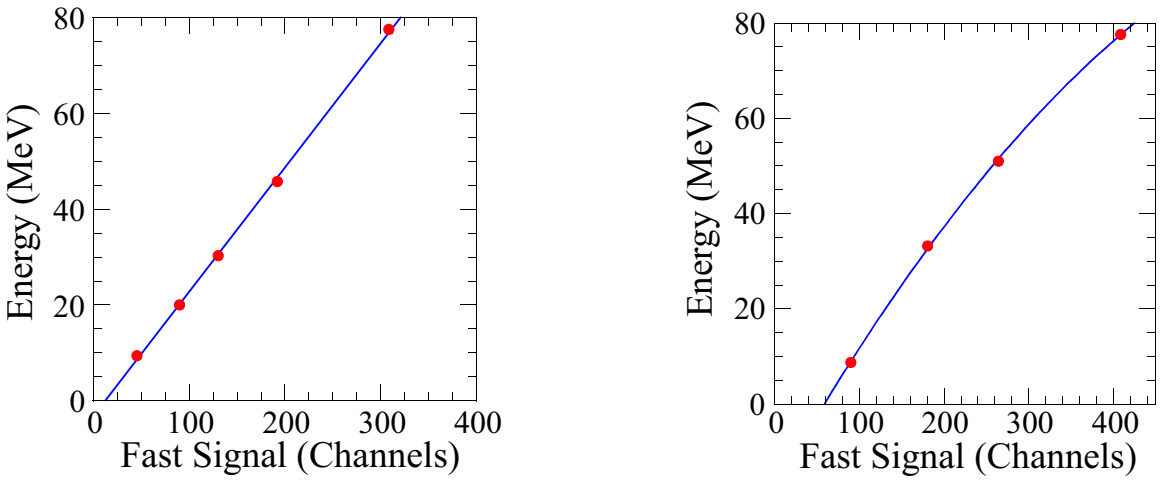

Figure 3.6: Calibration curves for one of the CsI detectors. The points were obtained as explained in the text. The solid curve in each panel shows the resulting fit through the points. Left: Proton calibration. Right: α calibration.

3.1.3 CRDC Detectors

The two CRDC detectors were calibrated for position in both the dispersive (x) and non-dispersive (y) directions. This was accomplished with the use of a mask. Each detector had its own mask, and each mask had holes and slits in it. The position of the holes and slits was known. With the masks in place, the beam only struck the detector where the holes and slits reside, as the mask itself was thick enough to stop the beam. This resulted in a spectrum that was used to calibrate the CRDC detectors for position. The spectrum used to calibrate CRDC1 is shown in Fig. 3.7. In the figure, the non-dispersive position is given by S801_TAC, while the dispersive position is given by S801_Cen_Fit.

3.2 S800 Analysis

3.2.1 Particle Identification

The particle identification (PID) in this experiment involved several steps. Typically, a two-dimensional plot of the energy loss of fragments through the ion-chamber versus

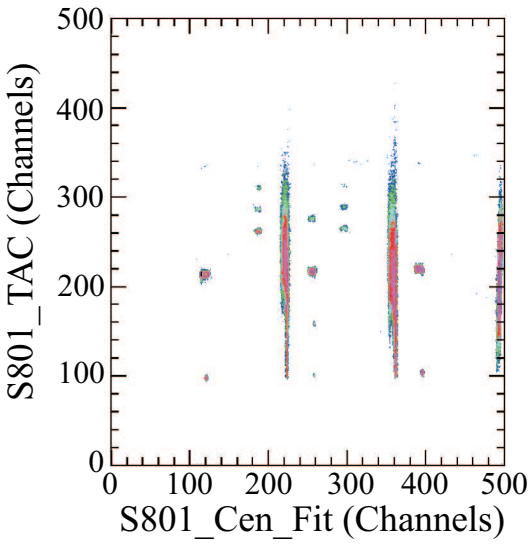

Figure 3.7: The mask spectrum used to calibrate CRDC1 for position in both the dispersive and non-dispersive directions is shown. The points in this spectrum correspond to holes in the mask, while the vertical bands correspond to slits in the mask.

the time-of-flight (TOF) is used for identification purposes. In order for this type of approach to be useful in this analysis, the TOF had to be adjusted. It should be mentioned that the TOF was started with the cyclotron RF and stopped by the signal from the E1 scintillator. The TOF was adjusted in such a way as to eliminate the dependence on the dispersive angle, θ, for nuclei with similar mass to charge (m/q) ratios. The TOF was subsequently adjusted to eliminate the dependence on the dispersive position for CRDC1 (S801_Cen_Fit) for similar m/q. The general way in which this was done was the following: first, a two-dimensional plot of TOF versus θ (left panel in Fig. 3.8) was created. With this plot, the TOF was adjusted using the following equation:

$$TOF' = TOF[1 + \beta(\theta - \theta_0) + \lambda(\theta - \theta_0)^2]. \tag{3.1}$$

The parameters β, λ, and θ_0 were determined by reading points from the left plot in Fig. 3.8. TOF$'$ was held constant for all points read from the plot for a given m/q in

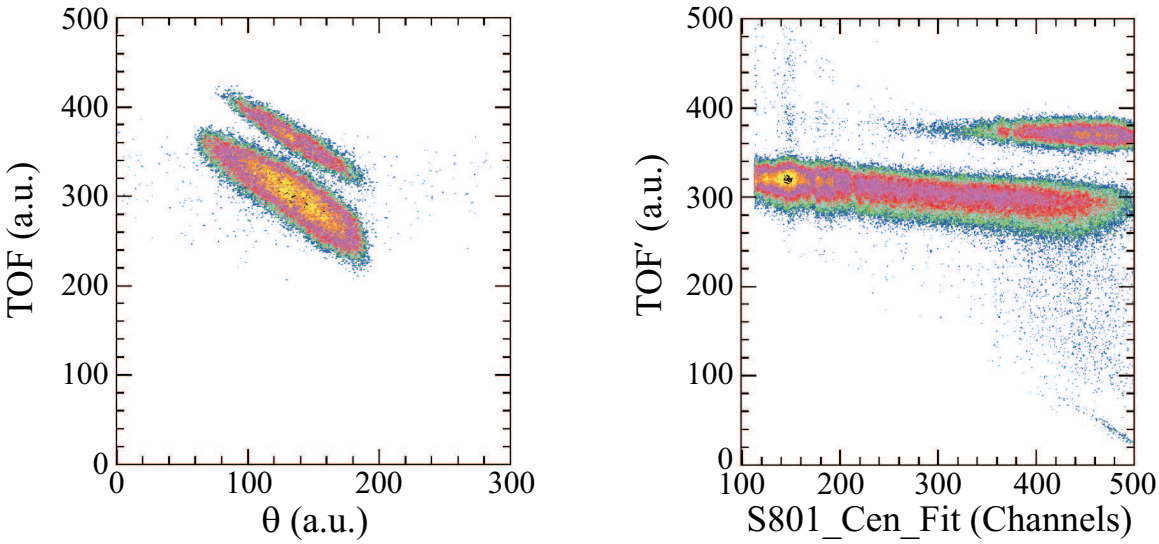

Figure 3.8: Plots used to adjust the TOF parameter for particle identification. Left: TOF vs. θ. Right: TOF vs. CRDC1 dispersive position

this process. Reading off three values for θ, λ, and TOF yielded three equations with three unknowns, which allowed for a simple algebraic solution. The three points were chosen along the center of one of the bands at the beginning, middle, and end of the region. The new parameter, TOF′, was further adjusted from a plot of TOF′ versus S801_Cen_Fit (X). This plot is shown in the right side of Fig. 3.8. The equation used in this step is similar to Eqn. 3.1, and is:

$$TOF'' = TOF'[1 + \zeta(X - X_0)]. \tag{3.2}$$

This time there are only two unknowns, namely ζ and X_0. These parameters were determined in the same fashion as β, λ, and θ_0. The values found for the parameters are shown in Table 3.1.

The new TOF parameter, TOF″, in conjunction with the energy loss of the fragments through the ion-chamber (IC_Sum), allowed for the first step in the PID process. This plot is shown in the right side of Fig. 3.9. Also shown in this figure is a plot of IC_Sum vs. TOF. This plot shows that the adjustment to the TOF parameter was indeed necessary, as it was impossible to distinguish between isotopes without it. The

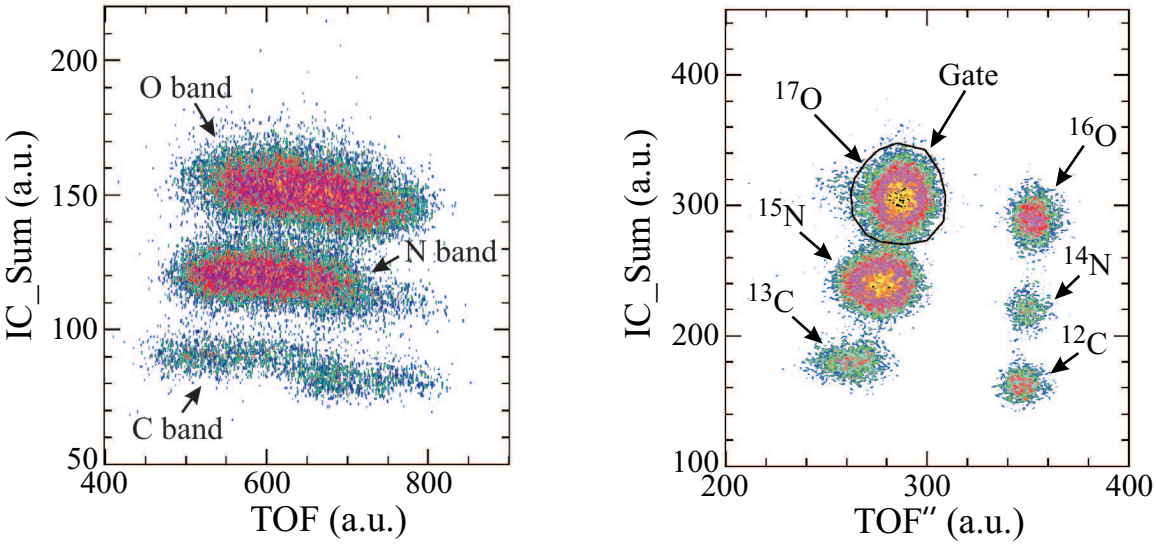

Figure 3.9: Left: Plot of IC_Sum vs. TOF. Right: Plot of IC_Sum vs. TOF″. This plot was used initially for particle identification. The gate used is shown. The identified isotopes are also indicated.

initial gate used for PID is shown in the right side of Fig. 3.9. A new gate was made for each individual run. This was to account for any drifts in the RF.

A second gate was placed on a plot of IC_Sum versus the geometric mean of E1. This is shown in the right side of Fig. 3.10. For comparison, the left side of Fig. 3.10 shows the same plot before the gate shown in Fig. 3.9 was implemented. The geometric mean for E1 is given by:

$$geometric\,mean\ E1 = \sqrt{(E1\_Up)(E1\_Down)}, \tag{3.3}$$

Table 3.1: Parameters used to adjust the TOF parameter for particle identification. All units are arbitrary.

Parameter	Value
β	5.5×10^{-4}
λ	4.17×10^{-7}
θ_0	502.181
ζ	2.56×10^{-5}
X_0	5749.65

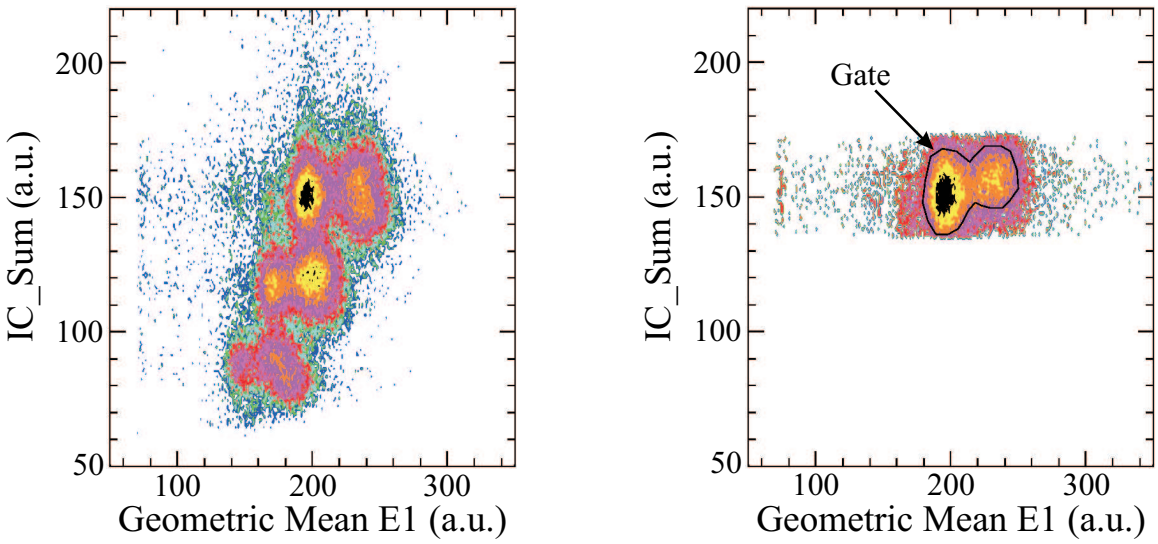

Figure 3.10: Left: Plot of IC_Sum vs. Geometric Mean E1 before the initial gate shown in Fig. 3.9 was implemented. Right: Plot of IC_Sum vs. Geometric Mean E1 after the gate shown in Fig. 3.9 was implemented. This plot ultimately gave particle identification. The gate used for final particle identification is shown.

where $E1\_Up$ and $E1\_Down$ are the signals from the top and bottom PMTs, respectively. Typically, the geometric mean is not position sensitive; however, this was not the case in this experiment. ^{17}O fragments that hit the left half of the E1 scintillator resulted in a different geometric mean than fragments which hit the right half. This is evident in the right side of Fig. 3.10. Clearly there are two intense regions in this plot. ^{17}O fragments hitting the center of E1 show up in this plot between the two regions enclosed by the gate. This effect may have been due to some dead area in the scintillator. This gate, in conjunction with the other (right side of Fig. 3.9), ultimately allowed for inelastically scattered ^{17}O events to be isolated.

3.2.2 Fragment Energy Loss

The energy loss of ^{17}O fragments was determined with the S800 magnetic spectrograph. The information collected from the CRDC detectors completely determined the trajectory of fragments reaching the focal plane. The parameters of fragments reaching the focal plane are given by x_f, θ_f, y_f, and ϕ_f. The parameters x_f and y_f

give the position at the focus, while θ_f and ϕ_f give the angles of trajectory in the x-z and y-z planes, respectively. These parameters, along with magnetic field mappings, were used to determine the energy loss.

The magnetic fields created by the magnets within the spectrograph were mapped as described in Ref. [42]. With this information, it was possible to analytically reconstruct the trajectory of fragments with known magnetic rigidity through the S800. The ability to reconstruct the trajectory, coupled with the measured parameters at the focus, allowed for the calculation of quantities that describe the motion of the fragments as they left the target (θ_t, y_t, ϕ_t, δ_t). The quantity δ_t is related to the fragment's kinetic energy. Specifically, the quantity δ_t is given by

$$\delta_t = \frac{E - E_c}{E_c}, \tag{3.4}$$

where E_c is the kinetic energy of fragments traveling along the central axis of the spectrometer. The quantity E_c is determined by

$$B\rho_{S800} = \frac{p_c}{q} = \frac{\sqrt{2mE_c}}{q}. \tag{3.5}$$

The quantities $B\rho_{S800}$, m, and q are the magnetic rigidity setting of the S800, fragment mass, and fragment charge, respectively. The target and focus quantities are related through the matrix equation

$$\begin{pmatrix} \theta_t \\ y_t \\ \phi_t \\ \delta_t \end{pmatrix} = \mathbf{R} \begin{pmatrix} x_f \\ \theta_f \\ y_f \\ \phi_f \end{pmatrix}, \tag{3.6}$$

where $\mathbf{R}$ is the inverse matrix, which is calculated by the code COSY INFINITY [43].

The parameters δ_t and E_c are all that is needed to calculate the energy loss of the

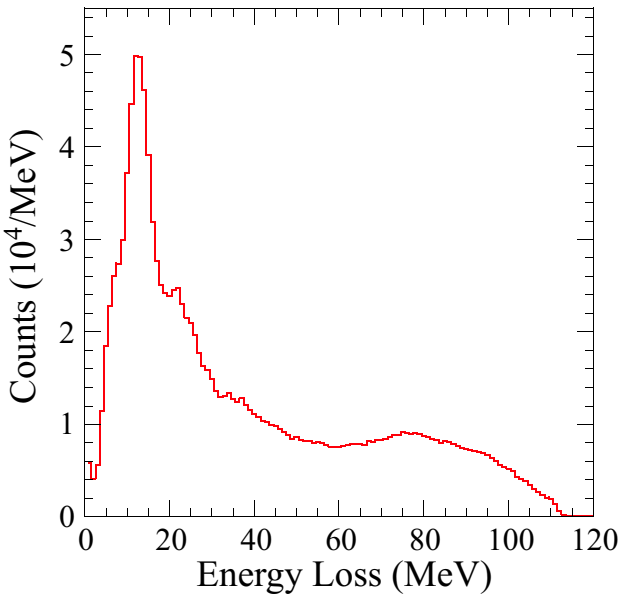

Figure 3.11: The S800 singles energy-loss spectrum is shown for ^{17}O events. The peak at $\sim$ 15 MeV is from the ground-state GDR.

fragments. The energy of the fragments, E_p, is given by

$$E_p = \delta_t E_c + E_c. \tag{3.7}$$

The parameter γ is calculated from this energy. More specifically,

$$\gamma = \frac{1}{\sqrt{1 - \frac{v^2}{c^2}}} = \frac{E_p}{mc^2} + 1, \tag{3.8}$$

where v is the velocity of the fragment and c is the speed of light. Finally, the energy loss (EL) is given by

$$EL = \frac{mc^2}{\gamma}(\gamma_0 - \gamma), \tag{3.9}$$

where γ_0 is calculated in the same manner as γ, except with E_p replaced with E_c. The energy-loss spectrum for S800 singles ^{17}O events is shown in Fig. 3.11.

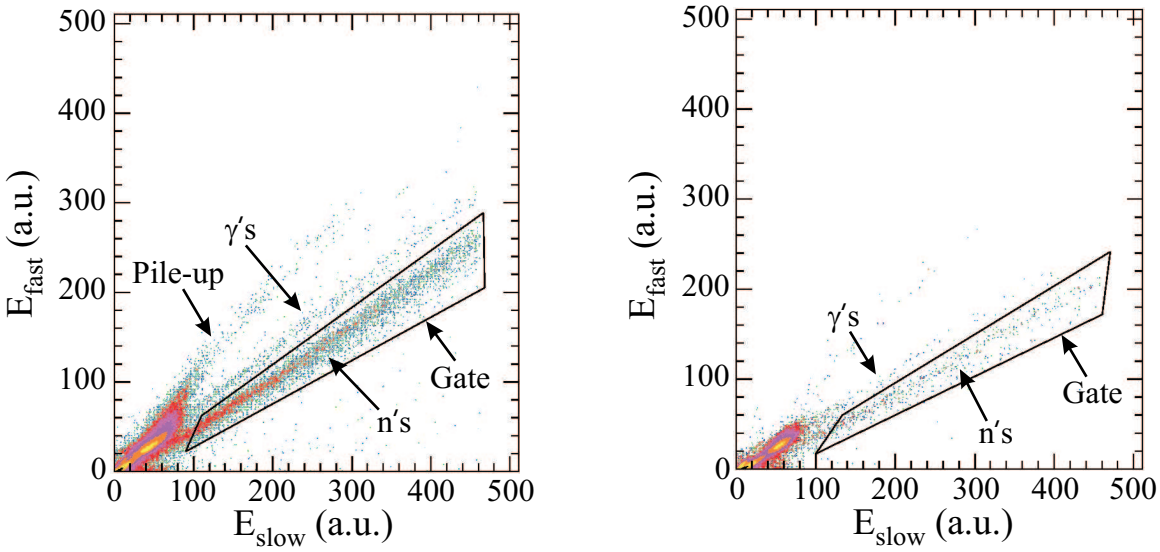

Figure 3.12: Plots used to eliminate high-energy neutrons from the analysis. Both plots show E_{Fast} versus E_{Slow}. Left: Plot for forward detector. Right: Plot for backward detector. The gate used to exclude neutrons is shown in each plot. The bands corresponding to pile-up, neutron, and γ events are also indicated.

3.3 BaF_2 Array Analysis

3.3.1 Selection of γ Rays

In order to study the evolution of the GDR width with temperature, the γ-ray decay spectrum had to be extracted from the data. The excited Sn nucleus predominantly decays by neutron emission at energies above the neutron binding energy. As a result, many neutrons were emitted as the nucleus decayed. The neutrons were detected, along with the γ rays, by the BaF_2 detectors. If the γ-ray decay of the GDR is to be studied, the neutron events must be discriminated against, so that only γ-ray events are considered. The discrimination of neutrons consisted of two parts.

The first step in selecting γ-ray events was to take advantage of the two components of light emitted in BaF_2. The ratio of the fast-to-slow component of light is different for neutrons than it is for γ rays. As a result, it was possible to eliminate many of the neutron events by gating on a plot of the fast versus slow signals. Fig. 3.12 shows such a plot. The gate shown in each side of the plot was used to

exclude events. A separate gate was made for each individual detector. Many more neutrons were emitted in the forward direction than in the backward direction, as evident in the plot. There is also a region that corresponds to pile-up for the forward detector. Pile-up occurs when multiple low-energy γ rays hit the same detector. The occurrence of pile-up is completely random.

In order to eliminate low-energy neutrons, it was necessary to consider the time-of-flight as measured between the individual BaF_2 detectors and the RF (TOF_{BaF_2}). The flight time should be shorter for γ rays than neutrons at low energies, because γ rays move at the speed of light. Hence, by plotting the energy deposited in each detector against the TOF_{BaF_2}, it was possible to eliminate all neutrons from the analysis. The plot used to do this is shown in Fig. 3.13. Fig. 3.13a shows the overall spectrum, while the other plots in Fig. 3.13 show smaller ranges of times. Fig. 3.13b shows the region corresponding to the prompt γ rays, while Fig. 3.13c is for that of the random γ rays. The gate shown in Fig. 3.13b was used for final γ-ray selection. These γ rays were ultimately used to create γ-ray decay spectra. In order to determine the background, and the contribution to the prompt γ rays from the random ones, a second gate was implemented. This gate is shown in Fig. 3.13c. The gate shown here is the same gate as used for the prompt γ rays, except that it is shifted by the time between beam bursts from the cyclotron (54.3 ns). This allowed for the creation of another γ-ray spectrum. This spectrum gave the background and the contribution of randoms. New gates were created for every run to account for any drifts in the RF. The spectra shown in Fig. 3.13 are for 10 runs.

3.3.2 Shower Reconstruction

To improve the response of the BaF_2 array, a shower reconstruction routine was implemented. All BaF_2 events sent to the routine were analyzed in the following way: first, these events were sorted into descending order. Next, the detector with highest

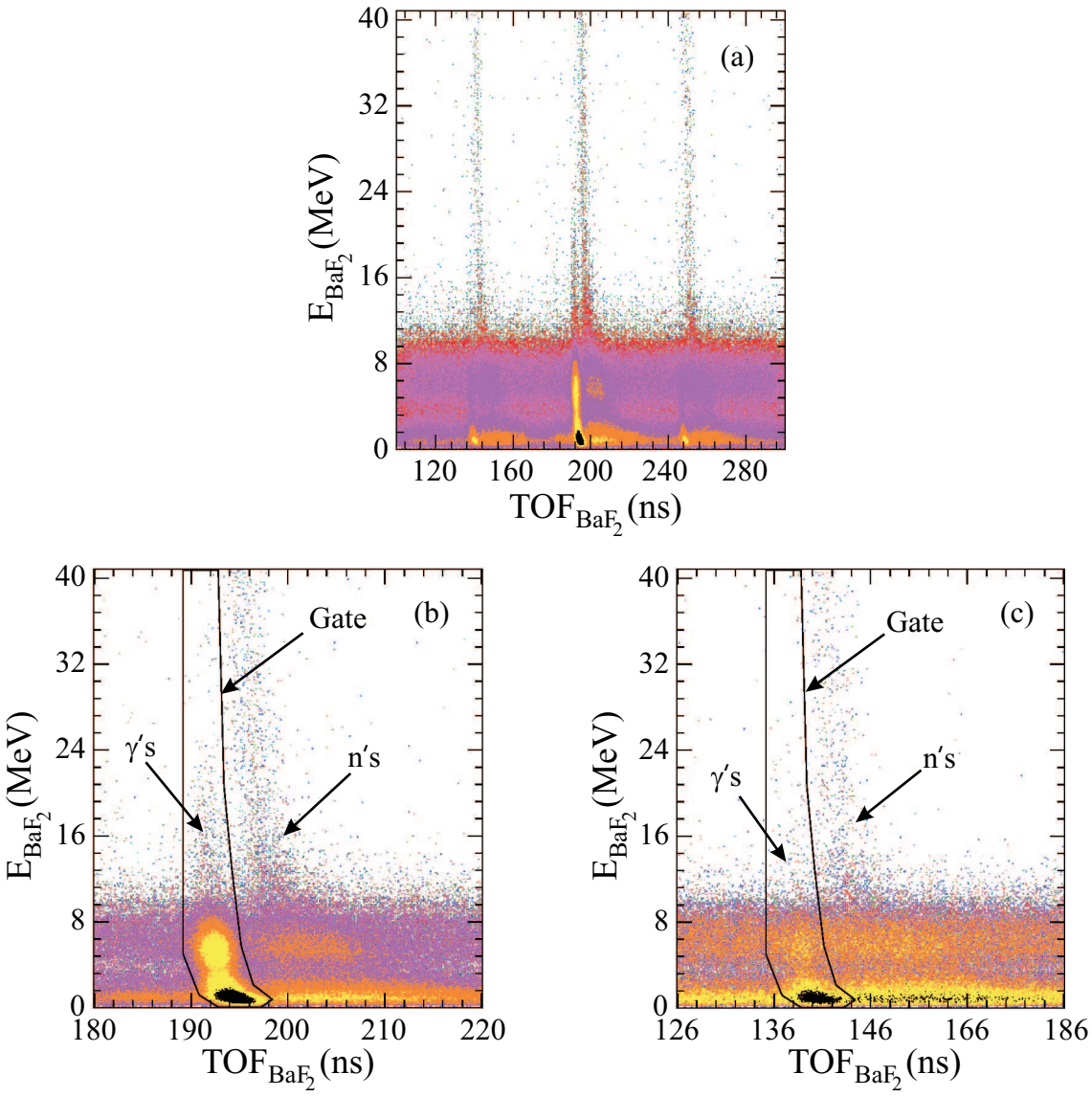

Figure 3.13: Plots used for final γ-ray selection. (a) Full spectrum used in the analysis. (b) Region of spectrum corresponding to prompt γ rays. (c) Region of spectrum corresponding to random γ rays. Neutron and γ-ray events are indicated in panels (b) and (c). The gates used in the analysis are also shown.

energy was assigned as the primary detector in the primary shower. After this, the detector with the second highest energy was considered. If this detector neighbored the primary detector in the primary shower, it was also assigned to the primary shower. Otherwise, it was assigned as the primary detector in a secondary shower. Then the detector with the next highest energy was analyzed. If this detector neighbored any

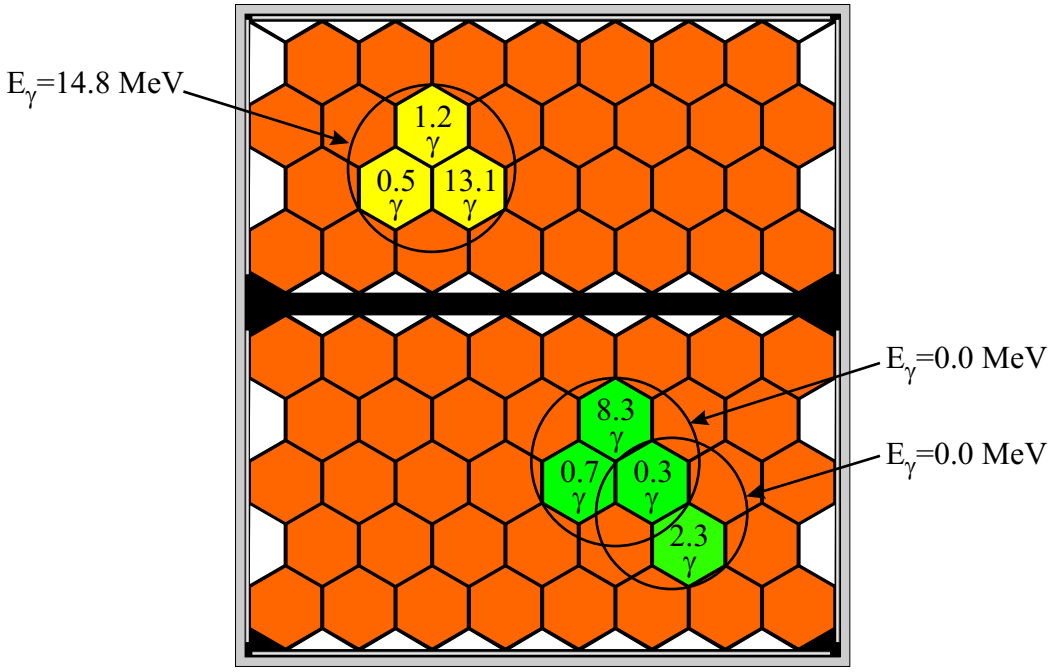

Figure 3.14: Schematic to demonstrate the shower reconstruction process used with the BaF_2 array. An example of both a good shower (yellow) and bad shower (green) are shown.

detectors already assigned to a shower, it was assigned to that shower. Otherwise, it was assigned as the primary detector in a secondary shower. This process was continued until all detectors were considered. Once all detectors were grouped into showers, the energies of detectors belonging to a given shower were added together. This sum gave the total energy of the γ ray (E_γ). If any detector belonged to more than one shower, the summed energy of these showers was rejected by setting the energy to zero. A criterion in the add back process was that the energy must decrease when moving away from the primary detector. Fig. 3.14 illustrates the process. The detectors colored yellow were added together, and signify a good shower. The detectors colored green signify a rejected shower. Analysis of all the data showed that only one in 600 showers was rejected.

The effect of the reconstruction process is evident in Fig. 3.15. The blue curve in Fig. 3.15 shows the spectrum resulting from PuBe source data, when no reconstruction was performed. The red curve in Fig. 3.15 also shows a spectrum from PuBe source

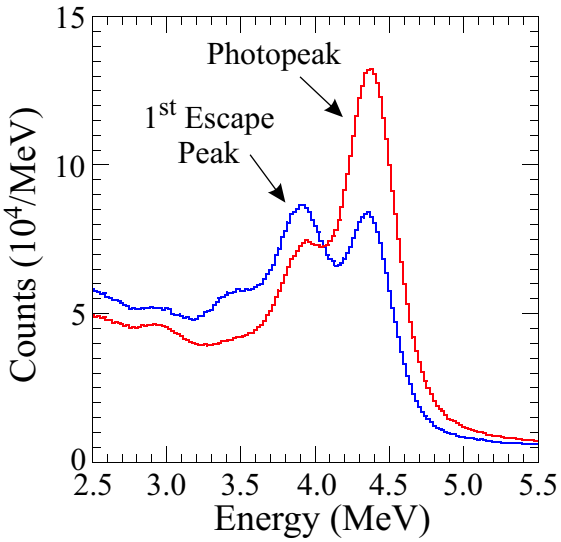

Figure 3.15: Spectra from PuBe source to show the effects of reconstruction. The blue spectrum is the result of histogramming each individual detector energy, while the red spectrum uses the reconstruction routine.

data. For this spectrum, events were analyzed using the reconstruction routine. The first escape peak is significantly lower for the red spectrum as compared to the blue spectrum. Also, the photopeak is much improved in the red spectrum.

3.3.3 γ-ray Decay Spectra

The final step in the BaF_2 data analysis was to extract γ-ray decay spectra at various projectile energy losses. To ensure that detected γ rays were correlated with the projectile energy loss, only events where there was both a BaF_2 and S800 event in coincidence were considered. With E_γ and projectile energy loss correlated, it was relatively simple to extract decay spectra for different energy losses.

The γ-ray spectra were extracted by making cuts on projectile energy loss. The cuts were made in 10 MeV steps from 20–90 MeV (i.e. 20–30, 30–40, ... , 80–90 MeV). Additionally, the γ-ray spectrum corresponding to decays to the ground state was measured. In all, eight spectra were extracted. For the 20–30 MeV energy cut, special care had to be taken.

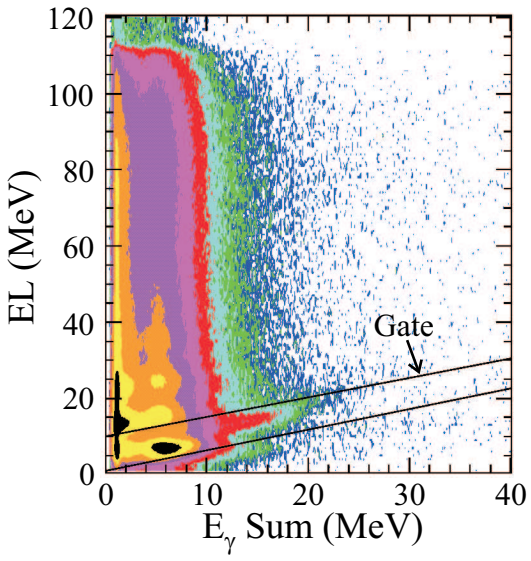

Figure 3.16: The fragment energy loss is plotted against the sum of detected γ rays. This spectrum was used to exclude γ decays to the ground state. The gate used to exclude γ-ray events that decay to the ground state is shown.

In the case of the 20–30 MeV energy loss cut, decays to the ground state were of concern. To study the GDR built on excited states, these events had to be rejected. The first step in eliminating these events was to sum up all γ-ray energies (E_γ Sum) from each event and plot them against energy loss, as shown in Fig. 3.16. This plot allowed for decays to the ground state to be eliminated by gating on the diagonal band, as the diagonal band corresponds to these decays. All events in this gate were excluded from the 20–30 MeV energy loss analysis. The spectra in Fig. 3.17 show the result of the analysis in the 20–30 MeV energy loss region. The effect of excluding events in the gate just described only affects the final spectrum for γ-ray energies greater than 20 MeV. At these energies, the contribution to the final γ-ray spectrum from the GDR built on excited states is minimal.

The events in the gate shown in Fig. 3.16 allowed for the γ-ray spectrum corresponding to decays to the ground state to be extracted. The events in this gate were histogrammed. It should be mentioned that E_γ was histogrammed, and not the sum of E_γ.

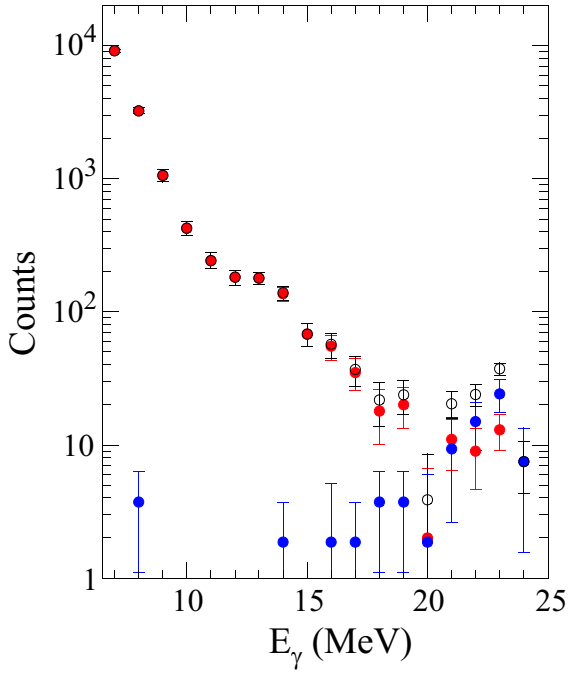

Figure 3.17: Breakdown of γ-ray spectrum corresponding to 20–30 MeV energy loss. The solid red circles exclude events from the gate in Fig. 3.16, while the blue circles are events from this gate. The open black circles show the resulting spectrum if no gate would have been implemented.

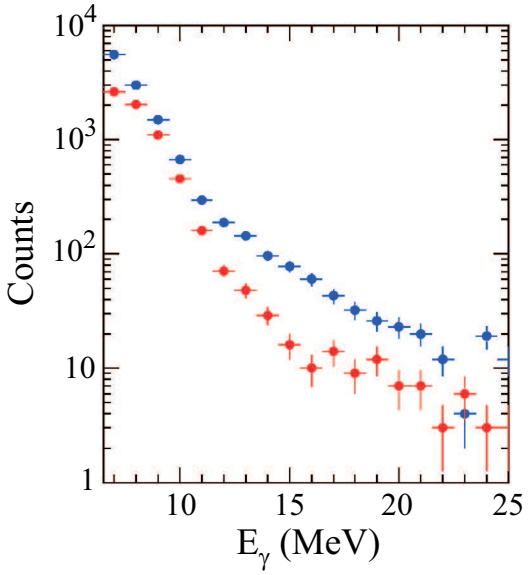

Figure 3.18: Raw and random γ-ray spectrum for energy losses of 80–90 MeV. The blue spectrum is the raw spectrum, while the red spectrum is the random spectrum. The errors in the vertical direction are statistical, while the horizontal error bars are to show the width of the histogram bins.

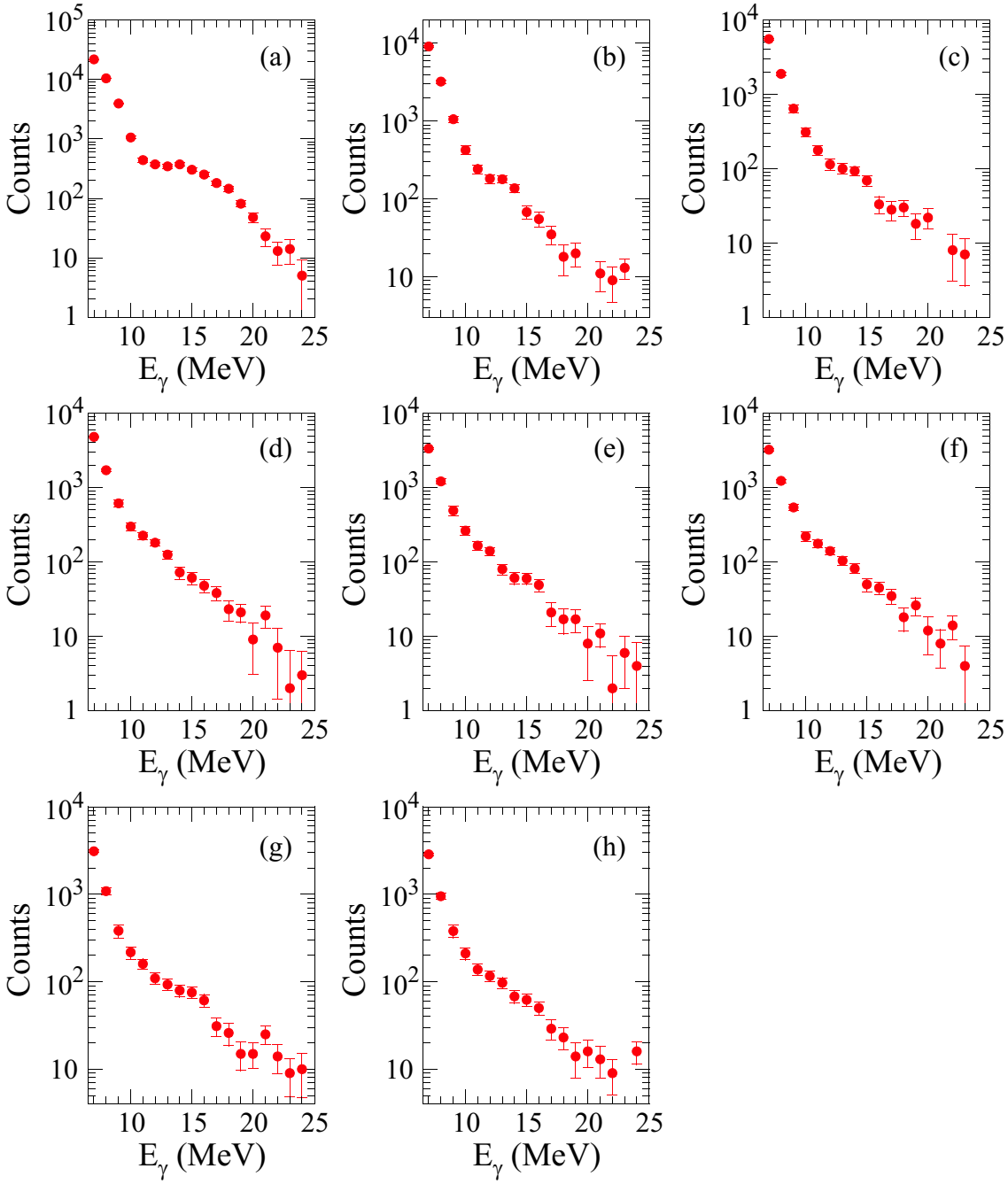

Figure 3.19: γ-ray decay spectra. Panel (a) corresponds to decays to the ground state. Panel (b) corresponds to energy losses of 20–30 MeV, (c) 30–40 MeV, (d) 40–50 MeV, (e) 50–60 MeV, (f) 60–70 MeV, (g) 70–80 MeV, (h) 80–90 MeV.

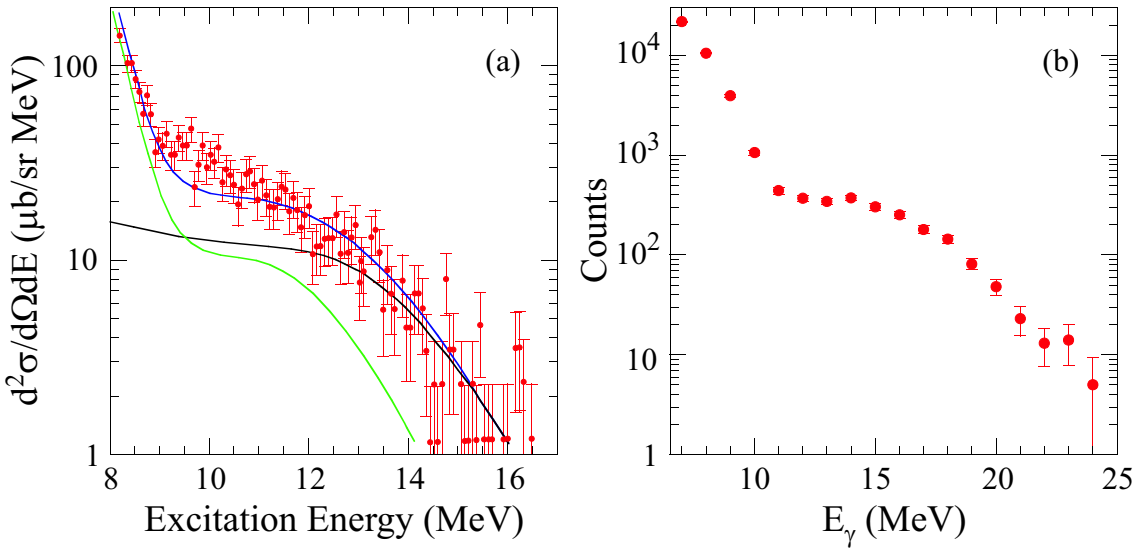

Figure 3.20: Panel (a) shows the ground state γ-ray spectrum measured by Ref. [23] for ^{208}Pb. The green curve shows a calculation for the yield of direct decays to the ground state, while the black curve shows compound decays. The solid blue curve is the sum of the blue and green curves. Panel (b) shows the ground-state spectrum from this work.

The final γ-ray spectrum for each energy loss cut was obtained by creating both a raw and random (background) spectrum. The raw spectrum was made by considering prompt γ-ray events (gate in Fig. 3.13b). These events were sent to the reconstruction routine described in the previous section. All γ-ray energies were then histogrammed, which resulted in the raw spectrum. The background contribution to the raw spectrum was determined in a similar way, with the difference being which events were sent to the reconstruction routine. In the case of the background, the events considered came from the gate shown in Fig. 3.13c. Fig. 3.18 shows both the raw and background spectrum corresponding to the 80–90 MeV energy-loss region. The final spectrum was obtained by subtracting the background spectrum from the raw spectrum.

The final γ-ray decay spectra for all energy losses considered are shown in Fig. 3.19. The γ-ray spectrum corresponding to decays to the ground state (Fig. 3.19a) was not analyzed in this work. Not only does this spectrum contain decays directly to the ground state, but it also contains decays that first go through excited states before

finally decaying to the ground state. It is extremely difficult to disentangle the different contributions. The only such analysis of this type has been performed on Pb [23].

Despite the fact that the ground state γ-ray spectrum was not analyzed quantitatively, it is still interesting to compare this spectrum to the one in Ref. [23]. Both spectra are shown in Fig. 3.20. The spectrum from this work (Fig. 3.20b) has a very similar shape to the blue curve in Fig. 3.20a. This indicates the presence of both direct and compound decays to the ground state.

3.4 CsI Array Analysis

3.4.1 Identification of Events

The CsI array was used to detect charged particles. In order to study the charged particles, the various particles were identified. In particular, α and proton events were isolated. As in the case of BaF_2, CsI has two components of light (see Sec. 2.1.2), which allows for pulse shape discrimination. The proton and α particles leave a different ratio of fast-to-slow energy, and plotting these signals against each other allowed for the separation of these events. Two such plots are shown in Fig. 3.21. In Fig. 3.21a, more particles were detected than in Fig. 3.21b. This is as expected, since the detector corresponding to Fig. 3.21a is more forward in the array. The spectra shown in Fig. 3.21 are not gated on ^{17}O events. The only requirement in making these plots was that a charged particle came in coincidence with a fragment in the S800 focal plane.

The plots in Fig. 3.21 are very useful for identification purposes. However, even with these plots it is difficult to gate on the different events. The bands in the plots are very close together. A larger separation between the bands can be achieved by manipulating the fast signal. The fast signal (E_{fast}) was transformed according to

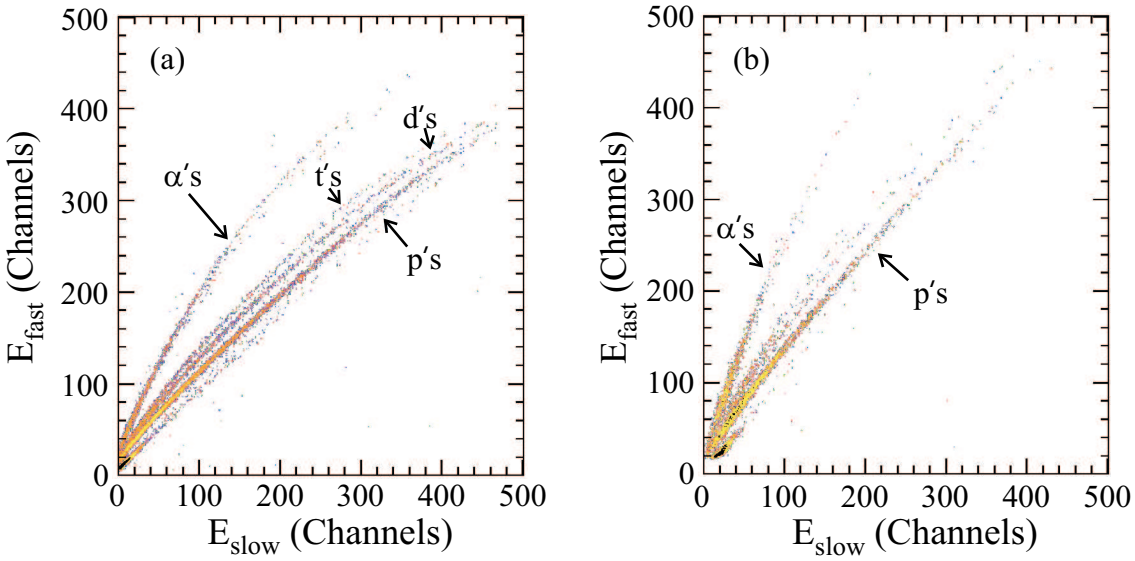

Figure 3.21: CsI fast vs. slow spectra. The spectrum in panel (a) was measured at a scattering angle of 60°, while in panel (b) the scattering angle was 150°. The bands corresponding to α, triton, deuteron, proton events are indicated. These plots were transformed, and used for identification purposes.

Ref. [4]. The transformed signal (E'_{fast}) is given by

$$E'_{fast} = \frac{y_2 - y}{y_2 - y_1}. \tag{3.10}$$

The quantities y, y_2, and y_1 are defined in Fig. 3.22, and are dependent on the boundary lines (blue lines in Fig. 3.22). The placement of these lines was such that all data was between them.

The transformation of the fast signal allowed for gates to be made on proton and α particles. The plots in Fig. 3.23 show the result. The separation between the bands corresponding to the proton and α particles is much better in this plot than in Fig. 3.21. Ultimately, gates were only implemented for proton events. Once ^{17}O events were gated on, very few α particles were detected. Also, only 4% of the events shown in Fig. 3.21 and Fig. 3.23 were left after gating on ^{17}O.

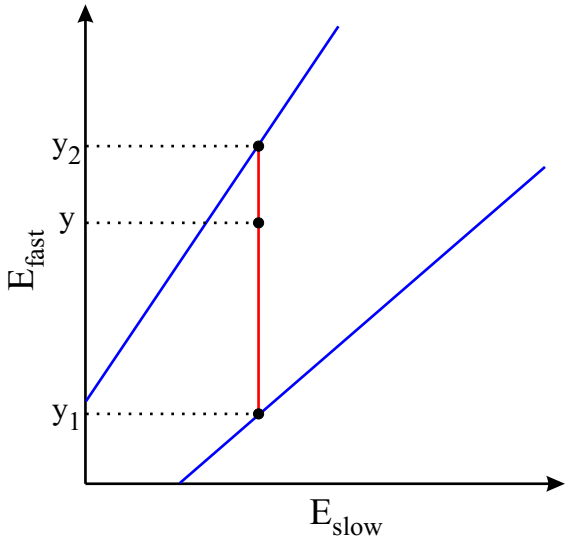

Figure 3.22: Illustration of parameters used to transform E_{fast}. The parameters y, y_1, and y_2 were used to transform E_{fast} as shown in Eqn. 3.10.

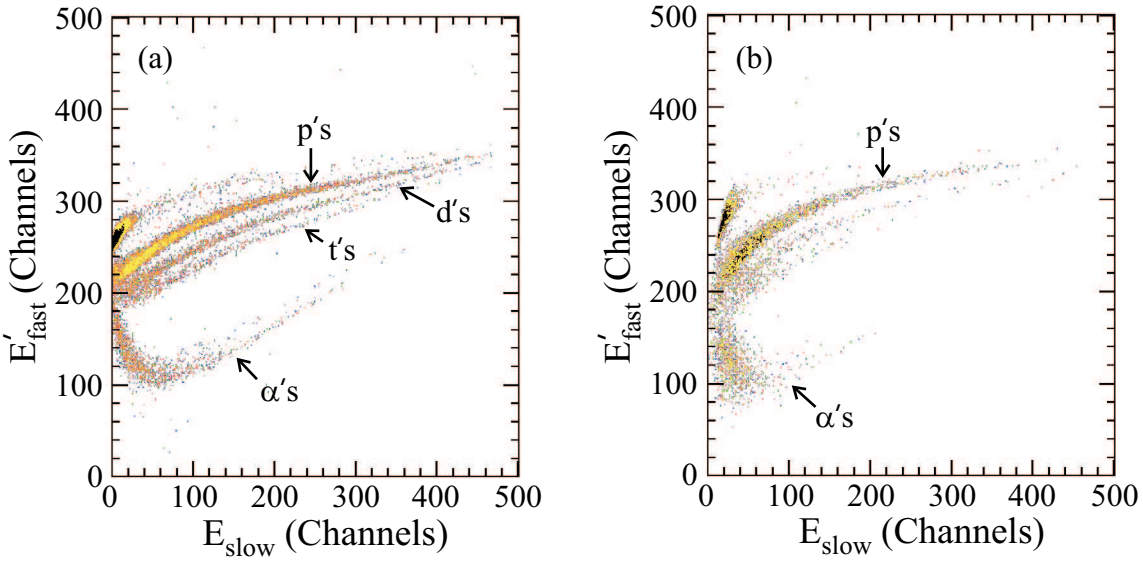

Figure 3.23: Transformed CsI spectra for charged-particle identification. The transformation was performed on the plots shown in Fig. 3.21. As in Fig. 3.21, α, proton, triton, and deuteron events are indicated. Ultimately gates were places on the proton bands.

3.4.2 Proton Spectra

Proton events were isolated in order to try to determine the initial excitation energy of the target nucleus. In a past experiment, the correlation between projectile energy loss and target excitation energy was studied [36]. It was hoped that a similar approach

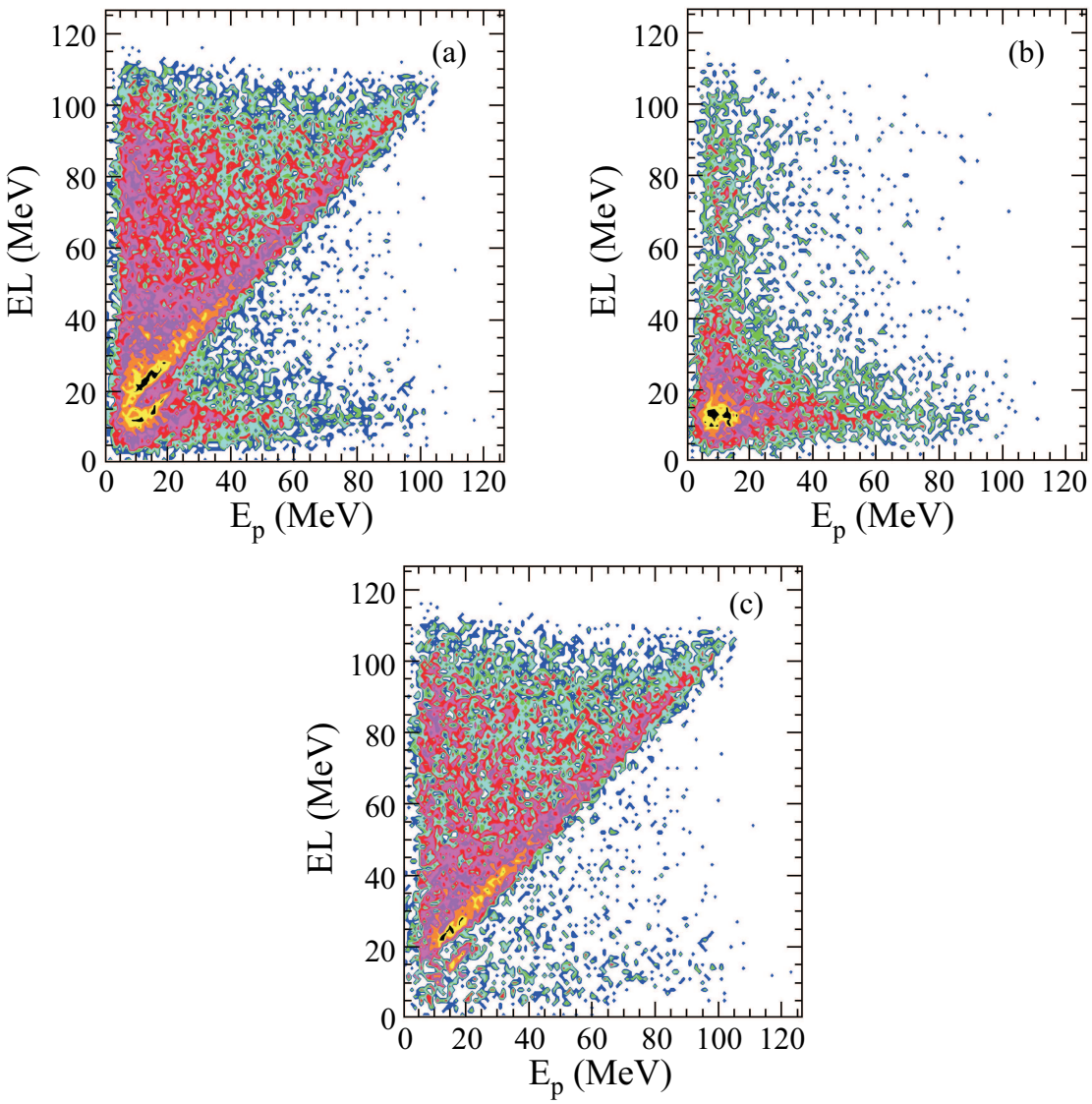

Figure 3.24: Plot of energy loss vs. proton energy for all CsI detectors. Panel (a) shows the resulting spectrum from prompt events, while (b) shows the random events. Panel (c) shows the random subtracted spectrum.

could be used here, by measuring proton spectra.

The fragment energy loss was correlated with the detected protons. Since the energy loss and proton energy were known, it was possible to construct a plot of fragment energy loss (EL) against proton energy (E_p). This plot is shown in Fig. 3.24, and allowed for the proton energy spectrum to be extracted as a function of energy loss.

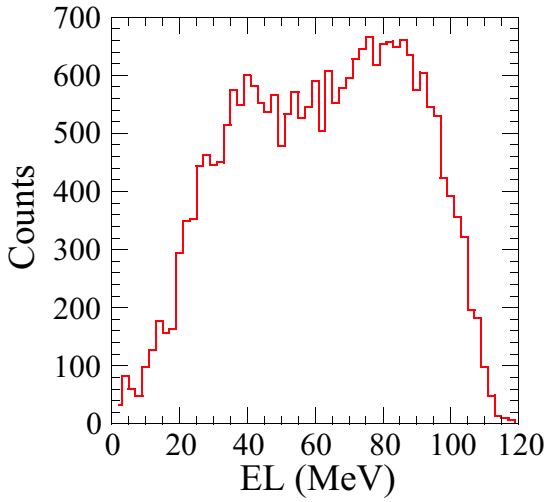

Figure 3.25: The fragment energy loss in coincidence with proton events is shown. This spectrum is the projection onto the energy-loss axis from Fig. 3.24c. The broad peak at 80 MeV is indicative of pickup-decay reactions.

Protons due to knockout and pickup-decay reactions were of concern. Pickup-decay reactions occur when the ^{17}O projectile picks up a proton from the target, and subsequently decays by the emission of a proton. Knockout reactions occur when the projectile knocks a proton out of the target.

The presence of knockout and pickup-decay reactions was investigated by projecting Fig. 3.24c on to the EL axis. This is shown in Fig. 3.25, and gives the energy loss distribution associated with the detected protons. There is clearly a broad peak in this spectrum at 80 MeV, which indicates the presence of pickup-decay reactions. There is also evidence for knockout reactions in Fig. 3.24c. The energy of the emitted protons ranges from a couple of MeV all the way up to the projectile energy loss. The presence of knockout and pickup-decay events in the CsI array should be limited to forward scattering angles. To eliminate these events from the analysis, only backward detectors could be considered.

Plotting the fragment energy loss against the proton energy for individual detectors gives an indication of whether or not knockout and pickup-decay reactions can be eliminated by considering only backward detectors. The spectrum shown in

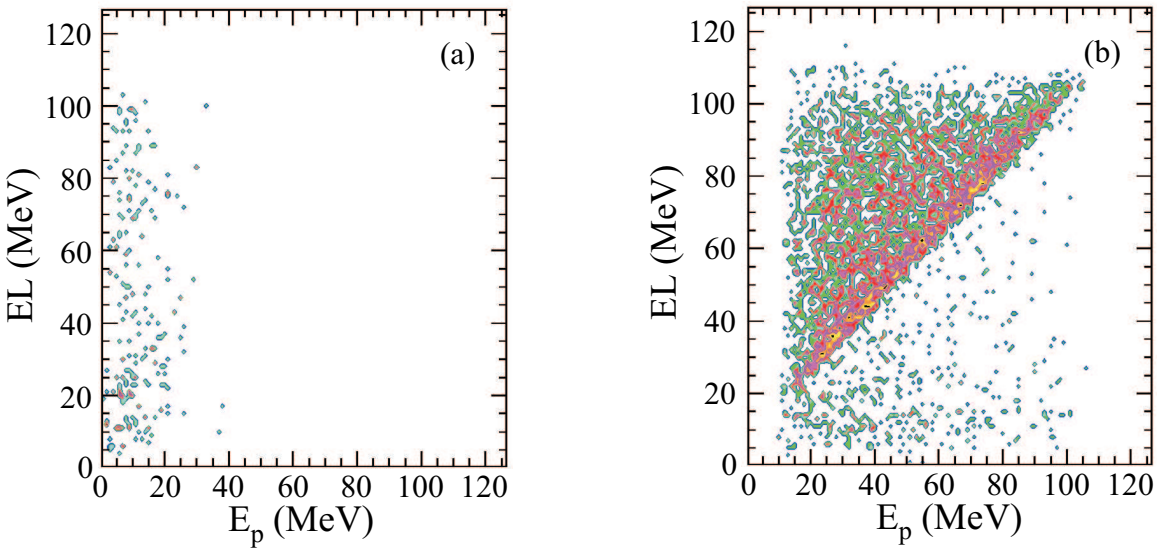

Figure 3.26: Plot of energy loss vs. proton energy. Panel (a) shows the spectrum from the backward most detector, while (b) shows the same for the forward most detector.

Fig. 3.26a was measured at a scattering angle of 180°, while in Fig. 3.26b the scattering angle was 30°. The spectrum measured at backward angles is much different than the one at forward angles, as the high-energy protons are almost completely absent from the spectrum from the backward detector. It appears that protons originating from knockout and pickup-decay reactions can be eliminated by considering only backward detectors.

The final proton spectra shown in Fig. 3.27 were extracted by only considering detectors covering scattering angles between 120° and 180°. The proton spectra were extracted as a function of excitation energy. Unfortunately, the statistics are poor. As a result of the poor statistics, this data could not be used to determine the initial excitation energy of the target nucleus.

Although the CsI data was not very useful in this experiment, it does show that detection of charged particles in the decay of the excited nucleus in GDR studies is feasible. If a similar approach is to be used in future experiments, the solid angle coverage of the CsI array should be increased. This is easily accomplished by adding more detectors to the array. Additionally, the array should primarily cover backward

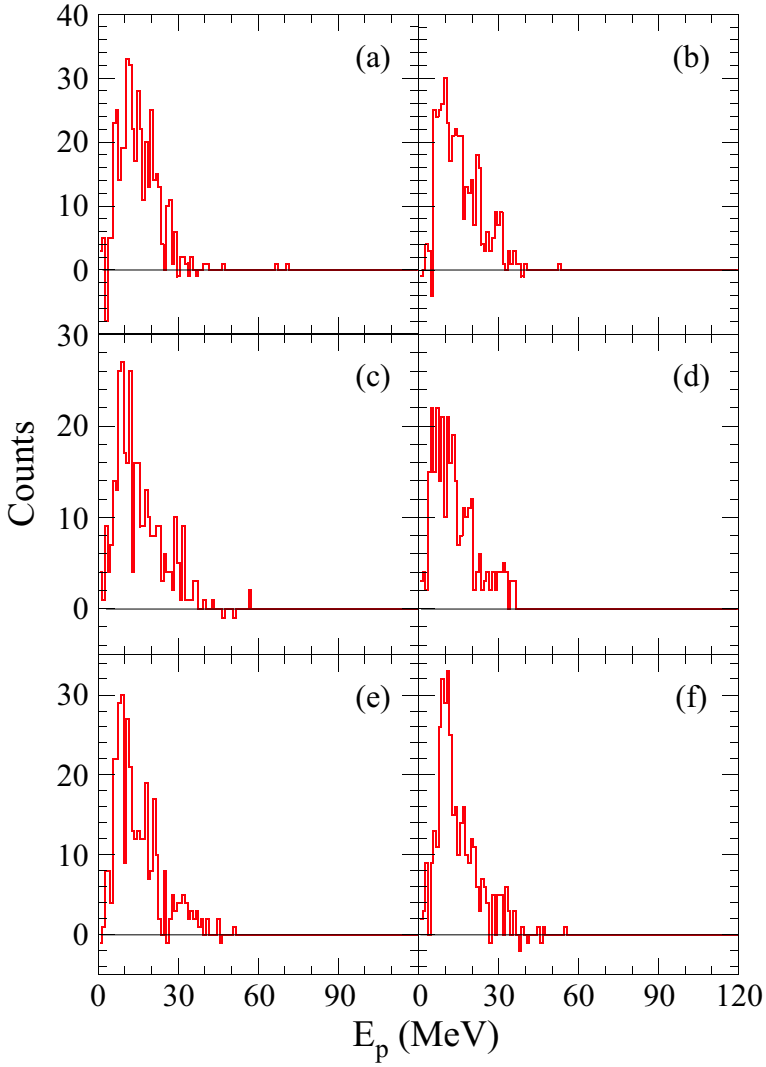

Figure 3.27: Proton energy spectra. The panels correspond to the following projectile energy losses: (a) 30–40 MeV, (b) 40–50 MeV, (c) 50–60 MeV, (d) 60–70 MeV, (e) 70–80 MeV, and (f) 80–90 MeV.

angles. As mentioned earlier, the presence of knockout and pickup-decay reactions is very small at backward scattering angles.

Chapter 4

Tools to Interpret the γ-ray Spectra

To interpret the results of the data analysis presented in the last chapter, several tools were needed. It was necessary to perform statistical model calculations. In this experiment bremsstrahlung radiation was also a concern, and had to be dealt with. The response of the BaF_2 detector arrays was also needed in order to compare theoretical calculations with data. Finally, the nuclear temperature had to be calculated in order to compare this data with previous measurements. In order to calculate the temperature, it was necessary to determine the mean excitation energy of the nucleus along the GDR decay.

4.1 Statistical Model Calculations

The fundamental assumption of the statistical model for the decay of an excited nucleus is that all relevant nuclear degrees of freedom are equilibrated before the decay can take place [3]. The computer code used to perform the calculations was CASCADE [44,45]. In this code, the user specifies the initial population of the excited nucleus in terms of energy and angular momentum. Based on the initial population,

the code calculates a final decay spectrum for alpha, proton, neutron, and γ-ray decay. These spectra are output according to the amount of the total initial cross section that went into each decay. It was the γ-ray decay spectrum from these calculations that was eventually compared with data. The relative probability of a given nucleus decaying by alpha, proton, neutron, or gamma emission is dependent on the relative decay rates as calculated in the code.

4.1.1 Initial Population of Nucleus

In past inelastic-scattering experiments, the energy loss of scattered fragments has been used to determine the initial excitation energy of the nucleus. In these experiments, the initial excitation energy was equated directly to the fragment energy loss [25, 27]. This procedure has since been shown to be inaccurate [36, 37]. A significant range of energies are populated well below that of the energy losses considered, as evident by the forward CsI detectors (see Fig. 3.24c). This becomes more and more problematic as higher and higher energy losses are considered.

An experiment was performed to investigate the correlation of energy loss and excitation energy. This study was performed with the use of α particles as the projectile, and ^{209}Bi as the target [36, 37]. Although the projectile and target used here differ, the results of the study can be used to aid in the determination of the energy distribution resulting from a given energy loss. Table 4.1 shows how the projectile energy loss and average excitation energy ($\overline{E^*}$) compare. As the table indicates, the average excitation energy is less than that of the energy loss for energy losses greater than 55 MeV. The discrepancy between energy loss and excitation energy becomes larger and larger as the energy loss increases.

In addition to the work of Ref. [36], there is another way to get some indication of the correlation between initial excitation energy and energy loss. Fig. 4.1 shows the energy loss spectrum in coincidence with γ rays with energy greater than 4 MeV. The

EL (MeV)	$\overline{E^*}$ (MeV)
45	45
55	55
65	63
75	68
85	74
95	79
105	84

Table 4.1: Summary of the projectile energy loss and target excitation energy. This information is taken from Ref. [36], where the reaction ^{209}Bi(α,α') was investigated.

structures in this plot correspond to the subsequent opening of neutron evaporation channels, and indicate a correlation between energy loss and excitation energy [24]. The structures can clearly be identified up to 35 MeV corresponding to the 4n channel. Thus, the energy loss can be equated directly with the excitation energy up to at least 35 MeV. For energies higher than this, the work of Viesti *et al.* [36] had to be used.

A distribution of excitation energy was determined for a given energy loss by Viesti *et al.* [36]. The distributions relevant to this work are shown in Fig. 4.2 along

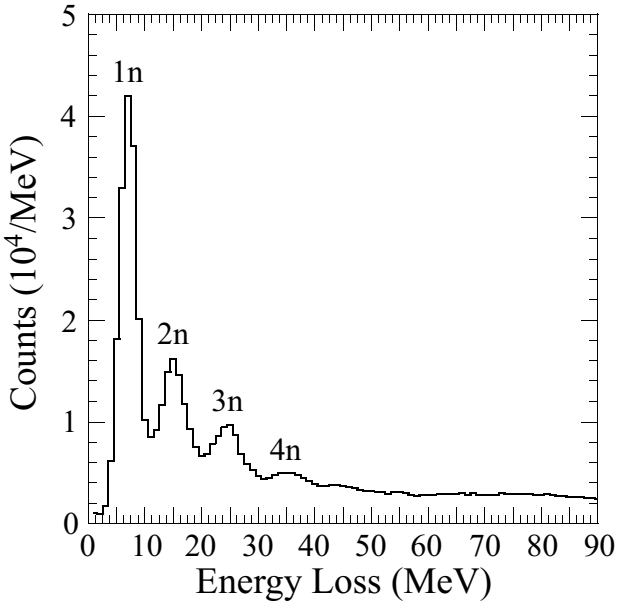

Figure 4.1: Spectrum of inelastically scattered ^{17}O particles in coincidence with γ rays with $E_\gamma \geq 4$ MeV. The successive opening of neutron evaporation channels, up to 4n, is indicated.

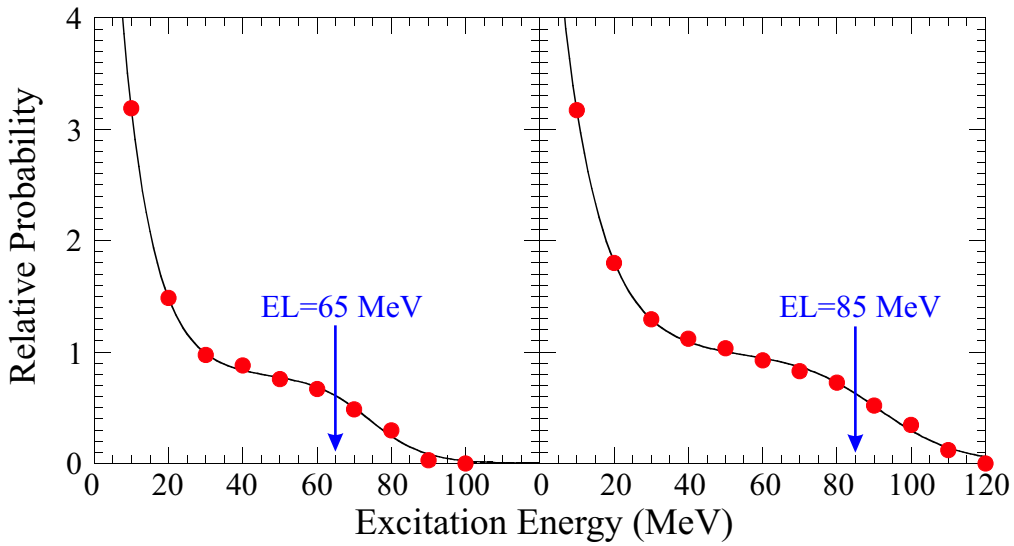

Figure 4.2: Plots adapted from Ref. [36]. The distribution of excitation energy resulting from a given energy loss is shown. The corresponding energy losses are indicated by the arrows in the plots. The points are data from Ref. [36], while the solid curve through the points is a fit.

with the corresponding energy loss. All distributions from Ref. [36] have a low energy tail. This tail is predominantly due to knockout and pickup-decay reactions.

The contribution of knockout and pickup-decay reactions is expected to be much lower in heavy-ion scattering than in α scattering [24]. Also, the contribution to the calculated γ-ray spectral shapes from the low-energy tail is negligible for γ-ray energies above 8 MeV. As a result, the low-energy tail was not included in the distributions of excitation energy used in this work. The distributions used are shown in Fig. 4.3. The corresponding energy losses considered are also shown in this figure for comparison. The energy loss distributions shown in Fig. 4.3 were determined from the S800 singles data (see Fig. 4.4). The peak at approximately 80 MeV in Fig. 4.4 indicates the presence of pickup-decay reactions. For spectra gated on energy losses below 30 MeV, the energy loss was equated with the initial excitation energy in the calculations.

CASCADE will calculate the initial distribution of angular momentum for a given energy; however, this calculation is only applicable for fusion-evaporation reactions. In inelastic-scattering experiments, the excited nucleus populates low angular mo-

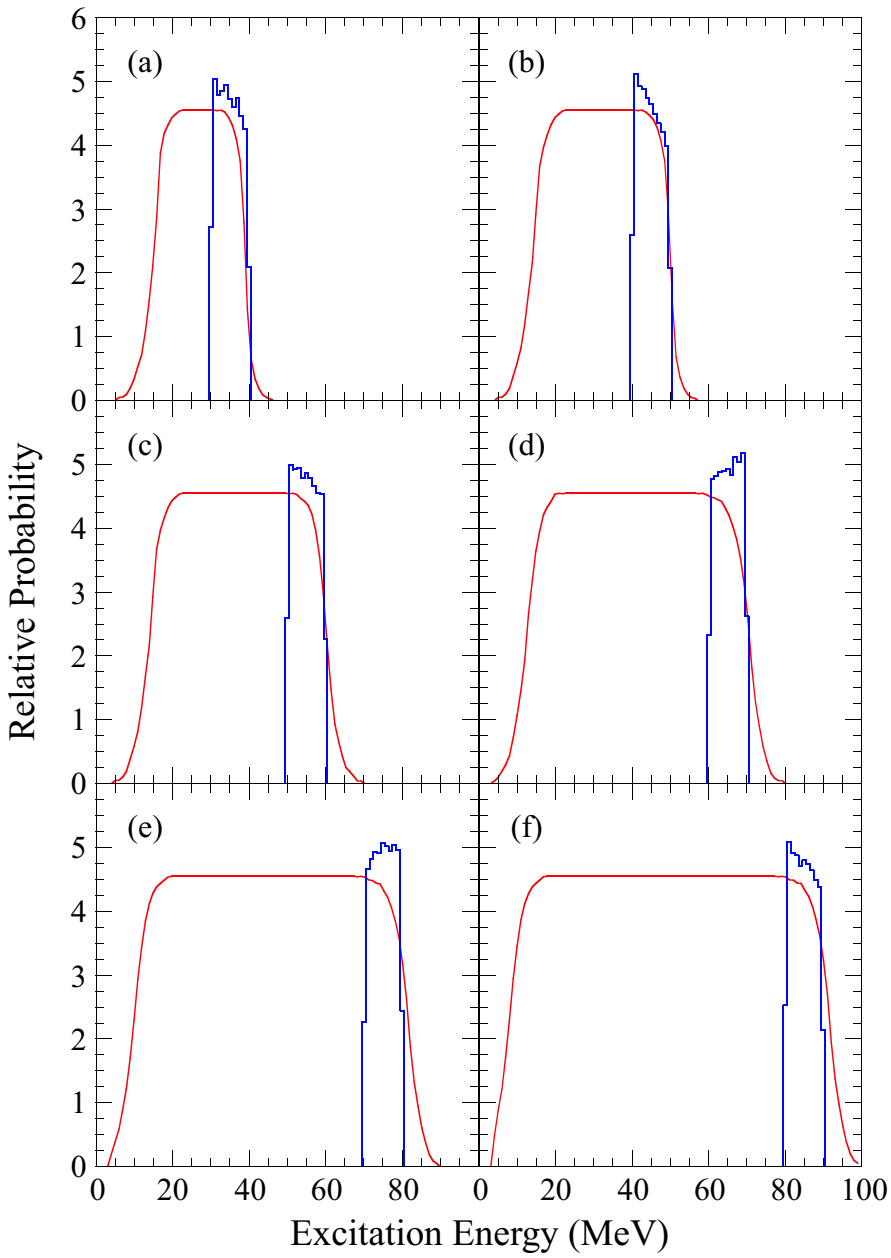

Figure 4.3: Distributions of E* used in this work for energy losses greater than 30 MeV. In all panels, the red curve shows the distributions used in the calculations, while the blue curve shows the distribution of energy losses considered, as determined from the S800 singles data. Panel (a) corresponds to 30–40 MeV, (b) 40–50 MeV, (c) 50–60 MeV, (d) 60–70 MeV, (e) 70–80 MeV, and (f) 80–90 MeV energy losses.

mentum states. CASCADE has the option of reading in a two-dimensional matrix, which specifies the initial angular momentum and energy. To take advantage of this option, the initial distribution of angular momentum must be determined.

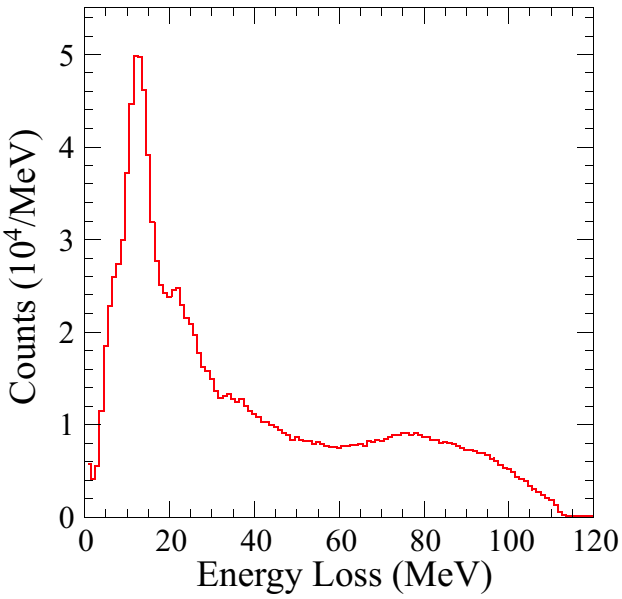

Figure 4.4: The energy loss determined from the S800 singles data is shown. This type of spectrum has been used in past experiments [25–27] to determine the initial excitation energy of the target nucleus.

A range of angular momenta was calculated for a given excitation energy. The upper limit (J_{max}) was determined using the sum of the matter half density radii (b_{max}) of the target and projectile nuclei. The lower limit (J_{min}) was calculated using the nuclear interaction radius (b_{min}). This quantity is defined as:

$$b_{min} = C_T + C_P + 4.49 - \frac{C_T + C_P}{6.35}, \tag{4.1}$$

where C_T and C_P are the matter half density radii of the target and projectile nuclei, respectively [4]. The matter half density radius is 5.43 fm for ^{120}Sn and 2.83 fm for ^{17}O. With these quantities determined, it was straightforward to calculate a lower and upper bound for the angular momentum transferred to the target. The range of angular momentum (J) of the target after the scattering process is given by:

$$J_{min/max} = \frac{1}{197} b_{min/max} p\hbar, \tag{4.2}$$

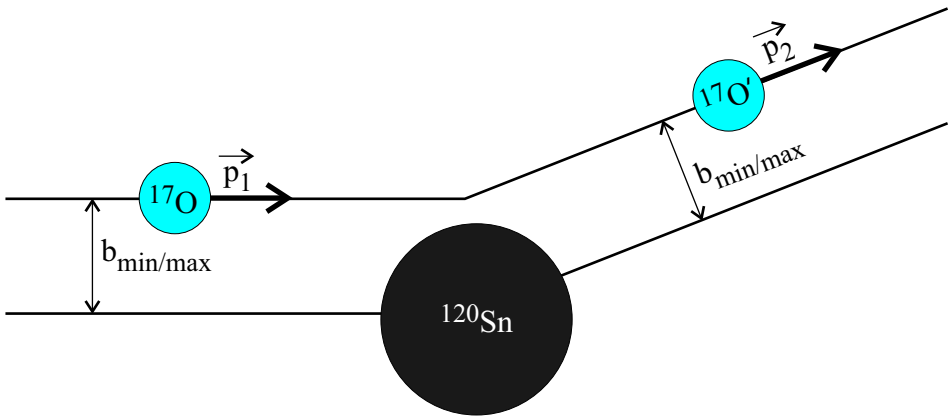

Figure 4.5: Cartoon of inelastic-scattering process to illustrate the momentum transferred to the target from the projectile. All quantities are explained in the text. This figure was adapted from Ref. [4].

where p is the momentum transferred to the target. The value of p is determined by:

$$p = |\vec{p_1}| - |\vec{p_2}|, \tag{4.3}$$

where $\vec{p_1}$ and $\vec{p_2}$ are the momentum of the projectile before and after scattering, respectively. A cartoon of the process is shown in Fig. 4.5.

The two-dimensional matrix used for the energy losses of 20–30 MeV is shown in Fig. 4.6. It is evident from this figure that as the energy loss increases, so does the angular momentum transferred to the target in the scattering process.

4.1.2 Decay Rates

CASCADE calculates the decay rates from the absorption cross sections for the inverse (excitation) process, using the reciprocity theorem [46]. In this model, the excited nucleus may decay by emission of a proton, neutron, alpha particle, or γ ray.

The width per unit energy, $\mathrm{d}\Gamma^x(\mathrm{e}_x)/\mathrm{de}_x$, for emitting a particle x from an excited nucleus 1 (excitation energy E_1, angular momentum J_1, parity π_1) to form a daughter

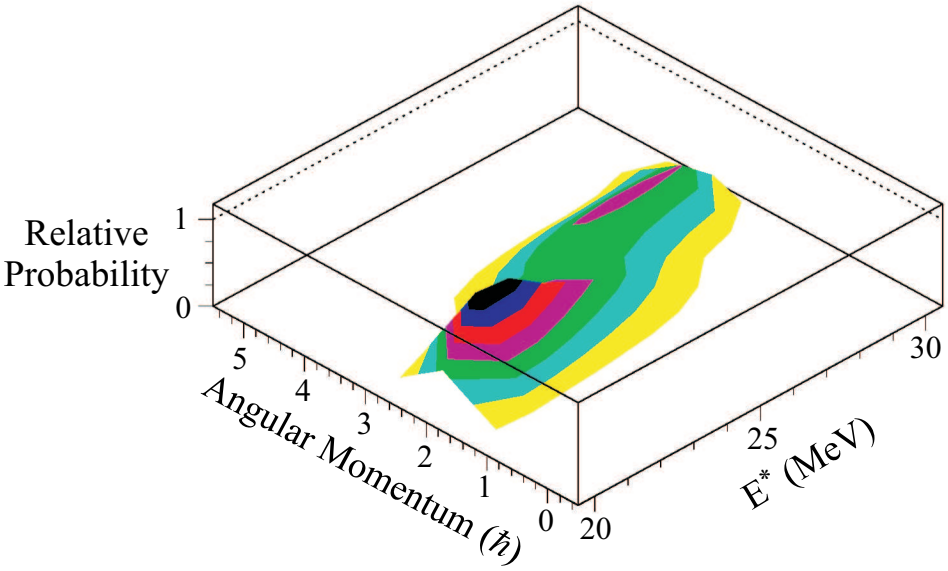

Figure 4.6: Population of the target nucleus in terms of energy and angular momentum for the energy losses of 20–30 MeV. The relative population for each energy was determined by the S800 singles data shown in Fig. 4.4.

nucleus 2 (at E_2, J_2, π_2) is then given by [3]:

$$\frac{\mathrm{d}\Gamma(e_x)}{\mathrm{d}e_x} = \frac{\rho_2(E_2, J_2, \pi_2)}{2\pi\rho_1(E_1, J_1, \pi_1)} \sum_{S=|J_2-S_x|}^{J_2+S_x} \sum_{L=|J_1-S|}^{J_1+S} T_L^x(e_x). \tag{4.4}$$

The kinetic energy of particle x is $e_x = E_1 - E_2 - B_x$, where B_x is the binding energy. Other quantities in Eqn. 4.4 are the level density (ρ), orbital angular momentum (L), channel spin ($S = J_2 + S_x$), and transmission coefficients ($T_L^x(e_x)$). The transmission coefficients are for the scattering of particle x on nucleus 2, and the values for these coefficients are obtained from the optical model.

The width per unit energy, $\mathrm{d}\Gamma^\gamma/\mathrm{d}E_\gamma$, for E1 γ decay is obtained in a similar way, and is given by [3]:

$$\frac{\mathrm{d}\Gamma^\gamma(E_\gamma)}{\mathrm{d}E_\gamma} = \frac{\rho_1(E_2, J_2, \pi_2)}{\rho_1(E_1, J_1, \pi_1)} \frac{\sigma_{abs}(E_\gamma)}{3} \frac{E_\gamma^2}{(\pi\hbar c)^2}, \tag{4.5}$$

where $E_\gamma = E_1 - E_2$ and $J_2 = J_1$ or $J_1 \pm 1$. The quantity $\sigma_{abs}(E_\gamma)$ represents the cross

section for E1 photoexcitation of a single level, averaged over all levels populated by γ decay in a given nuclear reaction, and is defined by:

$$\sigma_{abs} = \frac{4\pi e^2 \hbar}{Mc} \frac{NZ}{A} \sum_{j=1}^{2} \frac{S_j \Gamma_j E_\gamma^2}{\left(E_\gamma^2 - E_j^2\right)^2 + E_\gamma^2 \Gamma_j^2}. \tag{4.6}$$

The quantities S_j, E_j, and Γ_j are the values for the strength (in units of the classical dipole sum rule), energy and width of the E1 resonance, respectively.

The probability of a nucleus decaying through the available channels (n,p,α,γ) is dependent on the values calculated for the width per unit energy. Specifically, the relative magnitude of these calculations for the individual channels determines the percentage of the initial cross section that goes to the various decays. Since this is the case, it is very important that the quantities used to calculate the width per unit energy are accurate. Most of the quantities are well known, or can be calculated.

4.1.3 Level Density

It is very important to describe the level density as accurately as possible. The expression used to calculate the level density in CASCADE is given by [3, 44]:

$$\rho = \frac{a^{1/2}(2J+1)}{12\theta^{3/2}(U+T)^2} e^{2\sqrt{aU}}, \tag{4.7}$$

where,

$$U = E - \Delta - \frac{J(J+1)}{\theta'} = aT^2 - T, \tag{4.8}$$

$$\Delta = \frac{p}{A^{1/2}} \tag{4.9}$$

$$\theta = 2I_{rigid}\hbar^2, \tag{4.10}$$

$$\theta' = \theta(1 + \delta J^2 + \delta' J^4). \tag{4.11}$$

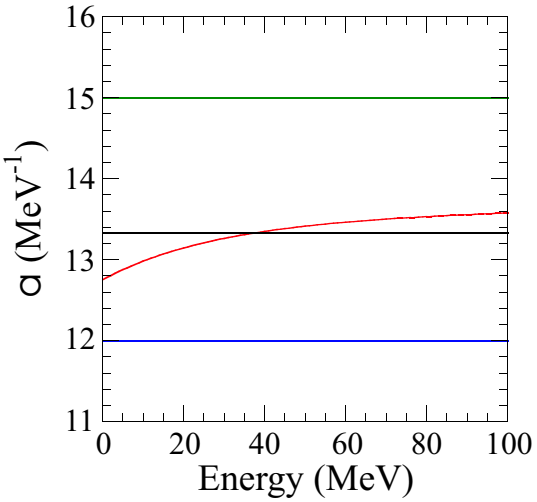

Figure 4.7: Level density parameter comparison for ^{120}Sn. The curves correspond to the following formalisms: green–A/8, black–A/9, blue–A/10, and red–Reisdorf.

In the above equations, E is the energy, Δ is the pairing energy, and T is the nuclear temperature. In the expression for Δ, a new parameter is introduced, namely the constant p, which is 8.5 MeV. The quantity θ is determined by the rigid body moment of inertia, while θ' represents the moment of inertia of a deformable rotating liquid drop [3]. The only other quantity not defined in Eqn. 4.7 is the level density parameter, a.

Several approaches have been used to calculate a. In past experiments, this quantity has been fixed over all energies and angular momenta considered. It was not uncommon to fix the value based on the mass (A) of the nucleus. The typical range used for Sn corresponds to A/10–A/8. In more recent experiments, the formalism set forth by Reisdorf [47] has been adopted. A comparison of the different formalisms for the level density parameter is shown in Fig. 4.7. In the Reisdorf description, a is both energy and mass dependent. Additionally, this description takes shell effects into account. In the description set forth by Reisdorf, a is calculated in the following way:

$$\bar{a} = 0.04543 r_0^3 A + 0.1355 r_0^2 A^{2/3} + 0.1426 r_0 A^{1/3} \tag{4.12}$$

$$a = \bar{a}\left(1 + \frac{\delta S}{U}\left(1 - e^{-U/E_D}\right)\right). \tag{4.13}$$

The quantities r_0 and E_D are constants given by 1.16 fm and 18.5 MeV, respectively, and δS is determined by the magnitude of shell effects. The Reisdorf description for the level density was adopted in the statistical calculations used in this analysis. The use of this level density description is even more important for nuclei where shell effects are large.

4.1.4 GDR Width

The width of the GDR is typically held constant throughout the decay process in CASCADE, and corresponds to an average along the entire decay. The code was modified to include the option of a non-constant width. In a recent paper by Kusnezov *et al.* [35], a parameterization was presented for the width of the GDR as a function of temperature (T), angular momentum (J), and the mass (A) of the nucleus. The parameterization is given by:

$$\Gamma(T, J, A) = \Gamma(T, J = 0, A)\left[L\left(\xi\right)\right]^{4/(T+3)} \tag{4.14}$$

$$\Gamma(T, J = 0, A) = \Gamma_0(A) + c(A)\ln(1 + T), \tag{4.15}$$

where $\Gamma_0(A)$ is the ground state width of the GDR, $c(A) \approx 6.45 - A/100$, $\xi = J/A^{5/6}$, and $L(\xi) - 1 \approx 1.8[1 + e^{(1.3-\xi)/0.2}]^{-1}$, as defined in Ref. [35]. This parameterization was incorporated into CASCADE, and allowed for the width of the GDR to be adjusted continuously along the decay.

In addition to the parameterization of Ref. [35], a second temperature-dependent width was incorporated into CASCADE for Sn, as shown by the blue curve in Fig. 4.8. This curve is an empirical fit to the existing data for Sn. The dependence of the width on angular momentum was not considered. The excited nucleus in this work never

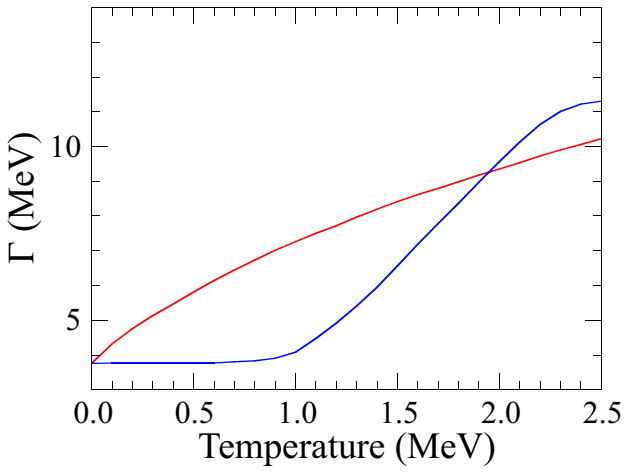

Figure 4.8: GDR width descriptions incorporated into CASCADE. The red curve was calculated from Eqn. 4.14 at low angular momentum, and the blue curve was empirically determined from existing data. Both of these curves were incorporated into CASCADE.

populates angular momentum states higher than $20\hbar$, and angular momentum effects are insignificant below $20\hbar$ in Sn [33,35]. The width description by Kusnezov *et al.* is also shown as the red curve in Fig. 4.8 for comparison.

4.2 Bremsstrahlung Radiation

In addition to the statistical γ rays, there was also a non-statistical contribution to the γ-ray spectra. Bremsstrahlung radiation was present in this data, as can be seen at high γ-ray energies (see Fig. 3.19). The form of the bremsstrahlung component of the spectra was assumed to have the form $\exp(-E_\gamma/E_0)$, where E_0 was set to a value of 25 MeV [48, 49]. This value is smaller than that given in Ref. [48], because the collision is peripheral [49] in this experiment.

The study of bremsstrahlung radiation is interesting in itself. Numerous experiments have been performed to study bremsstrahlung radiation [48, 49]. The γ-ray spectra from this work contain bremsstrahlung information; however, statistics are too poor to perform a detailed analysis.

4.3 GEANT Simulation

The response of the BaF_2 arrays was simulated with the Monte Carlo code GEANT [50]. This code allows the user to specify the exact geometry of the experimental setup. The S800 target chamber, target chamber doors, BaF_2 arrays, and aluminum used to hold the BaF_2 arrays together were specified. GEANT also allows for the materials used in the experiment to be defined. This is especially important since BaF_2 is not one of the standard materials in the code.

In the simulation it is important to take the energy resolution of the BaF_2 arrays into account. It was not possible to determine the resolution of the arrays as a function of energy in this experiment. The only data that was available to determine the resolution was the source data. The highest energy point was only 4.4 MeV. Information was needed for energies much higher than this. To account for this, the energy resolution determined in the work of Ref. [51] was adapted. The detectors used in Ref. [51] were the same detectors used in this experiment. For this experiment, all scintillators were recoupled to their photomultiplier tubes. The recoupling resulted an energy resolution that was slightly better than that of Ref. [51], so the spread (σ) measured by Ref. [51] at a given energy was scaled by 90%. The resolution used in the simulation is shown in Fig. 4.9.

It was possible to use the same analysis routines from the data analysis in the simulation. Since GEANT is a Monte Carlo code, events can be tracked individually. For a given event in the simulation, all detectors were considered. Any detectors that had energy signals were flagged for event reconstruction (see Sec. 3.3.2). Once the energy reconstruction was complete, the energies were histogrammed.

The accuracy of the simulation was tested by comparing experimental source data to simulated source data. This was done for both the ^{88}Y and PuBe sources, and is shown in Fig. 4.10. The good agreement between data and simulation indicates that GEANT can be used to generate a realistic response function for the detector arrays.

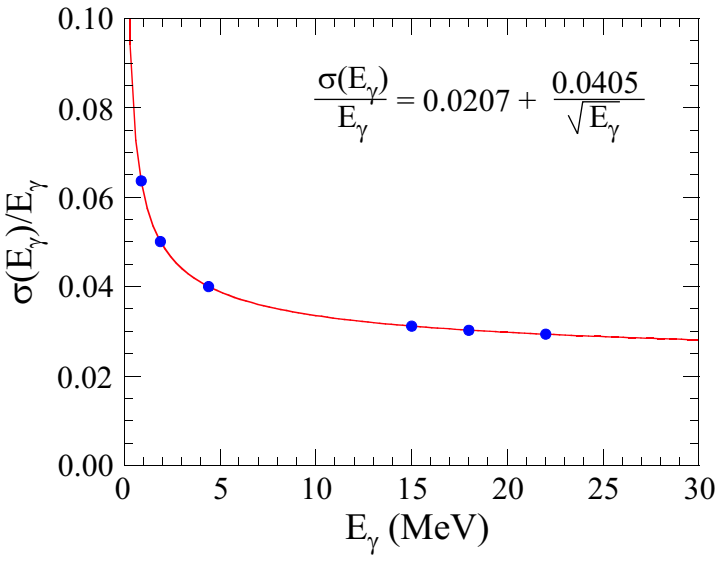

Figure 4.9: Energy resolution of the BaF_2 arrays. This plot is adapted from Ref. [51]. The solid points show where measurements for the resolution of the array were made by Ref. [51]. The solid curve is the scaled resolution used in this analysis, as discussed in the text.

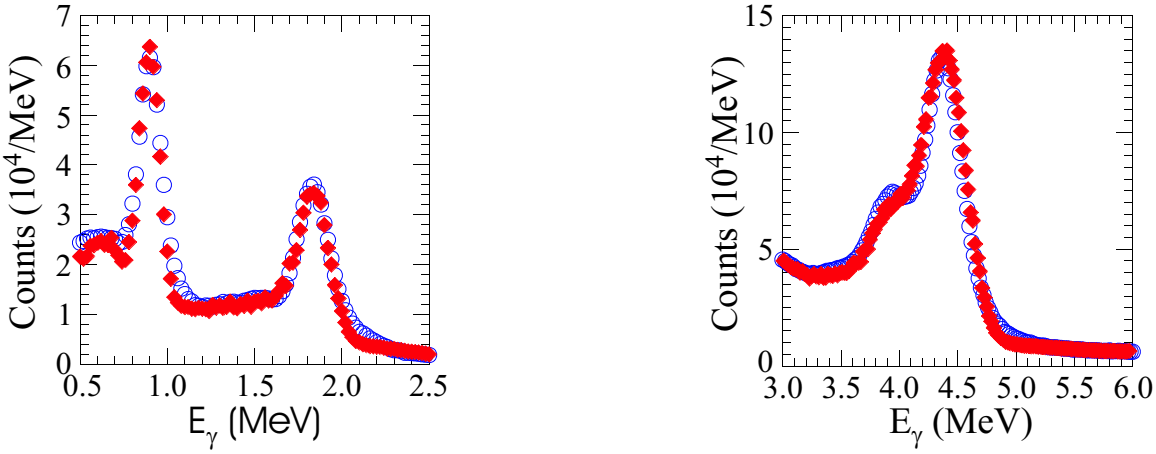

Figure 4.10: Comparisons of source data and simulation. Left – ^{88}Y. Right – PuBe. In each panel, the solid red diamonds are the result of the simulation, and the open blue circles are the data.

To generate a response function for the arrays, it was necessary to emit a γ-ray with a given energy and plot the resulting detected energy in the BaF_2 arrays. In this experiment we dealt with energies up to approximately 32 MeV. The response of the arrays was determined in 100 keV steps up to this energy. This was accomplished by emitting random energy γ rays in random directions. A 2-D histogram was created

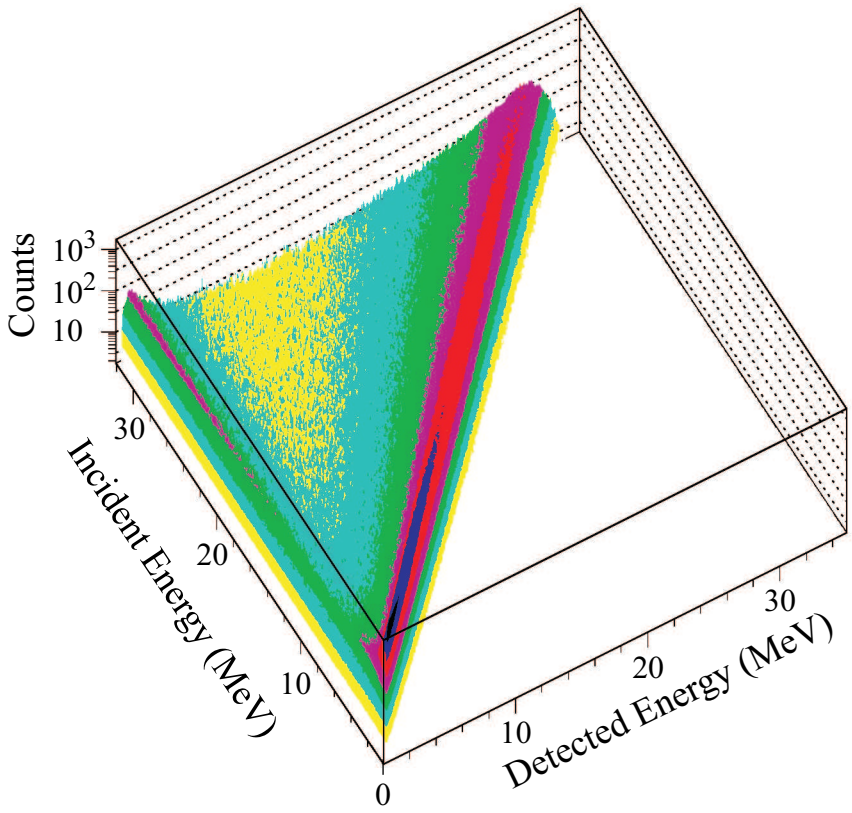

Figure 4.11: Response of the BaF_2 array as simulated by GEANT.

with the incident γ-ray energy on one axis, and the detected γ-ray energy on the other axis. This histogram is displayed as a surface plot in Fig. 4.11. Since all energies were random, it was necessary to keep track of the number of γ rays emitted in each 100 keV interval. This was easily accomplished by histogramming the incident energy event by event. The resulting distribution of incident γ rays is shown in Fig. 4.12.

Making cuts on the histogram shown in Fig. 4.11 allowed for the response of the BaF_2 arrays to a given energy to be examined. Several cuts are shown in Fig. 4.13. These cuts show the overall behavior of the array to a given energy. These plots do not take the geometric efficiency into account. The response of the array to a given energy was obtained by making a cut on Fig. 4.11, and scaling by the number of incident γ rays at the given energy. The number of incident γ rays is shown in Fig. 4.12.

The response function of the arrays allowed for the CASCADE calculations to be folded. When comparing data and theory, it is necessary to either unfold the data,

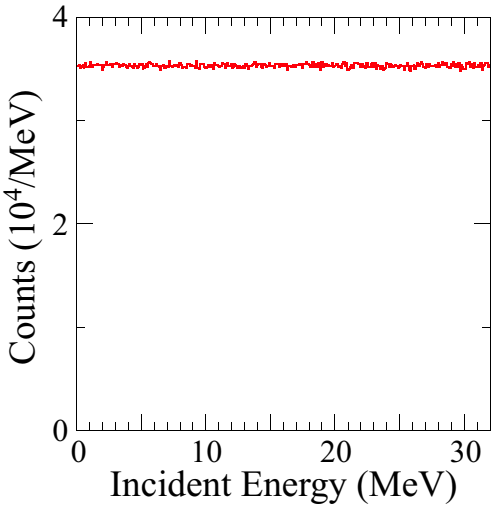

Figure 4.12: Distribution of γ rays emitted in the GEANT simulation.

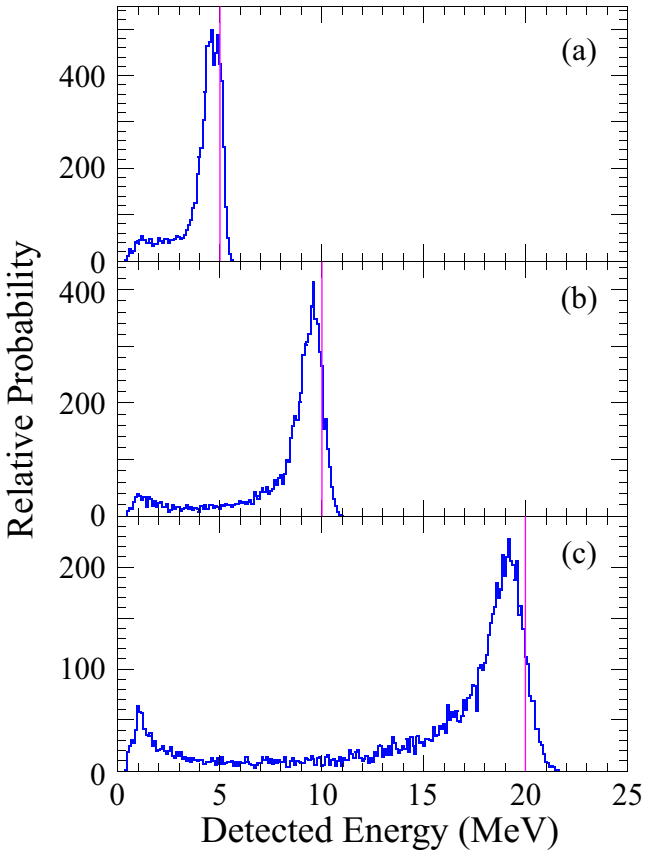

Figure 4.13: The response of the BaF_2 array is shown for several energies. Panels (a), (b), and (c) correspond to incident γ-ray energies of 5, 10, and 20 MeV, respectively. The incident γ-ray energy is indicated by the vertical line in each panel.

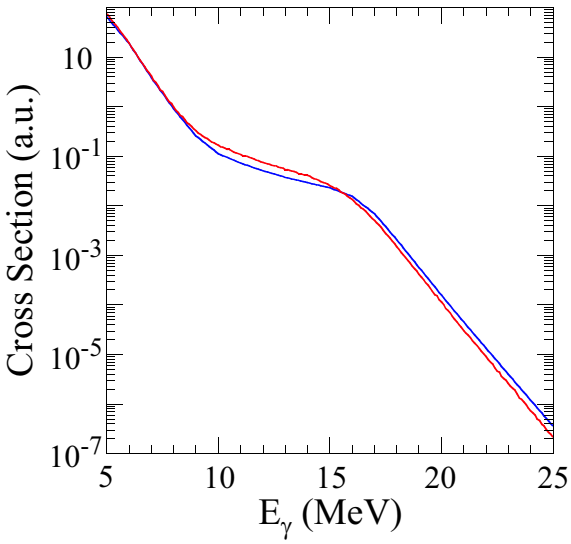

Figure 4.14: Example to demonstrate the effects of folding. Blue curve – Raw CASCADE calculation. Red curve – Folded CASCADE calculation. The red curve was normalized to the blue curve at 6 MeV.

or fold the calculations. Since it is very difficult to unfold the data, the calculations were folded. An example of the effects of folding are shown in Fig. 4.14.

4.4 Nuclear Temperature

4.4.1 Formalism to Calculate the Temperature

The conversion of excitation energy to temperature is necessary if comparisons are to be made between theoretical predictions and experimental results. The nuclear temperature (T) is defined as:

$$T = \left(\frac{d}{dU} \left[ln\left(\rho\right) \right] \right)^{-1}, \tag{4.16}$$

where ρ is the level density and U is the energy. At high energies, the Fermi gas model of the nucleus is valid, and the level density has the following form [52]:

$$\rho \propto exp(2\sqrt{aU}). \tag{4.17}$$

This form of the level density, along with Eqn. 4.16, leads to an expression for the nuclear temperature given by:

$$T = \sqrt{\frac{U}{a}}. \tag{4.18}$$

The expression given in Eqn. 4.18 has traditionally been used to determine the temperature in GDR experiments [3,16,20,25,27]. It should be noted that the level density parameter was constant in the derivation of Eqn. 4.18.

The Sn and Pb data existing prior to 1998 have been re-evaluated [35]. In the work of Ref. [35], the Reisdorf [47] level density formalism was used. Using this formalism, and the level density in CASCADE (Eqn. 4.7), the temperature was re-calculated using Eqn. 4.16. The expression obtained by Ref. [35] was:

$$T = \left(-\frac{2}{U} + \frac{da}{dU}\frac{1}{2a} + \sqrt{\frac{a}{U}} + \frac{da}{dU}\sqrt{\frac{U}{a}} \right)^{-1}, \tag{4.19}$$

where

$$\frac{da}{dU} = \frac{\bar{a}\ \delta S}{U^2}\left[-1.0 + \left(1.0 + \frac{U}{E_D} \right) e^{-U/E_D} \right]. \tag{4.20}$$

In this derivation, the quantity $(U+T)$ in Eqn. 4.7 was replaced by U. This is justified as T is small compared to U. The expression in Eqn. 4.19 was used to calculate the temperature in this work.

The calculation of temperature is dependent on the level density description used. Since different level density descriptions are used in analyzing data, it is important to determine the temperature in a manner consistent with the data that comparisons are to be made with. The effect of using different level density descriptions is evident in Fig. 4.15.

Some care has to be taken when calculating the temperature using Eqn. 4.19. The determination of the level density (Eqn. 4.7) is not accurate for very low energies. This is evident in Fig. 4.15. A vertical asymptote is present at $\sim$ 0.32 MeV for the

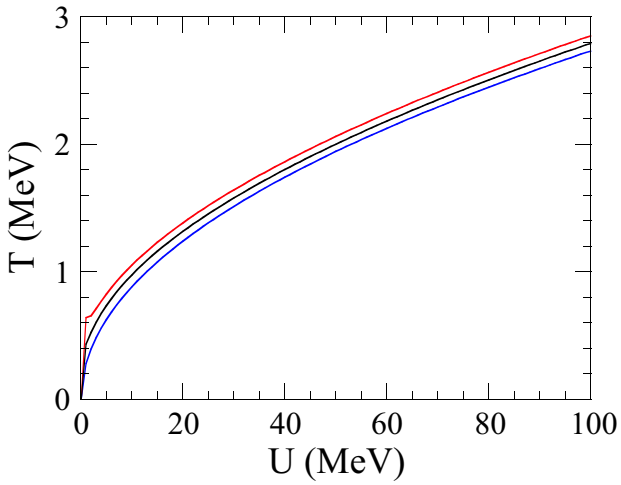

Figure 4.15: Temperature comparison for various level density descriptions. The blue curve shows the result of Eqn. 4.18, while the red curve shows the result of Eqn. 4.19. The black curve was determined with the Bethe [52, 53] level density description.

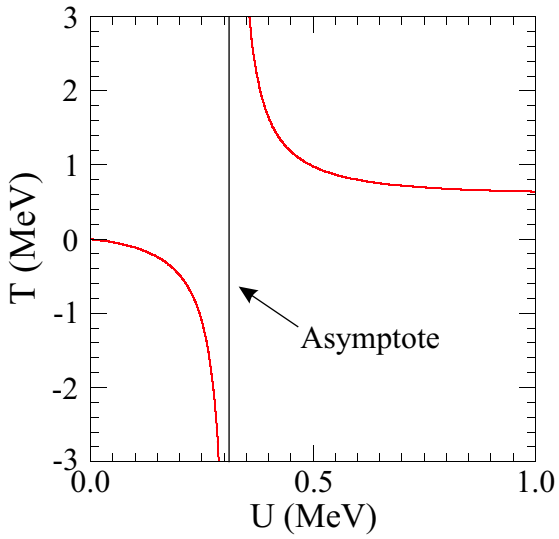

Figure 4.16: Low energy region of exact temperature calculation (red curve from Fig. 4.15). The vertical asymptote at U $\sim$ 0.32 MeV is apparent, and shows the danger in using this approach to calculate the temperature at low energies.

red curve shown in Fig. 4.15. This is clearer in Fig. 4.16.

At energies below $\sim$ 2–3 MeV, the temperature should not be calculated with Eqn. 4.19. The level density, as calculated in CASCADE, is not accurate at very low energies. This has been accounted for in the calculations, as discrete levels were included in the CASCADE calculations. For the experiment discussed here, the lowest

energy that had to be converted to a temperature was approximately 9 MeV, and the problems associated with Eqn. 4.19 are unimportant.

4.4.2 Relevant Quantities

To calculate the nuclear temperature using Eqn. 4.19, two quantities must be determined. One of these quantities is the mean excitation energy of the nucleus during the decay. Since the Reisdorf level density formalism is used in this analysis, the magnitude of shell effects also must be determined.

Mean Excitation Energy

The mean excitation energy ($\overline{E^*_{eff}}$) of the nucleus along the decay of the GDR is needed in order to calculate the temperature. The quantity $\overline{E^*_{eff}}$ is determined by:

$$\overline{E^*_{eff}} = \overline{E_{avg}} - E^{rot}_{avg} - E_{GDR}, \tag{4.21}$$

where $\overline{E_{avg}}$ is the average energy, E^{rot}_{avg} is the average rotational energy, and E_{GDR} is the ground state energy of the GDR. It is necessary to subtract E^{rot}_{avg} and E_{GDR} from $\overline{E_{avg}}$ because the energy associated with GDR corresponds to the energy associated with the states upon which the GDR is built [3]. The rotational energy is calculated with the following expression:

$$E^{rot}_{avg} = \frac{\overline{J_{avg}}\left(\overline{J_{avg}}+1\right)}{\theta'}, \tag{4.22}$$

where $\overline{J_{avg}}$ is the average angular momentum of the nucleus during the decay.

The determination of the quantities $\overline{E_{avg}}$ and $\overline{J_{avg}}$ is relatively straightforward from the computer code CASCADE. As discussed earlier, CASCADE calculates an expected spectrum of γ rays, which is dependent on the specified initial population of the nucleus. From this initial population, the code determines the relative popula-

E ↓ J →	1/2	5/2	9/2	13/2	17/2	21/2	25/2	29/2
50.4	0	1	113	1145	1104	98	1	0
49.4	0	12	576	3941	3473	406	12	0
48.4	0	48	1374	7063	5852	870	36	0
47.4	0	116	2318	9878	7720	1358	69	0
46.4	1	213	3299	12283	9018	1789	116	1
45.4	2	334	4280	14294	9808	2120	167	3
44.4	3	469	5293	15766	10107	2313	207	4
43.4	6	623	6342	16953	10014	2362	229	6
42.4	9	799	7413	17865	9617	2294	235	8
41.4	14	992	8516	18465	9160	2145	227	10
40.4	20	1185	8693	16887	8366	1965	208	10
39.4	28	1269	7287	12903	6985	1748	181	10
38.4	35	1166	5423	8997	5302	1481	153	9
37.4	39	964	3773	5971	3773	1187	128	8
36.4	37	732	2506	3829	2555	888	105	7
35.4	32	510	1591	2371	1644	619	85	6
34.4	25	333	973	1425	1013	408	66	4
33.4	18	210	581	840	608	261	49	4
32.4	13	129	342	489	359	162	35	3
31.4	8	78	199	283	210	99	24	2
30.4	5	46	116	163	122	60	16	2
29.4	3	27	67	94	70	35	10	1
28.4	2	16	38	54	40	21	6	1
27.4	1	9	22	31	23	12	4	1
26.4	1	5	13	18	13	7	2	0
25.4	0	3	7	11	8	4	1	0
24.4	0	2	4	6	4	2	1	0
23.4	0	1	2	3	2	1	0	0
22.4	0	1	1	2	1	1	0	0
21.4	0	0	1	1	1	0	0	0

Table 4.2: Sample population matrix from CASCADE. The relative probability of population in terms of energy and angular momentum is shown. The energy, in units of MeV, is indicated in the left most column, while the angular momentum, in units of $\hbar$, is indicated in the top row.

tion of daughter nuclei along the decay. By examining these populations, an average energy and angular momentum can be determined for each nucleus along the decay. Table 4.2 shows a typical population output from the code. For this particular example, E_{avg}=42.39 MeV and J_{avg}=6.87 $\hbar$.

The average energy and angular momentum of each daughter nucleus along the

Nucleus	E_{avg} (MeV)	J_{avg} ($\hbar$)	δS (MeV)	σ	Relative Weight (%)
^{120}Sn	54.89	6.71	-1.311	0.98	39.46
^{119}Sn	42.39	6.87	-0.483	0.04	30.70
^{119}In	35.47	6.87	0.211	1.96	0.24
^{118}Sn	32.92	6.98	-0.938	1.04	22.66
^{118}In	24.72	6.94	0.605	1.02	0.17
^{117}Sn	21.16	7.02	-0.361	2.04	5.85
^{117}In	16.26	6.94	0.590	2.02	0.04
^{116}Sn	12.48	6.97	-0.833	3.04	0.54
^{116}Cd	34.98	7.22	0.575	3.02	0.22
^{115}Cd	23.98	7.22	1.199	4.02	0.10
^{114}Cd	16.04	7.15	0.624	5.02	0.02

Table 4.3: Summary of nuclei populated along the decay. Several quantities relevant in calculating the temperature are shown. The quantities are described in the text.

decay allows for the determination of $\overline{E^*_{eff}}$. To calculate this quantity, the average energy of each daughter nucleus has to be determined. Calculating E_{avg} for each daughter nucleus is straight forward, as discussed in the previous paragraph. The weight given to each daughter nucleus in calculating $\overline{E_{avg}}$ is determined by the γ-ray cross section at 15 MeV of that nucleus relative to the total cross section of γ rays at 15 MeV, as determined by CASCADE. Determining $\overline{J_{avg}}$ is completely analogous to calculating $\overline{E_{avg}}$. The γ-ray energy of 15 MeV was chosen because the ground state energy in ^{120}Sn is 15.4 MeV [54]. Since CASCADE calculates everything in 1 MeV steps, 15.4 MeV was rounded down to 15 MeV. Table 4.3 shows an example of what can be expected. In this example, $\overline{E_{avg}}$=43.68 MeV and $\overline{J_{avg}}$=6.84 $\hbar$. With these quantities determined, it is easy to calculate $\overline{E^*_{eff}}$. It is this value of energy that should be used to calculate the temperature of the nucleus during the decay.

Magnitude of Shell Effects

The magnitude of shell effects (δS in Eqn. 4.20) is determined by the nucleus which has the number of protons and neutrons closest to that of $\overline{N}$ and $\overline{Z}$. The quantities $\overline{N}$ and $\overline{Z}$ are determined by performing a weighted average of Z and N. The averaging

procedure is completely analogous to that in the previous section where $\overline{E_{avg}}$ and $\overline{J_{avg}}$ were determined. The nucleus is then found by defining the quantity σ, where

$$\sigma = |\overline{Z} - Z| + |\overline{N} - N|. \tag{4.23}$$

The quantity σ can be calculated for each nucleus populated during the decay, as shown in Table 4.3. The nucleus which has the smallest value of σ determines δS. For the example in the previous section, $\overline{N} = 69.03$ and $\overline{Z} = 49.99$, which means δS is determined by ^{119}Sn.

Chapter 5

Interpretation of the γ-ray Spectra

The interpretation of the γ-ray spectra relied on the tools developed in the previous chapter. The parameters of the GDR are the sum rule strength (S), energy (E_{GDR}), and width (Γ). These parameters were extracted from the data by comparing theoretical calculations with data. The theoretical calculations consist of two pieces. The first piece is a statistical model calculation performed with CASCADE. The second piece is a bremsstrahlung calculation. Both of these calculations were folded, normalized to the data, and added together. This spectrum was then compared to data.

In the case of the γ-ray spectrum gated on energy losses of 20–30 MeV, the data was fit by varying the GDR parameters in CASCADE to achieve the best agreement between calculation and data using χ^2 minimization. The higher energy loss data was not analyzed in the same manner. Rather, this data was used to check for consistency between this data and previous measurements.

5.1 20–30 MeV Energy Loss Spectrum

The 20–30 MeV energy loss spectrum is low enough in energy to equate the initial excitation energy with the energy loss of the scattered ^{17}O. This was discussed in Sec. 4.1.1, and will not be discussed further here. The initial angular momentum was

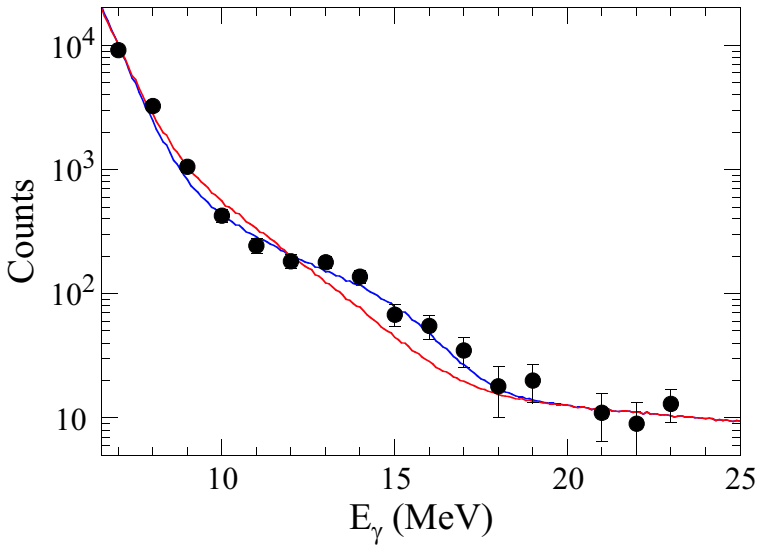

Figure 5.1: The γ-ray spectrum is shown as the solid points for 20–30 MeV energy losses. The blue curve is the result of the χ^2 fit, while the red curve is the result of using the description for the width set forth by Kusnezov *et al.* [35].

also determined as discussed in Sec. 4.1.1. With the initial excitation energy and angular momentum specified, CASCADE calculations were performed.

In the calculations, the parameters of the GDR were varied to minimize χ^2. The result of the calculations are shown in Fig. 5.1 as the solid blue curve. The parameters were found to be S = 1.1 $\pm$ 0.2, E_{GDR} = 16.5 $\pm$ 0.7 MeV, and Γ = 4 $\pm$ 1 MeV. For this case, the mean excitation energy following the GDR decay was found to be 9.7 MeV. This mean excitation energy was converted to a temperature as discussed in Sec. 4.4. The temperature was found to be 1 MeV. The fitted width agrees with the ground state GDR width of 4.9 MeV [54]. The fitted resonance energy, E_{GDR}, is somewhat higher than the ground state value of 15.4 MeV [54]; however, a resonance energy higher than that of the ground state value was also measured at low excitation energies in Refs. [25, 27].

The low-temperature width is shown in Fig. 5.2 with other existing data points taken from Refs. [22,35]. The temperature of all data points in Fig. 5.2 was determined as described in Sec. 4.4. The value of the width at zero temperature was set to the

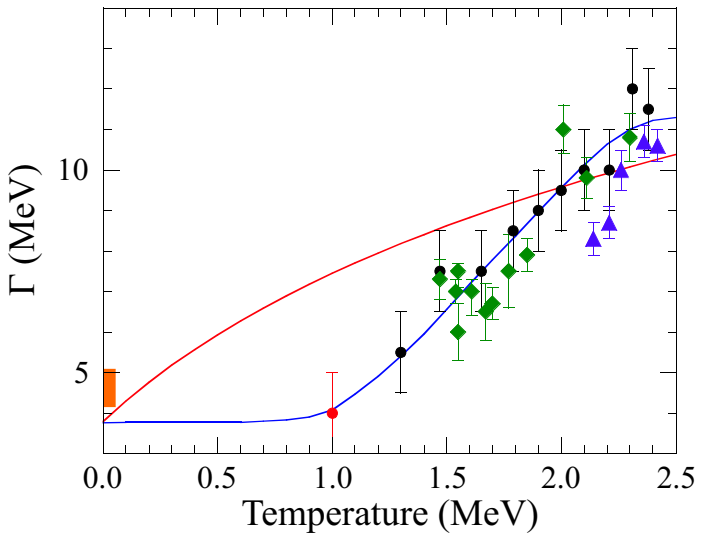

Figure 5.2: Comparison of data and theory for Sn. The red circle is from this work. The blue circles and green diamonds are from Ref. [35], where the circles are from α-scattering and the diamonds are from fusion-evaporation reactions. The blue triangles are from Ref. [22] and are from fusion-evaporation reactions. The orange rectangle is the range of widths measured for the ground state. The red curve is the adiabatic thermal shape fluctuation calculation, and the blue curve is the empirical curve discussed in Sec. 4.1.4.

value of 3.8 MeV [55], as in Ref. [35]. The red curve in Fig. 5.2 shows the adiabatic thermal shape fluctuation width calculated in Ref. [35] at low angular momentum. The red curve is generally consistent with the data at higher temperatures, but fails to describe the data at low temperatures.

The temperature-dependent width shown by the red curve in Fig. 5.2 was incorporated into CASCADE (see Sec. 4.1.4). Using this temperature-dependent width, the expected γ-ray spectrum shape for energy losses of 20–30 MeV was calculated, assuming $E_{GDR} = 16.5$ MeV and $S = 1.1$ as determined in the χ^2 fit. The result, shown as the red curve in Fig. 5.1, does not describe the data well. The width of the calculated spectrum shape is clearly too large, distributing the strength over a larger energy range than the data.

The empirical temperature-dependent width shown by the blue curve in Fig. 5.2 was also incorporated into CASCADE (see Sec. 4.1.4). If the data from this work is

consistent with previous measurements of the GDR width, then the empirical width description in Fig. 5.2 should describe the overall behavior of the data at higher temperatures.

5.2 Higher Energy Loss Data

The higher energy-loss data was used to check for consistency with previous measurements of the GDR width. The γ-ray spectra measured for energy losses higher than 30 MeV were not fit using χ^2 minimization. Additionally, the width was not held constant in the CASCADE calculations. Rather, the expected spectral shapes of the different measured spectra were calculated.

The calculation of the expected spectral shapes involved several steps. The initial excitation energy and angular momentum of the nucleus were determined as discussed in Sec. 4.1.1. The width of the GDR in the calculations was adjusted continuously along the decay as determined by the empirical width in Fig. 5.2. The sum rule strength, S, was fixed at 100%. The resonance energy, E_{GDR}, was fixed at 16.0 MeV. No attempt was made to fit the data. The only free parameter in the calculations was the overall normalization between the calculation and data.

The results of the calculations are shown in Fig. 5.3. While the agreement is not perfect between calculation and data, the overall shape of the calculations is similar to the data. The overall agreement indicates that this data is consistent with previous measurements.

The effects of using a broad range of energies for the initial excitation energy (see Fig. 4.3) in the calculations can also be investigated. This is possible by considering the highest energy loss (80–90 MeV) γ-ray spectrum measured. The highest energy loss spectrum had the broadest range of energies, and as such the effects should be largest for this spectrum. The effects should be evident by performing a second

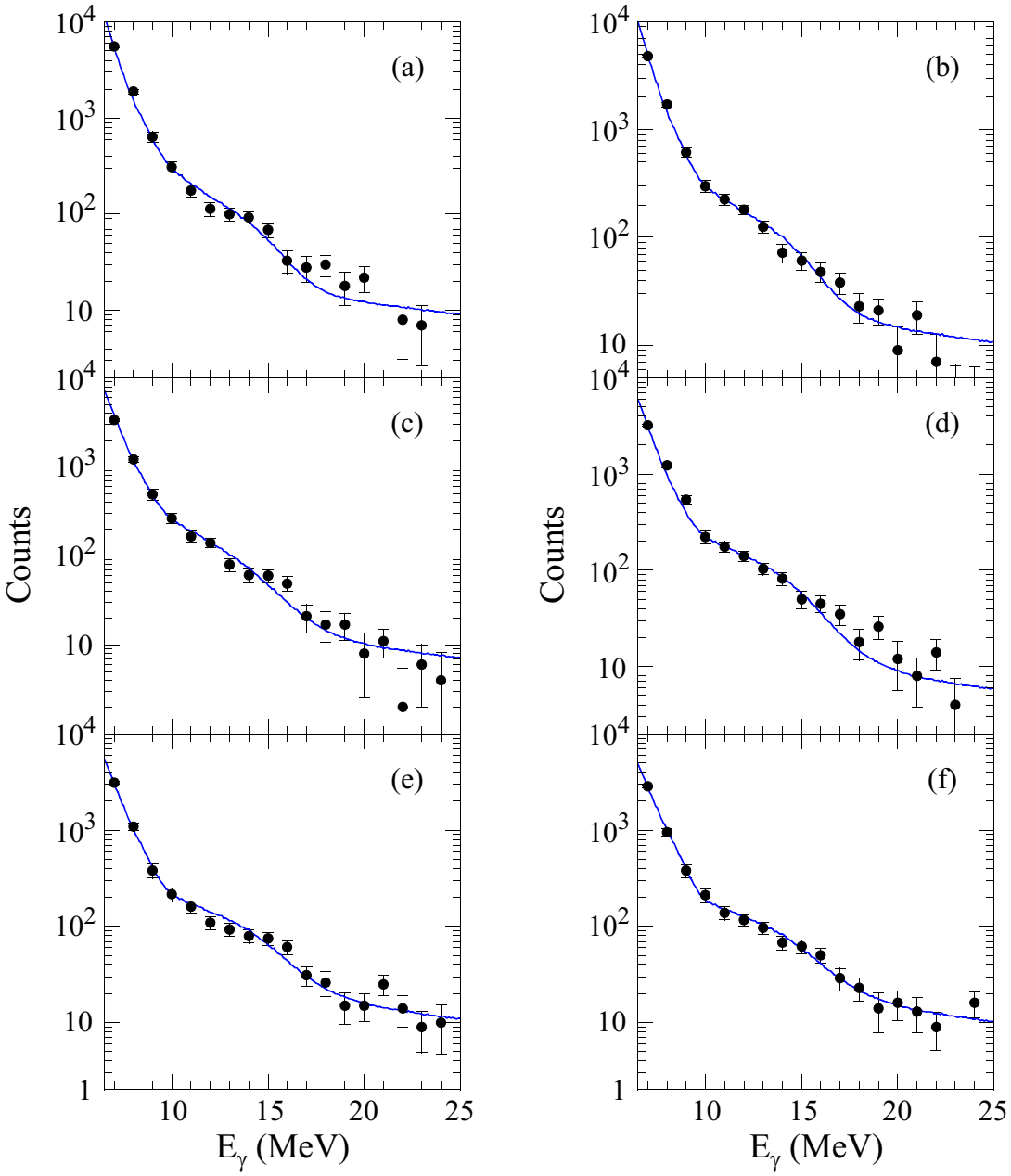

Figure 5.3: Comparisons of data and expected spectral shapes as calculated with CASCADE. The γ-ray spectra are gated on the following range of projectile energy losses: (a) 30–40 MeV, (b) 40–50 MeV, (c) 50–60 MeV, (d) 60–70 MeV, (e) 70–80 MeV, and (f) 80–90 MeV. In all panels the data is shown as the solid points, while the calculations are shown by the solid blue curves. The calculations were performed as described in the text.

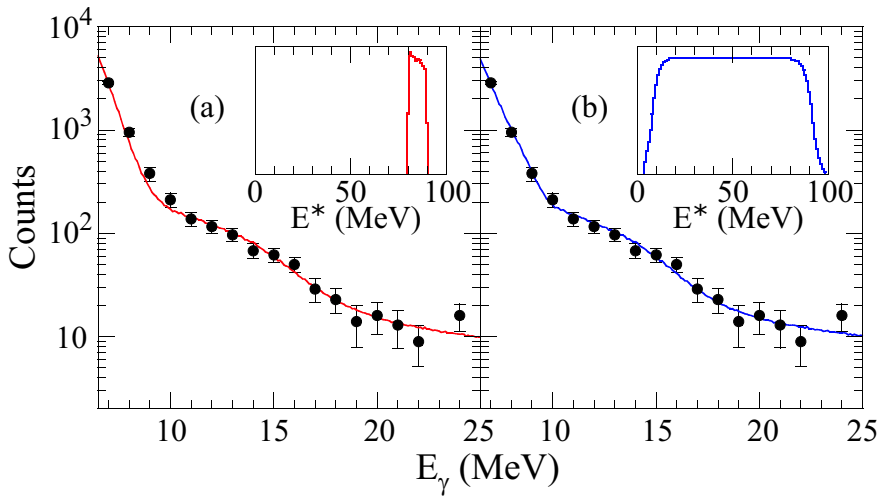

Figure 5.4: The 80–90 MeV energy loss γ-ray spectrum is shown in both panels. In panel (a), the initial excitation energy in the CASCADE calculation was set to the projectile energy loss as shown in the insert. The calculation is shown as the solid red curve. In panel (b), the initial excitation energy in the CASCADE calculation was set according to the insert. The resulting calculated spectrum is shown as the solid blue curve.

calculation, where the initial excitation energy is equated with the projectile energy loss. This calculation can then be compared with the calculation in Fig. 5.3f.

The result of this second calculation is shown in Fig. 5.4a. The other panel in this figure is identical to Fig. 5.3f. In both calculations (Fig. 5.4a,b), the width was adjusted continuously along the decay as shown by the empirical width in Fig. 5.2. Also, the resonance energy was fixed at 16.0 MeV. The only difference between the calculations is the initial excitation energy used (see inserts of Fig. 5.4). In the case where the initial energy was set to the projectile energy loss, it was necessary to reduce the sum rule strength from 100% to 36%. Both calculations show good agreement with data, and hence the choice of the initial excitation energy distributions influence the apparent GDR strength, but has only minor influences on the GDR width. This is consistent with the findings of Ref. [36].

The broad distributions used for the initial excitation energy extend to much lower energies than the energy losses considered. The population of lower excitation energies adds to the statistical γ rays, and does not influence the high-energy γ rays.

The high-energy γ rays are predominantly from the highest energies populated. This results in more statistical γ rays relative to the high-energy γ rays, and affects the overall sum rule strength as noted above.

Chapter 6

Conclusions

The GDR was studied by means of heavy-ion scattering using ^{17}O. This allowed for the first measurement of the GDR width at a temperature as low as 1 MeV in Sn.

In the previous chapter, the γ-ray spectra were analyzed. In the case of the spectrum where the temperature was found to be 1 MeV, the parameters of the GDR were extracted. The parameter of main interest was the width. The width (4 ± 1 MeV) extracted for this temperature was compared with previous measurements (Fig. 5.2). The consistency of this data was then verified by analyzing the higher energy-loss data.

The GDR width found at a temperature of 1 MeV is significantly lower than predicted (see Fig. 5.2 or Fig. 6.2b). The discrepancy at this temperature is on the order of 3 MeV. The difference between theory and experiment is especially striking when comparing the predictions with the empirical curve in Fig. 5.2. This indicates that the calculations overestimate the influence of thermal shape fluctuations at low temperatures.

Further insight into the behavior of the GDR width may be obtained by comparing Sn with other nuclei. Another nucleus where enough data and theoretical calculations exist is Cu. This nucleus has weak shell effects (see Fig. 6.1), just as in Sn. Therefore,

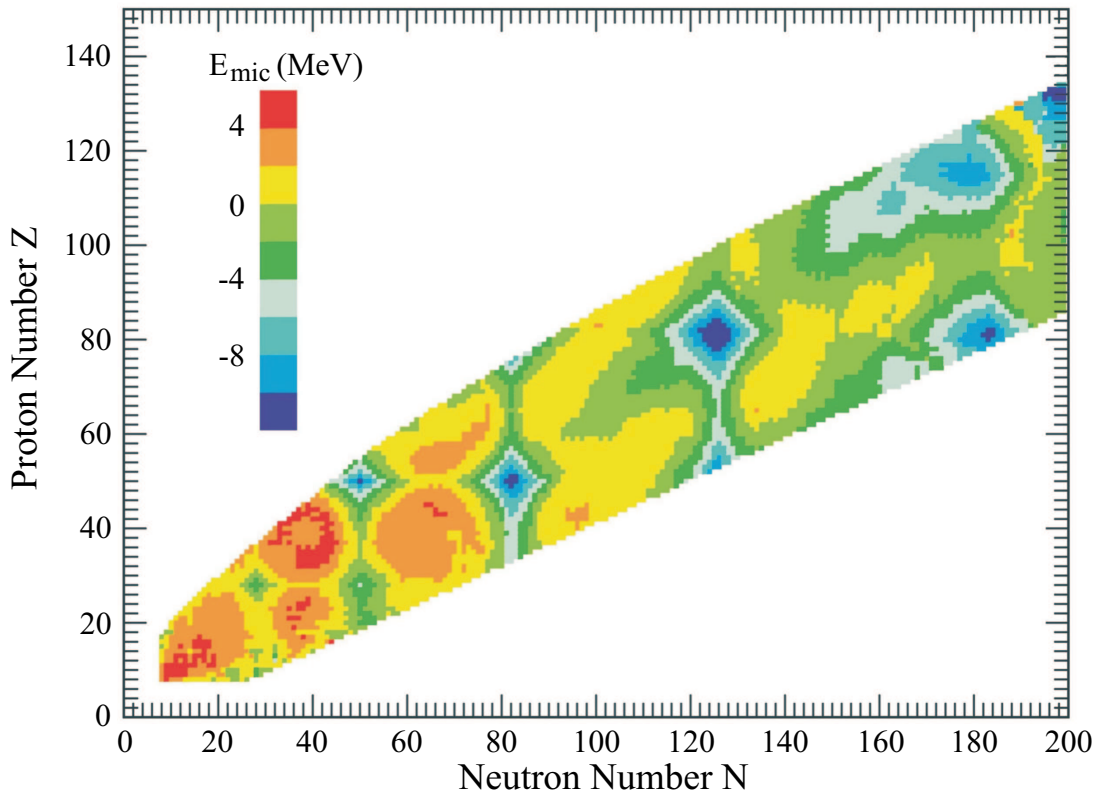

Figure 6.1: Microscopic correction to the ground state energy in terms of N and Z. The larger the absolute magnitude of the correction, the larger the shell effects. This plot is adapted from Ref. [56].

the shape fluctuations should be determined by the properties of a rotating liquid drop. The data and predictions for Cu are shown in Fig. 6.2c. The behavior of the Cu data is similar to that of Sn. The experimental width is nearly constant up to temperatures of $\sim$1 MeV. Then the width begins to increase. As in the case of Sn, the liquid drop predictions fail to describe the data, especially at low temperatures.

A measurement of the GDR width in ^{179}Au has also been performed [57]. The extracted width was found to be 5 MeV, and is shown in Fig. 6.2d. The solid curve in this figure is a calculation of the width as determined from Ref. [35] with an angular momentum of 17.5$\hbar$. Shell effects are weak in ^{179}Au, and just as in Cu and Sn, the predictions significantly overestimate the width at low temperatures.

The behavior of the experimental data for nuclei where shell effects are small

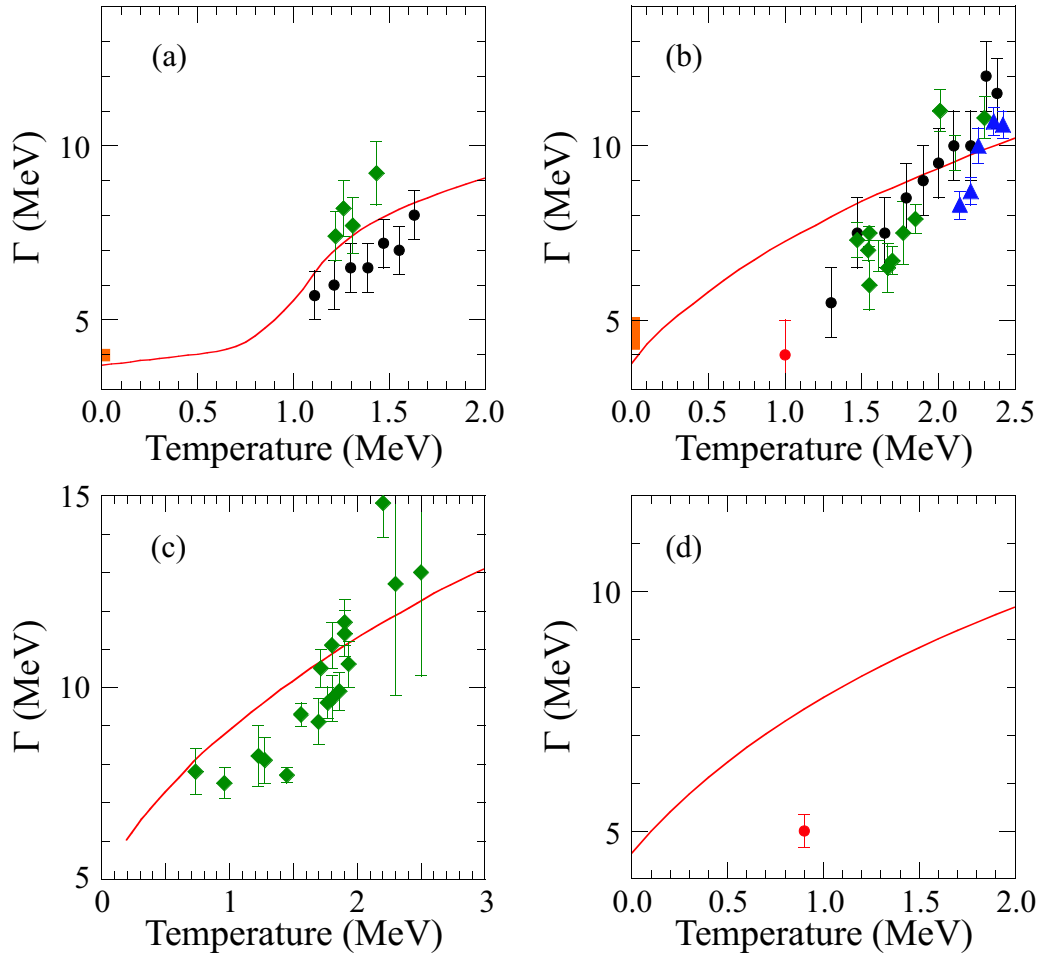

Figure 6.2: Theoretical predictions and data for Pb, Sn, Cu, and Au. Panel (a) – Pb. Panel (b) – Sn. Panel (c) – Cu. Panel (d) – Au. The solid curve in panels (a), (b), and (c) is an adiabatic thermal shape fluctuation calculation. In panels (a), (b), and (c) the black circles and green diamonds are from Ref. [35]. The black circles are from inelastic scattering measurements, whereas the green diamonds are from fusion-evaporation measurements. The blue triangles are from Ref. [22], and the solid red circle is from this work. The orange rectangle in panels (a) and (b) is the range of widths measured for the ground state value. In panels (c) and (d) the ground-state width is given by the curve at T = 0 MeV. The solid curve in panel (d) is the calculated width from Eqn. 4.14. The data point in this panel is from Ref. [57].

(Sn, Cu, and Au) is as predicted for nuclei where shell effects are large (Pb). This is evident by examination of Fig. 6.2. In the case of Pb, the GDR width is predicted to be suppressed relative to liquid drop predictions. This suppression is attributed to shell effects. While it is clear that shell effects limit shape fluctuations at low temperatures in Pb, it is not clear that these effects are responsible for the suppression of the GDR

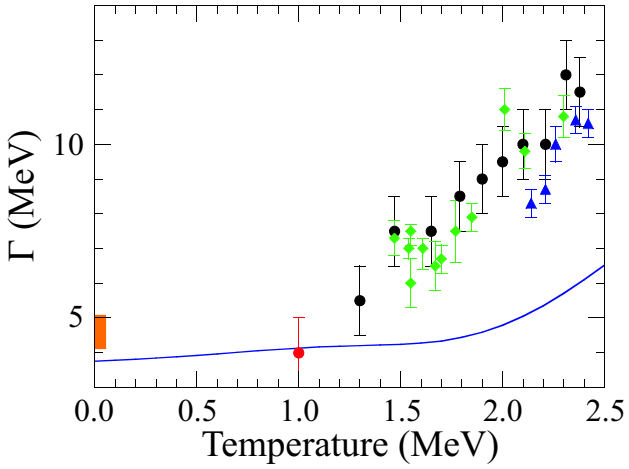

Figure 6.3: Comparison of Sn data and microscopic model predictions. The solid blue curve shows the predicted GDR width as determined from the microscopic model discussed in the text. The data is as in Fig. 6.2b.

width. In fact, the interpretation that shell effects are responsible for the suppression of the GDR width in Pb at low temperatures has to be questioned.

The suppression of the GDR width at low temperatures is evident in the experimental data for all nuclei discussed here (Sn, Cu, Au, and Pb). In the case of Sn, Cu, and Au, shell effects are weak. Despite this fact, the behavior of the GDR width is as predicted for nuclei with strong shell effects. It appears that the GDR with is suppressed at low temperatures regardless of whether shell effects are present of not.

The thermal shape fluctuation calculations neglect pairing effects. Pairing effects are predicted to be unimportant at the energies explored in this experiment. It is thought that pairing effects are only important for very low energies. Still, it would be interesting to have a calculation where pairing was included.

Another attempt to predict the GDR width is based on the interplay between one-body Landau damping and two-body collisional damping of nucleons [27, 32]. The predicted width from this theory is shown in Fig. 6.3, along with the data. The calculation was shifted such that the ground state value (T = 0 MeV) for the width was 3.8 MeV. At low temperatures (T $<$ 1 MeV), this theory describes existing data; however, the agreement at higher temperatures (T $>$ 1 MeV) is poor.

It is clear that the existing theories to describe the GDR width are not very robust. In fact, based on the lack of agreement between theory and data, it is fair to say that the evolution of the GDR width with temperature is not well understood. At this point, more theoretical work is needed. If the adiabatic thermal shape fluctuation model is to be used, the way in which the shapes are determined needs to be reconsidered. Possibly more effects could be included.

Bibliography

[1] G. F. Bertsch. Vibrations of the atomic nucleus. *Scientific American*, pages 62–73, May 1983.

[2] S. S. Dietrich and B. L. Berman. Atlas of photoneutron cross section obtained with monoenergetic photons. *At. Data and Nucl. Data Tables*, **38**:199–338, 1988.

[3] Kurt A. Snover. Giant resonances in excited nuclei. *Annu. Rev. Nucl. Part. Sci.*, **36**:545–603, 1986.

[4] E. Ramakrishnan. *Giant Dipole Resonance in Highly Excited* ^{208}*Pb Nuclei*. PhD thesis, Michigan State University, 1995.

[5] H. Steinwedel and J. H. Jensen. *Z. Naturforsch*, **52**:413, 1950.

[6] W. D. Myers, W. J. Swiatecki, T. Kodama, L. J. El-Jaick, and E. R. Hilf. Droplet model of the giant dipole resonance. *Phys. Rev. C*, **15**:2032–2043, 1977.

[7] M. Goldhaber and E. Teller. On nuclear dipole vibrations. *Phys. Rev.*, **74**:1046–1049, 1948.

[8] T. Engeland, J. Rekstad, and J. S. Vaagen. *Collective Phenomena in Atomic Nuclei*. World Scientific, 1984.

[9] B. Orlandini, V. D. Efros, and W. Leidemann. Fully microscopic calculations of giant resonances in few-body systems. *Nucl. Phys. A*, **649**:21c–24c, 1999.

[10] D. Vretenar, P. Ring, G. A. Lalazissis, and N. Paar. Relativistic mean-field description of the dynamics of giant resonances. *Nucl. Phys. A*, **649**:29c–36c, 1999.

[11] D. Drake, S. L. Whetstone, and I. Halpern. Spectra of high-energy photons emitted from the compound system ^{64}Zn in various nuclear reactions. *Phys. Lett. B*, **32**:349–350, 1970.

[12] D. Drake, S. L. Whetstone, and I. Halpern. The radiative capture of fast protons by medium-mass nuclei. *Nucl. Phys. A*, **203**:257–279, 1973.

[13] F. S. Dietrich, J. C. Browne, W. J. O'Connell, and M. J. Kay. Spectrum of γ rays in the 8- to 20-mev range from ^{252}Cf spontaneous fission. *Phys. Rev. C*, **10**:795–802, 1974.

[14] J. J. Gaardhøje, C. Ellegaard, B. Herskind, and S. G. Steadman. Nuclear shape at high spin and excitation energy. *Phys. Rev. Lett.*, **53**:148–151, 1984.

[15] J. J. Gaardhøje, C. Ellegaard, B. Herskind, R. M. Diamond, M. A. Deleplanque, G. Dines, A. O. Macchiavelli, and F. S. Stephens. Gamma decay of isovector giant resonances built on highly excited states in ^{111}Sn. *Phys. Rev. Lett.*, **56**:1783–1786, 1986.

[16] D. R. Chakrabarty, S. Sen, M. Thoennessen, N. Alamanos, P. Paul, R. Schicker, J. Stachel, and J. J. Gaardhøje. Giant resonances in excited Sn isotopes. *Phys. Rev. C*, **36**:1886–1895, 1987.

[17] A. Bracco, J. J. Gaardhøje, A. M. Bruce, J. D. Garrett, B. Herskind, M. Pignanelli, D. Barnéoud, H. Nifenecker, J. A. Pinston, C. Ristori, F. Schussler, J. Bacelar, and H. Hofmann. Saturation of the width of the giant dipole resonance at high temperature. *Phys. Rev. Lett.*, **62**:2080–2083, 1989.

[18] G. Enders, F. D. Berg, K. Hagel, W. Kühn, V. Metag, R. Novotny, M. Pfeiffer, O. Schwalb, R. J. Charity, A. Gobbi, R. Freifelder, W. Henning, K. D. Hildenbrand, R. Holzmann, R. S. Mayer, R. S. Simon, J. P. Wessels, G. Casini, A. Olmi, and A. A. Stefanini. Excitation-energy dependence of the giant dipole resonance width. *Phys. Rev. Lett.*, **69**:249–252, 1992.

[19] I. Diøszegi, D. J. Hofman, C. P. Montoya, S. Schadmand, and P. Paul. Giant dipole resonance decay from fusion-fission and quasifission of hot thorium nuclei. *Phys. Rev. C*, **46**:627–636, 1992.

[20] A. Bracco, F. Camera, M. Mattiuzzi, B. Million, M. Pignanelli, J. J. Gaardhøje, A. Maj, T. Ramsøy, T. Tveter, and Z. Źelazny. Increase in width of the giant dipole resonance in hot nuclei: Shape change or collisional damping? *Phys. Rev. Lett.*, **74**:3748–3751, 1995.

[21] M. Mattiuzzi, A. Bracco, F. Camera, W. E. Ormand, J. J. Gaardhøje, A. Maj, B. Million, M. Pignanelli, and T. Tveter. Angular momentum dependence of the gdr width in sn nuclei at fixed excitation energy. *Nucl. Phys. A*, **612**:262–278, 1997.

[22] M. P. Kelly, K. A. Snover, J. P. S. van Schagen, M. Kicińska-Habior, and Z. Trznadel. Giant dipole resonance in highly excited nuclei: Does the width saturate? *Phys. Rev. Lett.*, **82**:3404–3407, 1999.

[23] J. R. Beene, F. E. Bertrand, M. L. Halbert, R. L. Auble, D. C. Hensley, D. J. Horen, R. L. Robinson, R. O. Sayer, and T. P. Sjoreen. Heavy-ion excitation and photon decay of giant resonances in ^{208}Pb. *Phys. Rev. C*, **39**:1307–1319, 1989.

[24] M. Thoennessen, J. R. Beene, F. E. Bertrand, D. J. Horen, M. L. Halbert, D. C. Hensley, J. E. Lisantti, W. Mittig, Y. Schutz, N. Alamanos, F. Auger, J. Barrette, B. Fernandez, A. Gillibert, B. Haas, J. P. Vivien, and A. M. Nathan. High-energy

target excitations in heavy ion inelastic scattering. *Phys. Rev. C*, **43**:R12–R15, 1991.

[25] E. Ramakrishnan, T. Baumann, A. Azhari, R. A. Kryger, R. Pfaff, M. Thoennessen, S. Yokoyama, J. R. Beene, M. L. Halbert, P. E. Mueller, D. W. Stracener, R. L. Varner, R. J. Charity, J. F. Dempsey, D. G. Sarantites, and L. G. Sobotka. Giant dipole resonance built on highly excited states of ^{120}Sn nuclei populated by inelastic α scattering. *Phys. Rev. Lett.*, **76**:2025–2028, 1996.

[26] E. Ramakrishnan, A. Azhari, J. R. Beene, R. J. Charity, M. L. Halbert, P. F. Hua, R. A. Kryger, P. E. Mueller, R. Pfaff, D. G. Sarantites, L. G. Sobotka, M. Thoennessen, G. Van Buren, R. L. Varner, and S. Yokoyama. Temperature dependence of the giant dipole resonance width in ^{208}Pb. *Phys. Lett. B*, **383**:252–257, 1996.

[27] T. Baumann, E. Ramakrishnan, A. Azhari, J. R. Beene, R. J. Charity, J. F. Dempsey, M. L. Halbert, P. F. Hua, R. A. Kryger, P. E. Mueller, R. Pfaff, D. G. Sarantites, L. G. Sobotka, D. W. Stracener, M. Thoennessen, G. Van Buren, R. L. Varner, and S. Yokoyama. Evolution of the giant dipole resonance in excited ^{120}sn and ^{208}pb nuclei populated by inelastic alpha scattering. *Nucl. Phys. A*, **635**:428–445, 1998.

[28] A. Smerzi, A. Bonnsera, and M. DiToro. Damping of giant resonances in hot nuclei. *Phys. Rev. C*, **44**:1713–1716, 1991.

[29] A. L. Goodman. Statistical shape fluctuations in ^{166}Er. *Phys. Rev. C*, **37**:2162–2169, 1988.

[30] J. J. Gaardhøje. Nuclear structure at high excitation energy studied with giant resonances. *Annu. Rev. Nucl. Part. Sci.*, **42**:483–536, 1992.

[31] W. E. Ormand, P. F. Bortignon, R. A. Broglia, T. Døssing, and B. Lauritzen. Time-dependent thermal fluctuations and the giant resonance in hot, rotating nuclei. *Phys. Rev. Lett.*, **64**:2254–2257, 1990.

[32] V. Baran, M. Colonna, M. DiToro, A. Guarnera, V. N. Kondratyev, and A. Smerzi. The many facets of giant resonances at high excitation energies. *Nucl. Phys. A*, **599**:29c–48c, 1996.

[33] W. E. Ormand, P. F. Bortignon, and R. A. Broglia. Temperature dependance of the width of the giant dipole resonance in ^{120}Sn and ^{208}Pb. *Phys. Rev. Lett.*, **77**:607–610, 1996.

[34] W. E. Ormand, P. F. Bortignon, R. A. Broglia, and A. Bracco. Behavior of the giant-dipole resonance in ^{120}Sn and ^{208}Pb at high excitation energy. *Nucl. Phys. A*, **614**:217–237, 1997.

[35] D. Kusnezov, Y. Alhassid, and K. A. Snover. Scaling properties of the giant dipole resonance width in hot rotating nuclei. *Phys. Rev. Lett.*, **81**:542–545, 1998.

[36] G. Viesti, M. Lunardon, D. Fabris, G. Nebbia, M. Cinausero, E. Fioretto, D. R. Napoli, G. Prete, K. Hagel, J. B. Natowitz, R. Wada, P. Gonthier, Z. Majka, R. Alfarro, Y. Zhao, N. Mdeiwayeh, and T. Ho. Energy deposition and GDR emission in the reaction ^{209}Bi(α,α') at 240 MeV. *Nucl. Phys. A*, **652**:17–33, 1999.

[37] D. Fabris, G. Nebbia, G. Viesti, M. Lunardon, M. Cinausero, E. Fioretto, D. R. Napoli, G. Prete, K. Hagel, J. B. Natowitz, R. Wada, P. Gonthier, Z. Majka, R. Alfarro, Y. Zhao, N. Mdeiwayeh, and T. Ho. Energy deposition in (α,α') reactions at 60 Mev u^{-1}. *J. Phys. G*, **23**:1377–1382, 1997.

[38] M. Laval, M. Moszyński, R. Allemand, E. Cormoreche, P. Guinet, R. Odru, and J. Vacher. Barium fluoride – inorganic scintillator for subnanosecond timing. *Nucl. Instr. and Meth.*, **206**:169–176, 1983.

[39] Glenn F. Knoll. *Radiation Detection and Measurement.* John Wiley & Sons, Inc., 3rd edition, 2000.

[40] E. J. Tryggestad. *Low-Lying Dipole Strength in ^{20}O.* PhD thesis, Michigan State University, 2001.

[41] J. Yurkon, D. Bazin, W. Benenson, D. J. Morrissey, B. M. Sherrill, D. Swan, and R. Swanson. Focal plane detector for the s800 high-resolution spectrometer. *Nucl. Instr. and Meth. A*, **422**:291–295, 1999.

[42] J. A. Caggiano. *Spectroscopy of exotic nuclei with the S800 spectrograph.* PhD thesis, Michigan State University, 1999.

[43] M. Berz, K. Joh, J. A. Nolen, B. M. Sherrill, and A. F. Zeller. Reconstructive correction of aberrations in nuclear particle spectrographs. *Phys. Rev. C*, **47**:537–544, 1993.

[44] F. Pühlhofer. On the interpretation of evaporation residue mass distributions in heavy-ion induced fusion reactions. *Nucl. Phys. A*, **280**:267–284, 1977.

[45] R. Butsch, M. Thoennessen, D. R. Chakrabarty, M. G. Herman, and P. Paul. Nuclear deformation in excited pb isotopes from giant dipole γ-ray–fission angular correlations. *Phys. Rev. C*, **41**:1530–1544, 1990.

[46] J. M. Blatt and V. F. Weisskopf. *Theoretical Nuclear Physics.* Wiley, 1952.

[47] W. Reisdorf. Analysis of fissionability data at high excitation energies. *Z. Phys. A*, **300**:227–238, 1981.

[48] H. Nifenecker and J. A. Pinston. High energy photon production in nuclear reactions. *Annu. Rev. Nucl. Part. Sci.*, **40**:113–143, 1990.

[49] G. Martínez, F. M. Marqués, Y. Schutz, Gy. Wolf, J. Díaz, M. Franke, S. Hlaváč, R. Holzmann, P. Lautridou, F. Lefèvre, H. Löhner, A. Marín, T. Matulewicz, W. Mittig, R. W. Ostendorf, J. H. G. van Pol, J. Québert, P. Roussel-Chomaz, A. Schubert, R. H. Siemssen, R. S. Simon, Z. Sujkowski, V. Wagner, and H. W. Wilschut. Bremsstrahlung photons as a probe of hot nuclei. *Phys. Lett. B*, **349**:23, 1995.

[50] Detector description and simulation tool geant, version 3.21, cern program library, geneva.

[51] N. P. Shaw. *High Energy γ-rays from Highly Excited Thorium, Californium, and Meitnerium.* PhD thesis, State Univeristy of New York at Stony Brook, 1999.

[52] A. Gilbert and A. G. W. Cameron. A composite nuclear-level density formula with shell corrections. *Canadian Journal of Physics*, **43**:1446–1496, 1965.

[53] H. A. Bethe. *Rev. Mod. Phys.*, **9**:69, 1937.

[54] B. L. Berman. Atlas of photoneutron cross sections obtained with monoenergetic photons. *At. Data and Nucl. Data Tables*, **15**:319–390, 1975.

[55] Y. Alhassid and B. Bush. Effects of thermal fluctuations on giant dipole resonances in hot rotating nuclei. *Nucl. Phys. A*, **509**:461–498, 1990.

[56] P. Moller, J. R. Nix, W. D. Myers, and W. J. Swiatecki. website: http://t2.lanl.gov/publications/masses/normal.html.

[57] F. Camera, A. Bracco, V. Nanal, M. P. Carpenter, F.della Vedova, S. Leoni, B. Million, S. Mantovanil, M. Pignanelli, O. Wieland, B. B. Back, A. M. Heinz, R. V. F. Janssens, D. Jenkins, T. L. Khoo, F. G. Kondev, T. Lauritsen, C. J. Lister, B. Mcclintock, S. Mcclintock, S. Mitsuoka, E. F. Moore, D. Seweryniak, R. J. Van Swol, D. Hofman, M. Thoennessen, K. Eisenman, P. Heckman, J. Seitz, R. L. Varner, M. L. Halbert, I. Dioszegi, and A. Lopez-Martens. Radiative fusion from very symmetric reactions: The giant dipole resonance in the ^{179}Au nucleus. to be published.